

**THE THERMAL AND METAMORPHIC EVOLUTION OF MOUNTAIN BELTS AS
A RESPONSE TO EROSION, ACCRETION, AND RADIOGENIC HEATING**

by

AUDREY DEAN HUERTA

M.S. Idaho State University (1992)

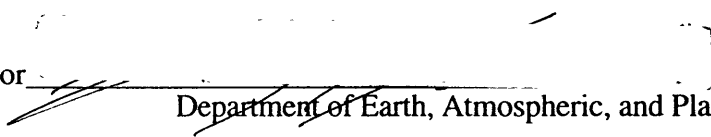
B.S. University of Utah (1984)

Submitted to the
Department of Earth, Atmospheric, and Planetary Sciences
in Partial Fulfillment of the Requirements for the Degree of

DOCTOR OF PHILOSOPHY
at the
MASSACHUSETTS INSTITUTE OF TECHNOLOGY
February, 1999

© Massachusetts Institute of Technology, 1999. All rights reserved.

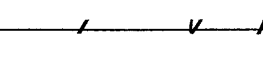
Signature of Author


Department of Earth, Atmospheric, and Planetary Sciences

Certified by

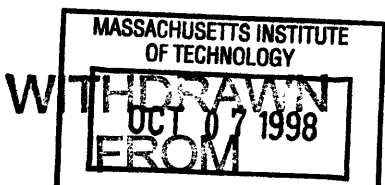

Kip V. Hodges
Thesis Supervisor
September 21, 1998

Certified by


Leigh H. Royden
Thesis Co-Supervisor

Accepted by

Ronald Prinn
Department Head





THE THERMAL AND METAMORPHIC EVOLUTION OF MOUNTAIN BELTS AS A RESPONSE TO EROSION, ACCRETION, AND RADIOGENIC HEATING

AUDREY DEAN HUERTA

Submitted to the Department of Earth, Atmospheric and Planetary Sciences
on September 23, 1998 in Partial Fulfillment of the Requirements for the Degree of
Doctor of Philosophy in Geology

ABSTRACT

Simple thermal models of collisional orogenesis generally predict metamorphic temperatures that are much cooler than those revealed by thermobarometric studies of real metamorphic terrains. This thesis focuses on a more realistic model that accounts for the redistribution of crust enriched in heat-producing elements by accretion and erosion. In collisional settings, these processes lead to the development and growth of a wedge of heat-producing crust within the overriding plate. Maximum temperatures in an orogenic setting occur within this wedge, and inverted thermal gradients occur beneath the zone of maximum temperatures, a characteristic not displayed by simple models that ignore the combined effects of accretion and erosion.

Synthetic metamorphic field gradients generated by tracking the pressure-temperature history of rocks advected through a model orogen are generally similar to those observed in the field. Specific aspects of these metamorphic patterns can be related to the relative rates of accretion, erosion, and plate convergence. In particular, peak metamorphic temperatures within the core of an orogen are related to ratios of accretion rate to convergence velocity; and the distance from the toe of an orogen to the metamorphic core is controlled by the ratio of erosion rate to accretion rate. In addition, results of this model challenge two prevailing paradigms in metamorphic petrology: 1) that the metamorphic record does not closely reflect the geothermal gradients within an orogen; and 2) that metamorphic pressure-temperature paths characterized by isothermal decompression require rapid unroofing. Under special (but nonetheless realistic) conditions, metamorphic field gradients closely mimic actual geotherms. The model predicts that pressure-temperature paths for rocks from the metamorphic cores of mountain ranges will display a component of isothermal decompression, even at low exhumation rates.

The sensitivity of the metamorphic history of a synthetic collisional orogen to the rate and geometry of accretionary and erosional processes implies that it should be possible to use the metamorphic record of a real orogen to extract information about rates of deformation and denudation. Tests of this hypothesis with data from the Himalayan orogen confirm that most critical parameters can be constrained to within about 30%.

Thesis advisor: Kip V. Hodges
Title: Professor of Geology

TABLE OF CONTENTS

<i>Title Page</i>	1
<i>Abstract</i>	3
<i>Table of Contents</i>	5
<i>Introduction</i>	7
<i>Chapter 1:</i>	13
<i>The interdependence of deformational and thermal processes in mountain belts</i>	
<i>Chapter 2:</i>	17
<i>The thermal structure of collisional orogens as a response to accretion, erosion, and radiogenic heating</i>	
<i>Chapter 3:</i>	53
<i>The effects of accretion, erosion, and radiogenic heat on the metamorphic evolution of collisional orogens</i>	
<i>Chapter 4:</i>	103
<i>Constraining the rates of orogenic processes from petrologic data.</i>	

INTRODUCTION

During the past quarter-century, advances in the fields of structural geology, petrology, and geochronology in the context of plate tectonics have revolutionized our understanding of the thermal and structural development of continental crust. These disciplines reveal that the evolution of mountain ranges is governed by the interplay of metamorphism, deformation, and exhumation, but the exact nature of the relationships between these processes has remained elusive.

Part of the problem has been that thermal models of collisional orogenesis have a difficult time reproducing some aspects of the metamorphic records preserved in mountain ranges. In particular, modeled temperatures are typically cooler than those in real orogens. In addition, inverted metamorphic gradients, which are found in a variety of natural examples (e.g., the Himalaya - Le Fort, 1975), are difficult to produce and even harder to preserve in simple models. The response of the modeling community to such problems has been to invoke special processes – such as extreme frictional heating within fault zones (Bird et al., 1975; England et al., 1992; Molnar & England, 1990) or unusually high rates of heat transfer from the asthenosphere (Bird, 1978; De Yoreo et al., 1991; Oxburgh & Turcotte, 1975) – to artificially boost the thermal budget. In this thesis, I approach the problem somewhat differently: using only simple, intrinsic processes of orogenesis and the known properties of materials in orogenic systems, is it possible to produce a viable model that reproduces common metamorphic observations? Building on previous studies (particularly that of Royden, 1993), I have shown that the accretion of material enriched in radioactive heat-producing elements and the eventual removal of this material from the orogenic system through erosion can reproduce the metamorphic patterns found in mountain ranges with remarkable fidelity.

The first chapter of this thesis is published in *Science* under the authorship of Huerta, Royden and Hodges (Huerta et al., 1996). Here we present the results of a two-

dimensional numerical model addressing the time-dependent effects of accretion and erosion on the thermal structure of orogenic systems in which an upper layer of crust is enriched in heat producing elements. Results indicate that the processes of accretion and erosion can result in high temperatures at mid-crustal levels at time scales consistent with observed metamorphism. In addition, inverted geotherms, similar to those observed in settings like the Himalaya, developed within the upper plate.

The second chapter is presented in the *Journal of Geophysical Research* under the authorship of Huerta, Royden and Hodges (Huerta et al., 1998). This chapter further investigates how the processes of accretion and erosion control the thermal evolution of collisional orogens using the model described in the previous chapter. Two processes – the accretion of crust enriched in heat -producing elements from the down-going plate to the upper plate, and the subsequent erosion of the surface of the upper plate – result in the formation of a wedge of heat-producing crust within the upper plate. This wedge exerts first-order control on the thermal structure of the orogen. Thick wedges and high heat-production rates lead to high upper-plate temperatures, while wide wedges result in broad high-temperature regions within the upper plate.

The third chapter has been submitted to *Journal of Metamorphic Geology* under the authorship of Huerta, Royden and Hodges (Huerta et al., submitted). In this chapter, our model is used to track the pressure-temperature history of rocks moved through an orogen by the processes of subduction, accretion and erosion. These histories are used to construct regional metamorphic patterns reflecting maximum temperatures (T_{max}), pressures at the time of T_{max} , and age at T_{max} . The predicted metamorphic field gradients are similar to observed metamorphic patterns in that metamorphic temperatures increase with distance from the toe of the orogen to a maximum at the “metamorphic core” of the orogen. While previous chapters only addressed orogens in which accretion acted continuously, in this chapter episodic accretion is also considered. In all cases, two key facets of the metamorphic record – the maximum temperatures within the metamorphic core and the

distance from the toe of the orogen to the metamorphic core – can be related to relative rates of accretion, erosion, and convergence velocity. Maximum temperatures within the metamorphic core are determined by the depth of the heat-producing wedge and the heat-production rate of crust within the wedge, while the distance from the toe of the orogen to the metamorphic core is related to the width of the heat-producing wedge. Since the both the thermal structure of the orogen (as controlled by the geometry of the heat-producing wedge) and the particle paths of rocks advected through the orogen are determined by the advective rates, the metamorphic record of an orogen can be related to the rates of accretion, erosion, and plate convergence. High metamorphic temperatures in the core result from low ratios of accretion rate to convergence velocity (deep wedges), while cores located far from the toe of the orogen result from low ratios of erosion rate to accretion rate (wide wedges)

The final chapter will be submitted to *Tectonics* in 1998 under the authorship of Huerta, Hodges and Royden. This chapter addresses the applicability of our model by comparing synthetic metamorphic patterns to observed metamorphism within the Himalaya. Model results indicate that only a few input parameters control the metamorphic history of an orogen. Geological and geophysical data from the Himalaya constrain these parameters to some extent, however the uncertainties are sufficiently large that model results based on these parameters cover a broad spectrum of metamorphic patterns. While some of these synthetic metamorphic patterns are consistent with the observed metamorphism, some are not only inconsistent, but are also physically impossible. However, by requiring the model to be consistent with the observed metamorphic record, we can substantially limit the acceptable range of values for the key input parameters. This observation indicates that the record of ancient orogens can be used to successfully constrain the rates of important orogenic processes.

This thesis has analyzed the thermal evolution of collisional orogens as a response to the redistribution of crust enriched in heat producing elements due to *assigned*

deformational and erosional processes. However, the kinematic model used here can not address the impact of the thermal structure on the deformational and erosional histories of an orogen. Since the strength of the crust is strongly influenced by temperature, the mechanical response of the crust during collision should evolve as temperatures increase. Thus, the next step in understanding mountain belts is to develop dynamic models that can address the interdependence of the thermal and mechanical evolutions of orogens.

References

- Bird, P., 1978. Initiation of intracontinental subduction in the Himalaya, *Journal of Geophysical Research-B.*, **83**, 4975-4987.
- Bird, P., M.N. Toksoz, and N.H. Sleep, 1975. Thermal and mechanical models of continent-continent convergence zones, *Journal of Geophysical Research-B.*, **80**, 4405-4416.
- De Yoreo, J.J., D.R. Lux, and C.V. Guidotti, 1991. Thermal modeling in low-pressure/high-temperature metamorphic belts, *Tectonophysics*, **188**, 209-238.
- England, P.C., and A. Thompson, 1986. Some thermal and tectonic models for crustal melting in continental collision zones, in *Collision Tectonics*, edited by M.P. Coward and A.C. Ries, *Geological Society Special Publication*, **19**, 83-94.
- England, P., P. Le Fort, P. Molnar, and A Pecher, 1992. Heat Sources for Tertiary Metamorphism and Anatexis in the Annapurna-Manaslu Region Central Nepal, *Journal of Geophysical Research-B*, **97**, 2107-2128.
- Huerta, A.D., L. Royden and K. Hodges, 1996. The Interdependence of Deformational and Thermal Processes in Mountain Belts, *Science*, **273**, 637-639.
- Huerta, A.D., L. Royden and K. Hodges, 1998. The thermal structure of collisional orogens as a response to accretion, erosion, and radiogenic heating. *Journal of Geophysical Research-B*, **103**, 15287-15302.
- Huerta, A.D., L. Royden and K. Hodges, submitted. The effects of accretion, erosion, and radiogenic heat on the metamorphic evolution of collisional orogens. *Journal of Metamorphic Geology*.
- Le Fort, P., 1975. Himalayas: the collided range. Present knowledge of the continental arc. *American Journal of Science*, **275-A**, 1-44.
- Molnar, P. and P. England, 1990. Temperatures, heat flux, and frictional stress near major thrust faults, *Journal of Geophysical Research-B*, **95**, 4833-4856.
- Oxburgh, E.R., and D.L. Turcotte, 1974. Thermal gradients and regional metamorphism in overthrust terrains with special reference to the eastern Alps, *Schweiz. Mineral. Petrogr. Mitt.*, **54**, 641-662.

The Interdependence of Deformational and Thermal Processes in Mountain Belts

Audrey D. Huerta,* Leigh H. Royden, and Kip V. Hodges

The Interdependence of Deformational and Thermal Processes in Mountain Belts

Audrey D. Huerta,* Leigh H. Royden, Kip V. Hodges

Crustal temperatures within collisional orogens are anomalously high compared with temperatures at comparable depths in stable continents, which is evidence of thermal processes that are fundamental to orogenesis. These temperatures can be explained by the redistribution of crust enriched in heat-producing elements through the accretion of crust from the down-going plate to the upper plate and surface erosion. With the use of geologically reasonable rates, the model results predict high temperatures (over 600°C) and inverted upper-plate geotherms (about 100°C over 20 kilometers) at shallow depths (20 to 40 kilometers) by 25 to 35 million years after collision. This study emphasizes the interdependence of deformational, surficial, and thermal processes.

Rocks present at the surface in many collisional orogens contain metamorphic mineral assemblages indicating high temperatures (~600° to 700°C) at midcrustal depths (20 to 30 km) (1). In some orogens this high-temperature metamorphism is associated with in situ partial melts (2), whereas less commonly, inverted metamorphic field gradients may develop within the upper plate (3, 4). Despite early suggestions that these phenomena could be explained by thrusting of hot rocks over cold rocks and by thickening of an upper crustal layer enriched in heat-producing elements (HPEs) during shortening (3, 5, 6), subsequent models that quantify the advection and conduction of heat during noninstantaneous thrusting have not reproduced observed thermal structures very well and are unable to explain steep-to-inverted metamorphic field gradients within the upper plate (7). Such shortcomings suggest that previous studies have neglected one or several processes that are responsible for the first-order thermal structure of collisional orogens.

Although previous studies have recognized the potential impact of HPE-enriched material within collisional belts (6, 8) and the importance of rapid surface denudation and accretion of material from the lower plate to the upper plate (9), our understanding of the thermal consequences of accretion and erosion on HPE-enriched crust has been limited to steady-state results (10). And although these results suggest that erosion and accretion can exert dramatic controls on the temperature structure, they are based on an idealized orogenic system in which the upper plate is HPE-enriched everywhere

Here we present the results of a numer-

ical study addressing the time-dependent effects of erosion and accretion on the thermal structure of orogenic systems, using a more realistic distribution of HPE-enriched crust based on a simplified subduction zone geometry (Fig. 1). The contact between the upper and lower plates was assumed to have a uniform dip, at angle θ . Convergence between upper and lower plates occurred at a constant rate v_c . Material was accreted from the lower to the upper plate at rate a , and material was removed from the surface of the upper plate at rate e (both measured in the vertical direction). The frame of reference was held fixed with respect to the toe of the upper-plate wedge, and material within the upper and lower plates moved with respect to the frame of reference. Standard finite difference techniques for calculation of conduction and advection of heat were used to compute the thermal evolution of the system. Initial thermal conditions were calculated as the steady-state conditions for subduction of a nonradioactive oceanic lithosphere at a convergence rate v_c , with no accretion across the subduction boundary or erosion at the surface. The upper plate initially contained an upper layer of HPE-enriched crust with heat production rate A and thickness d_r . Computation began at the time of collision ($t = 0$), as simulated by the introduction of lower plate continental crust with an HPE-enriched upper layer having heat production rate A and thickness d_r , and by the concomitant initiation of erosion and accretion. This was a highly idealized model of collision, inasmuch as it is not necessarily true that all three processes would begin simultaneously. We also ignored internal deformation within the upper and lower plates.

Accretion of HPE-enriched material from the lower plate to the upper plate resulted in the development of an HPE-enriched wedge (Fig. 2). The size and shape of this wedge were critical to the thermal evolution of the orogen. This triangular

wedge reached a maximum steady-state depth of

$$d_w = d_r \left(1 - \frac{e}{a} + \frac{v_c}{a} \sin \theta \right) \quad (1)$$

and a steady-state surface width of

$$s_w = \frac{d_w}{e/a \tan \theta} \quad (2)$$

at time

$$t_w = \left(\frac{d_r}{e} \right) \left(1 + \frac{v_c}{a} \sin \theta \right) \quad (3)$$

Initially, the upper plate was cold, with temperatures less than 300°C to depths in excess of 60 km. By $t = 8$ million years (My), temperatures within the toe of the upper plate had increased as HPE-enriched material was accreted to the upper plate and the HPE-enriched wedge began to form. By $t = 16$ My, temperatures within the upper plate increased to >400°C at a depth of 25 km. By $t = 24$ My, the thermal gradient had inverted, and a local temperature maximum in excess of 500°C had developed near the base of the HPE-enriched wedge in the upper plate at depths of 20 to 40 km. By $t = 32$ My, maximum temperatures within the upper plate were in excess of 600°C at depths of ~30 km, and maximum surface heat flow was on the order of 125 $\mu\text{W}/\text{m}^2$. From 32 My onward, temperatures changed relatively slowly within the evolving orogen and reached thermal steady state by about $t = 120$ My, at which

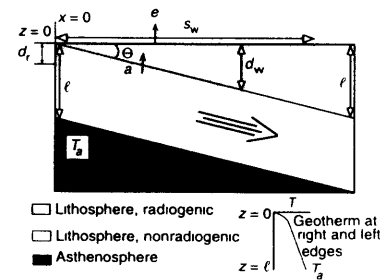


Fig. 1. Simplified subduction zone with dip θ , convergence velocity v_c , and lithospheric thickness l . Material is accreted from the lower to the upper plate at rate a (vertical component) and removed at the surface at rate e . The HPE-enriched wedge within the upper plate (light shaded area) has steady-state depth d_w and surface width s_w . Temperatures (T) are 0°C at $z = 0$ and T_a at the base of the lower plate. Dark shaded area indicates asthenosphere with $T = T_a$. Thermal boundary conditions at the right and left sides of the area modeled (at $x = 0$ and $x = l/\tan \theta$) for $z < l$ are steady-state temperatures for lithosphere with HPE-enriched crust to depth d_r , and are $d^2T/dx^2 = 0$ for $z > l$.

Department of Earth, Atmospheric, and Planetary Sciences, Massachusetts Institute of Technology, Cambridge, MA 02139, USA

*To whom correspondence should be addressed

time the temperature maximum ($>700^{\circ}\text{C}$) was located at a depth of about 30 km. The HPE-enriched wedge reached a steady-state shape by $t = 39$ My, with $d_w = 44$ km and $s_w = 225$ km.

Three parameters controlled steady-state maximum temperatures and inversion of geotherms: A , d_w , and v_c . The depth of the HPE-enriched wedge and the heat production rate had the most substantial impact on the thermal structure. Increasing either A or d_w (while all other parameters were held constant) resulted in substantially higher temperatures within the orogen and contributed to the inversion of geotherms within the upper plate; decreasing A or d_w

resulted in lower temperatures within the orogen and a lesser degree of inversion. Increasing the convergence velocity (holding all other parameters constant) resulted in slightly depressed temperatures at depths >15 km, especially near the subduction contact, and geotherms were more inverted; lower convergence velocities resulted in slightly higher temperatures and geotherms showed less inversion. Although the width of the wedge did not control the magnitude of maximum temperatures, increasing s_w (holding all other parameters constant) resulted in a broader region of elevated temperatures, with upper plate maximum temperatures located farther toward the hinter-

land. The transient thermal evolution was also primarily controlled by A , d_w , and v_c . High temperatures at shallow levels and inverted geotherms within the upper plate developed more quickly for higher values of v_c and d_w or for higher values of A , or both; high temperatures and inverted geotherms took longer to develop at lower values of v_c and d_w or lower values of A , or both.

There is a reasonably broad range of parameter values that yield inverted thermal gradients in the upper plate (for example, $A \geq 1.0$ for $d_w = 55$ km, or $A \geq 3.25$ for $d_w = 35$ km). However, in order to attain temperatures in excess of 600°C at depths as shallow as ~ 20 to 30 km as well as inverted geotherms in the upper plate, moderate values of A are required (for example, $A \geq 2.0$ for $d_w = 55$ km). In order to attain temperatures in excess of 600°C and inverted geotherms in a reasonable time span ($t < 40$ My), high values of A are required (for example, $A = 3.0$ for $d_w = 45$ km). Thus, we propose that the redistribution of HPE-enriched crust into a deep zone within the upper plate is an important factor in the thermal evolution of orogenic belts where high-temperature metamorphism, crustal melting, and geothermal inversions occur.

One of the best documented examples of high-temperature metamorphism associated with inverted metamorphic field gradients occurs in the central Himalayan orogen, where paleotemperatures increase structurally upward from a Miocene intracontinental subduction boundary (the Main Central thrust zone), reaching maximum temperatures in excess of 600°C at structural distances of 5 to 10 km above the Main Central thrust zone. Geologic data from some sectors of the orogen suggest that inverted field gradients in the Himalayas resulted from an actual inversion of the geothermal gradient (4, 11, 12); in other areas, the observed field gradients have been interpreted as the result of late- or post-metamorphic structural disruption (13). Although the structural inversion of field gradients requires no special thermal circumstances, the documentation of high-grade metamorphism and inverted geothermal gradients in the Himalayas has inspired many researchers to propose that transient heat sources such as dissipative heating, mantle delamination, or other mechanisms (14) are responsible for the observed metamorphic conditions.

Comparison of the nature and timing of Himalayan metamorphism and the results presented here suggests that the effects of accretion and erosion and the attendant redistribution of HPE-enriched crust offer an alternative explanation for the development of high temperatures and inverted

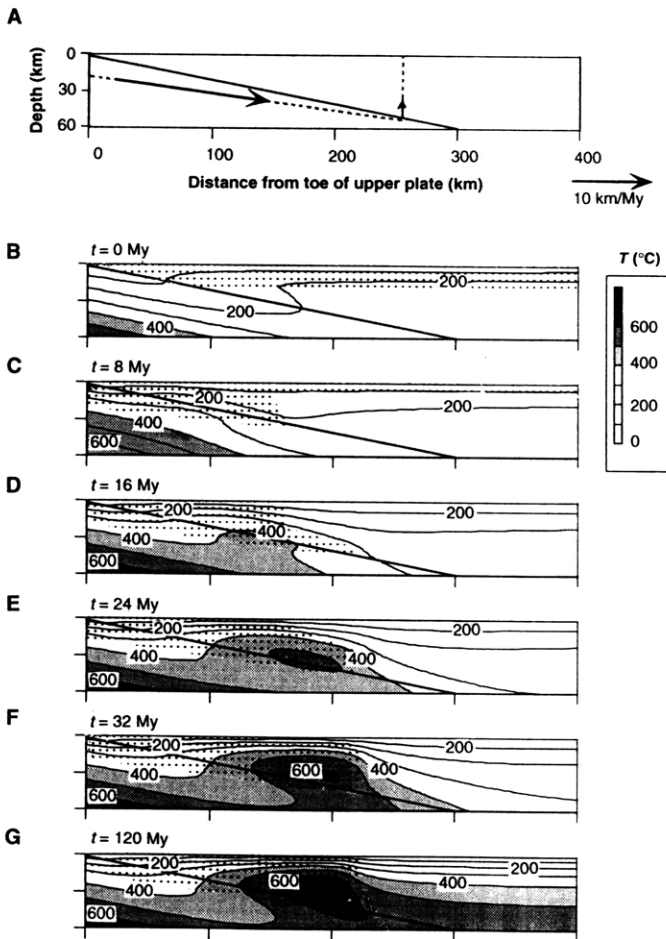


Fig. 2. Crustal cross sections for the model outlined in Fig. 1, based on $\tan \theta = 0.2$, $v_c = 20$ km/My, $a = 1.6$ km/My, $e = 1.6$ km/My, and $\ell = 126$ km. (A) Material velocity fields. (B through G) Thermal evolution and growth of HPE-enriched wedge, from $t = 0$ My (initiation of collision) to $t = 120$ My (approximately steady state). Stippled pattern indicates HPE-enriched crust with $A = 3 \mu\text{W}/\text{m}^3$. Other parameters were as follows: $d_i = 18$ km and $T_a = 1260^{\circ}\text{C}$. The width of the area modeled was 630 km, thermal conductivity was 2.5 W/mK, and thermal diffusivity was 10^{-6} m²/s. Note the inversion of geothermal gradients and a local temperature maximum in excess of 600°C at depths <30 km within the upper plate by $t = 32$ My.

geothermal gradients within collisional orogens. Within the central Himalayas, the development of inverted field gradients, accompanied by substantial crustal melting, occurred at about 20 to 25 million years ago, about 25 to 35 My after the initiation of collision between India and Eurasia (15). Rocks currently at the surface were at depths of 20 to 40 km during regional metamorphism (12, 16), yielding averaged rates of denudation of 1 to 2 km/My. Likewise, extensive tracts of lower (Indian) plate rocks with an exposed surface width greater than 300 km have been accreted episodically onto the upper (Eurasian) plate since the time of collision. Paleosubduction rates are unconstrained, but modern rates of convergence across the Himalayas are about 10 to 25 km/My (17). Radioactive heat production rates for metamorphic and igneous rocks of the Himalayas range from ~ 1.5 to $>6 \mu\text{W}/\text{m}^3$, with a significant proportion ($>25\%$) of reported values in excess of $4 \mu\text{W}/\text{m}^3$ (18). Thus, parameter values (especially $A = 3 \mu\text{W}/\text{m}^3$) used to construct Fig. 2 are consistent with observations from the Himalayas. The agreement between timing, paleotemperatures and depths recorded in the central Himalayas, and the modeled thermal structure 32 My after collision (Fig. 2) suggests that redistribution of material with a high rate of heat production within the Himalayan orogen may have been an important factor in its thermal evolution.

Our model suggests that accretion and erosion and the attendant redistribution of HPE-enriched material exert first-order control on the thermal and metamorphic evolution of collisional orogens. Accretion leads to the development and maintenance of a wedge of HPE-enriched material within the upper plate of intracontinental subduction zones. Surface erosion also controls the geometry of this wedge and enhances heating within the upper plate by advecting material from deeper to shallower crustal levels.

REFERENCES AND NOTES

- 1 R D Hatcher Jr *et al.*, in *The Appalachian-Ouachita Orogen in the United States*, R D Hatcher Jr, W A Thomas, G W Viele, Eds (Geological Society of America, Boulder, CO, 1989), pp 233-318, A Gansser, *Geology of the Himalayas* (Wiley Interscience, London, 1964)
- 2 W S Pitcher, *Geol Rundsch* **76**, 51 (1987)
- 3 P Le Fort, *Am J Sci* **275A**, 1 (1975)
- 4 M S Hubbard, *J Metamorph Geol* **7**, 19 (1989)
- 5 E R Oxburgh and D L Turcotte, *Schweiz Mineral Petrogr Mitt* **54**, 641 (1974)
- 6 P C England and A Thompson, in *Collision Tectonics*, M P Coward and A C Ries, Eds. (Special Publication 19, Geological Society of America, Boulder, CO, 1986), pp 83-94
- 7 P Bird, M N Toksoz, N H Sleep, *J Geophys. Res* **80**, 4405 (1975), Y Shi and C Y Wang, *Geology* **15**, 1048 (1987), P Karabinos and R Ketchum, *J Metamorph Geol* **6**, 559 (1988), C Ruppel and K V Hodges, *Tectonics* **13**, 17 (1994)
- 8 C Pinet and C Jaupart, *Earth Planet Sci Lett* **84**, 87 (1987)
- 9 F A Dahlen and T D Barr, *J Geophys Res* **94**, 3906 (1989), T D Barr and F. A. Dahlen, *ibid.*, p 3923, S. M. Peacock, in *Metamorphism and Crustal Evolution, Western Conterminous United States*, W G Ernst, Ed (Prentice-Hall, Englewood Cliffs, NJ, 1987), pp 953-975
- 10 L H Royden, *J. Geophys. Res.* **98**, 4487 (1993)
- 11 K V Hodges, P Le Fort, A Pêcher, *Geology* **16**, 707 (1988)
- 12 A Pêcher, *J Metamorph Geol* **7**, 31 (1989)
- 13 M Brunel and J R Kienast, *Can J Earth Sci* **23**, 1117 (1986), M P Searle and A J Rex, *J Metamorph Geol* **7**, 127 (1989)
- 14 P Molnar and P England, *J Geophys Res* **95**, 4833 (1990), G A Houseman, D P McKenzie, P Molnar, *ibid* **86**, 6115 (1981)
- 15 M S Hubbard and T M Hamson, *Tectonics* **8**, 665 (1989), K V Hodges *et al.*, *Contrib Mineral Petrol* **117**, 151 (1994), M P Searle, D J W Cooper, A J Rex, in *Tectonic Evolution of the Himalayas and Tibet*, R M Shackleton, J F Dewey, B F Windley, Eds (The Royal Society, London, 1988), pp 117-150
- 16 K V Hodges, M S Hubbard, D S Silverberg, *Philos Trans R Soc London Ser. A* **326**, 257 (1988)
- 17 H Lyon-Caen and P. Molnar, *Tectonics* **4**, 513 (1985)
- 18 B C Scaillet, C France-Lanord, P Le Fort, *J Volcanol Geotherm Res* **44**, 163 (1990), P Vidal, A Cochene, P Le Fort, *Geochim Cosmochim Acta*, **46**, 2279 (1982), A M Macfarlane, thesis, Massachusetts Institute of Technology (1992)
- 19 We thank two anonymous reviewers for helpful comments. Support was provided by NSF grant EAR 9418062 to K V H

1 April 1996, accepted 12 June 1996

CHAPTER 2:

THE THERMAL STRUCTURE OF COLLISIONAL OROGENS AS A RESPONSE TO ACCRETION, EROSION, AND RADIOGENIC HEATING

Audrey D. Huerta, Leigh H. Royden & Kip V. Hodges

Journal of Geophysical Research, 1998

Abstract.

Thermal models of collisional orogens generally predict temperature structures that are much cooler than those recovered by thermobarometric studies. Here we demonstrate that high-temperature, low-pressure metamorphism and the development of inverted geotherms within collisional belts may be the result of accretion and erosion acting on crust enriched with heat-producing elements. A new two-dimensional finite difference model, described here, incorporates the subduction of lithosphere with heat-producing material in the upper crust, accretion of crustal material from the subducting plate to the upper plate, and surface erosion of the upper plate. These processes result in the development of a wedge of heat-producing material within the upper plate. The rate of heat production within the wedge and maximum depth of the wedge are the most important parameters controlling the magnitude of upper plate temperatures. Our model yields inverted upper plate geotherms when heat production rates exceed $0.75 \mu\text{W}/\text{m}^3$ and the heat-producing wedge extends to a depth greater than 35 km. Temperatures in excess of 500°C at depths of 20-30 km are computed when heat production rates are greater than $\sim 1.75 \mu\text{W}/\text{m}^3$ and the wedge extends to a depth >50 km. Other processes, such as shear heating, fluid flow, or mantle delamination, need not be invoked to explain geologic evidence of high temperatures or inverted thermal gradients in collisional systems.

1. Introduction

Quantitative thermobarometry and geochronology have improved our ability to place constraints on the deformational and thermal evolution of collisional orogens, yet many questions remain largely unanswered. For example, collisional orogens commonly contain rocks with high-temperature metamorphic assemblages ($>500^{\circ}\text{C}$), recording conditions several hundred degrees hotter than expected for a “normal” stable continental geotherm. In addition, many collisional zones contain anatectic melt products that are spatially and temporally associated with peak metamorphic mineral assemblages. The sources of heat responsible for high temperatures at shallow levels remain problematic, and a variety of mechanisms have been proposed, including thickening of crust enriched in heat-producing elements [England and Thompson, 1986], shear heating within fault zones [Bird *et al.*, 1975; England *et al.*, 1992; Molnar and England, 1990], and high levels of transient heat flow from the asthenosphere [Bird, 1978a; De Yoreo *et al.*, 1991; Oxburgh and Turcotte, 1975].

Some orogenic belts retain metamorphic evidence of inverted geothermal gradients [Hubbard, 1989; Graham and Powell, 1984]. A variety of models have been developed to relate such inversions to orogenic processes, but none are consistent with basic geologic constraints in the Himalayan orogen, which displays the best documented example of inverted geothermal gradients within a collisional system. For example, Jamieson *et al.* [1996] have shown that inverted metamorphic gradients can be the result postmetamorphic structural restacking; however, this is not consistent with the lack of field evidence of significant postmetamorphic structures along critical transects [Hubbard, 1989; Macfarlane, 1995]. England and Molnar [1993] proposed that shear heating due to friction along the main shear boundary could heat the upper plate and cause inversion of geotherms. However, this mechanism does not yield the observed geothermal inversions at the appropriate structural position, and very high shear stresses are required (>100 MPa) to raise temperatures sufficiently. Royden [1993] suggested that erosion and accretion can play significant roles in controlling the steady state thermal regime of collisional orogens, and her model predicts upper plate geothermal inversions at high temperatures (600°C - 700°C) if surface erosion is rapid and if the upper plate is composed entirely of material significantly enriched in heat-producing elements.

Our goal is to develop a first-order understanding of the thermal evolution of orogenic belts based solely on processes which are common to all collisional orogens and which are geologically reasonable. We begin by reviewing the current state of knowledge about processes that affect the thermal structure of orogenic belts. These include heat flow from

the asthenosphere, crustal heat production, frictional heating, advection of rock by deformational and surficial processes, fluid flow, and magma migration.

2. Orogenic Processes, Observed and Postulated

The combination of radiogenic heat from continental crust and heat fluxed through the base of the lithosphere from the asthenosphere results in surface heat flow values in cratonic regions of 40-80 mW/m² [Sclater *et al.*, 1980]. Oceanic heat flow data indicate that the flux of heat at the base of the lithosphere is of the order of 30 mW/m² [Sclater *et al.*, 1980, 1981]; if asthenospheric conditions beneath continental lithosphere are similar, heat fluxed through the base of the lithosphere would account for ~75% to 40% of surface heat flow and yield a background geothermal gradient of ~10°/km. The remaining 10-50 mW/m² of surface heat flow is presumably attributable to radioactive heat production within the crust. Measured values of crustal heat production vary widely, from >10 μW/m³ for granites enriched in uranium and thorium to <0.1 μW/m³ for tholeiitic basalts, with an average value of ~1.7 μW/m³ for continental crust [Van Schmus, 1989].

While radiogenic and asthenospheric sources account for the heat within stable cratons, processes inherent to orogenesis may provide additional heat. One hypothesized process is the removal of downgoing oceanic lithosphere [Sacks and Secor, 1990; Davies and von Blanckenburg, 1995] or continental lithospheric mantle [Houseman *et al.*, 1981; Bird, 1978a] during subduction. Either would result in the placement of hot asthenospheric material at high levels within the lithosphere and thus raise temperatures within the crust. However, while geodynamic models suggest that such processes might occur, there is no direct evidence that detachment or convective removal of mantle lithosphere actually occurs in collisional orogens.

Another potential heat source associated with orogenesis is shear heating along the subduction boundary. Laboratory measurements of rock strength suggest differential stresses of the order of 100 MPa may be required to deform rocks within the upper crust [Brace and Kohlstedt, 1980; Kirby and McCormick, 1989], and shear heating due to fault movement associated with stresses of this magnitude is frequently invoked to explain anomalous metamorphism [Scholz, 1980; Molnar and England, 1990; England and Molnar, 1993]. However, there is no direct evidence that such high differential stresses occur in situ at plate boundaries. In fact, seismic radiation estimates and heat flow studies of the San Andreas fault suggest that shear stress on the fault is of the order of several tens of megapascals [Brune *et al.*, 1969; Lachenbruch and Sass, 1980; Zoback *et al.*, 1987], consistent with the low stress values predicted by mechanical models of subduction

boundaries [*Bird, 1978b; Barr and Dahlen, 1990*]. Thermal calculations indicate that fault movement at geologically reasonable rates (tens of kilometers per million years) associated with stress levels of the order of tens of megapascals would only affect temperatures at a local scale and would not significantly perturb the thermal structure of an orogen [*Scholz, 1980; Bird, 1978a*].

Regardless of how heat is introduced into the crust, the overall thermal structure of orogenic belts depends on how heat is distributed through the crust. In addition to conduction, other heat transfer mechanisms play an important role. In many regions, high-grade metamorphism has been attributed to the influx of high-temperature aqueous fluids [*Ferry, 1980; Hoisch et al., 1988*]. However, several studies suggest that hydrothermal fluid systems may not be regionally extensive and may not significantly perturb regional thermal structures [*Banks et al., 1991; Ferry, 1994; Ferry and Dipple, 1991*]. High-temperature metamorphism has also been attributed to magmatic intrusion [*Yardley et al., 1987; Barton and Hanson, 1989*], but some studies indicate that more than 33% of the crustal volume would have to be replaced by magma at 1000°C to raise temperatures from 300°C to 600°C [*De Yoreo et al., 1991*], and most collisional belts do not contain such large volumes of far-traveled magmas. The occurrence of large tracts of high-grade metamorphic rocks in orogens lacking evidence of thermal perturbation due to fluid flow or extensive magmatism indicates that such essentially convective processes may not play a fundamental role in heat transfer during collisional orogenesis.

Advection may be an important method of heat transfer. The three primary mechanisms of advection in collisional settings are subduction, erosion, and accretion. Studies of present day collisional orogens yield estimates of subduction rates up to 25 km/m.y. [*Lyon-Caen and Molnar, 1985*], and erosion rates up to >5.0 km/m.y. [*Li, 1976; Hubbard et al., 1991; Copeland and Harrison, 1990*]. Within the Himalayas, horizontal accretion rates of ~6 km/m.y. are indicated by the presence of ~300 km of lower (Indian) plate rocks that have been accreted to the Eurasian plate over the last ~50 m.y. Results of previous thermal models indicate that the processes of erosion and accretion are important advective processes within collisional orogens and can play a critical role in the thermal structure [*Barr and Dahlen, 1989; Royden, 1993; Huerta et al., 1996*].

If we disregard mechanisms that are of local importance or are mostly unconstrained, we find that the gross thermal structure of orogenic belts largely depends on the redistribution of asthenospheric and crustal (radiogenic) heat through the advective processes of subduction, accretion, and erosion. Our goals are to understand the nature of these processes in a theoretical way, and to determine if they alone can be responsible for the thermal structures observed within orogens or if other processes (such as shear heating,

mantle delamination, or fluid flow) must be involved. To this end, we have constructed a two-dimensional numerical model tracking the thermal history of collisional belts in which accretion and erosion act concurrently with subduction. This paper expands on the analytical study of Royden [1993] by applying a numerical method to the transient thermal evolution of collisional orogens, thus eliminating the need for the upper plate to have uniform radiogenic heat production throughout.

3. Model Configuration and Boundary Conditions

In this study, we simulate a collisional orogen as a slab of continental lithosphere of thickness l being subducted beneath an overriding wedge of continental lithosphere (Figure 1). The upper surface ($z=0$) is horizontal, the subduction boundary is assumed to have a uniform and constant dip (at angle Θ) from the surface to the base of the overriding lithosphere, and there is no internal deformation of upper or lower plates (see Table 1 for symbols, variables, and values used in this paper). A layer of crustal material enriched with heat-producing elements extends from the surface to a depth of d_r .

Convergence velocity (v_c) is defined as the velocity of particles in the downgoing plate with respect to particles in the upper plate, accretion rate (a) is defined as the rate at which material is transferred across the subduction contact and is measured vertically with respect to the subduction contact, and erosion rate (e) is defined as the vertical rate that material is removed from the upper surface.

We use a frame of reference fixed with respect to the toe of the upper plate. This choice of frame of reference eliminates computational complications that arise in a reference frame that is not stationary with respect to the subduction boundary. To illustrate this point, Figure 1b shows particle paths in two frames of reference, one fixed to the toe of the upper plate (Figure 1b, bottom), and a more familiar frame of reference that does not move horizontally with respect to particles in the upper plate (Figure 1b, middle). When erosion and accretion rates are zero, particle paths in the two frames of reference are identical (Figure 1b, top); particles in the upper plate are stationary, and particles in the downgoing plate move parallel to the subduction contact. However, the two frames of reference present very different views when a and e are nonzero. In the more familiar frame of reference (Figure 1b, middle), particles in the upper plate move vertically upwards at a rate e , while particles in the downgoing plate move at a velocity that is the sum of the velocity of upper plate particles plus the convergence velocity. In addition, in this frame of reference, the subduction contact moves horizontally with velocity $(a-e)/\tan\Theta$. The movement of the subduction contact makes analysis and computation complicated because the thickness of

the upper plate at any location changes with time. This complication is eliminated if we use a reference frame fixed to the toe of the upper plate. In this frame of reference (Figure 1b, bottom) the subduction boundary is stationary, the velocity of upper plate particles has a horizontal component $(a-e)/\tan\Theta$ and a vertical component $-e$, and the velocity of particles in the downgoing plate is the sum of the velocity of upper plate particles plus the convergence velocity.

With respect to this frame of reference, the horizontal (u) and vertical (w) velocities of particles within the upper and lower plates are given by

$$u_u = (a-e)/(\tan\Theta)$$

$$w_u = -e$$

$$u_l = v_c \cos\Theta + (a-e)/(\tan\Theta)$$

$$w_l = v_c \sin\Theta - e.$$

We solve the heat flow equation in two dimensions for conduction and advection by explicit finite difference techniques, for a box of dimensions $z=2*l$ by $x=l/\tan\Theta$, using vertical grid spacing $\Delta z=2$ km, horizontal grid spacing $\Delta x=\Delta z/\tan\Theta$, and time steps $\tau=0.05$ m.y. (Figure 1a). Boundary conditions are constant temperature of $T=0^\circ\text{C}$ at the surface ($x=0$), and constant temperature of $T=T_a$ at the “base” of the downgoing lithosphere ($z=(l+x*\tan\Theta)$, parallel to the subduction contact). Entering temperatures of the downgoing plate ($x=0, z<l$) are equivalent to the steady state temperatures of a lithosphere of thickness l with basal temperature of T_a and with an uppercrustal layer enriched in heat-producing elements to depth d_r . Boundary conditions on the right-hand edge for the upper plate ($z<l$) are also equivalent to the steady state temperatures of a lithosphere of thickness l with basal temperature of T_a and with an uppercrustal layer enriched in heat-producing elements to depth d_r . Right-hand boundary conditions for the downgoing plate ($z>l$) are such that horizontal thermal gradients are constant ($d^2T/dx^2=0$). (Note that the boundary conditions for the base of the lithosphere and the right-hand edge have little to no affect on the results presented in this paper because of the relative time scales of advection and convection.)

Initial (“precollision”) geotherms are taken as the steady state temperatures of a subduction regime with accretion and erosion rates set equal to zero. The upper plate is of “continental” lithosphere with a layer of heat-producing (HP) crust between $z=0$ and $z=d_r$, and the lower plate is “oceanic” lithosphere without HP crust (or $A=0$). At $t=0$ (initiation of “collision”), continental lithosphere (with a layer of HP crust between $z=0$ and $z=d_r$) in the downgoing plate enters the orogenic system at $x=0$, and accretion and erosion are initiated.

Subsequent to collision, continental lithosphere is subducted beneath the upper plate, accretion transfers material from the downgoing plate to the upper plate, and erosion removes material from the upper plate surface.

4. Redistribution of HP Crust

Of particular interest is the effect of accretion and erosion on the distribution of HP crust within the orogen. Subduction moves HP crust to depth, while accretion transfers this HP crust to the upper plate, and erosion advects the HP crust to the surface of the upper plate. These advective processes result in the development of a wedge of HP crust within the upper plate (Figure 1a). The HP wedge grows with time until a steady state geometry is attained. At this time, the surface width of the wedge is such that the amount of HP crust removed from the surface by erosion equals the amount of HP crust accreted to the upper plate. The steady state size of the wedge is a function of the initial thickness of the HP layer in the downgoing plate, convergence velocity, erosion rate, accretion rate, and subduction angle.

For cases where $e \neq 0$, the HP wedge within the upper plate reaches a steady state shape (Figure 1a) by time

$$t_w = \left\{ \frac{d_r}{e} \right\} * \left\{ 1 + \left(\frac{v_c}{a} \right) * \sin \theta \right\}, \quad (1)$$

with steady state maximum depth and surface width of

$$d_w = d_r * \left\{ 1 - \frac{e}{a} + \left(\frac{v_c}{a} \right) * \sin \theta \right\}, \quad (2)$$

$$s_w = d_w * \left\{ \frac{a}{e * \tan \theta} \right\}. \quad (3)$$

5. Modeled Transient Thermal Structures

Three examples illustrate the transient thermal effects of accretion and erosion and the attendant redistribution of HP material, as shown by the growth of the HP wedges and associated thermal evolutions (Figure 2). In the first case (Figure 2a), we used nominal values for advection and heat production rates with $v_c = 20$ km/m.y., $a = 2$ km/m.y., $e = 1$ km/m.y., and $A = 1.75 \mu\text{W/m}^3$ (Table 2). The HP wedge reaches steady state geometry by $t = 53$ km with maximum depth (d_w) of 44 km, and surface width (s_w) of 440 km. Initially ($t = 0$), subduction of cold “oceanic” lithosphere cools the upper plate and inverts geotherms near the subduction contact, with temperatures of less than 300°C to depths in excess of 50

km. From $t=0$ m.y. to $t=12$ m.y., temperatures near the subduction contact increase as HP material is subducted and accreted to the upper plate. By $t=12$ m.y., HP material has been subducted to a depth of $d_w=33$ km, and a significant amount of HP material had been accreted to the upper plate with temperatures in the region of HP crust in excess of 300°C at depths of ~ 30 km. As the wedge continues to grow laterally, temperatures within the growing wedge increase, and by $t=20$ m.y., the 400°C isotherm slightly inverts where it crosses from the lower plate into the upper plate. After $t=20$ m.y., temperatures near the foreland (from $x=0$ to $x=150$ km) change imperceptibly, while temperatures near the deepest portion of the wedge ($x=200$ km to $x=350$ km) continue to slowly rise. By $t=60$ m.y., the HP wedge is completely developed ($t_w=53$ m.y.), and maximum temperatures within the upper plate are of the order of 500°C at depths greater than 55 km. From $t=60$ m.y. to $t=100$ m.y., temperatures within the orogen do not change significantly, and by $t=100$ m.y., thermal steady state is achieved (t_s). Steady-state geotherms within the upper plate are slightly elevated (compared to typical cratonal geotherms) with temperatures of $400\text{--}500^\circ\text{C}$ at depths of 20–55 km and maximum temperatures of $\sim 500^\circ\text{C}$ at depths greater than ~ 55 km. Lateral thermal gradients are minimal throughout the upper plate, but isotherms near the subduction contact at depths greater than 30 km are steep to inverted.

As a second example, Figure 2b displays model results using lower accretion and erosion rates ($a=1.5$ km/m.y., $e=0.9$ km/m.y.), which result in a slowly developing ($t_w=72$ m.y.), moderately deep HP wedge ($d_w=54$ km). Early on (from $t=0$ to $t=30$ m.y.), the thermal evolution is similar to case A. However, by $t=40$ m.y., temperatures within the upper plate of Figure 2b are significantly higher ($T_{\text{max}}>500^\circ\text{C}$), and a broad region of the upper plate displays inverted geotherms associated with a local temperature maximum near the base of the HP wedge. By $t=80$ m.y., the HP wedge is completely developed ($t_w=72$ m.y.), a significant portion of the upper plate has achieved temperatures $>500^\circ\text{C}$, maximum upper plate temperatures are $>600^\circ\text{C}$, and the 400°C and 500°C geotherms are inverted where they cross from the upper plate into the lower plates. Steady-state temperatures (t_s , ~ 120 m.y.) within the upper plate are elevated, with temperatures in excess of 500°C at depths as shallow as $z\sim 25$ km and maximum temperatures within the upper plate of $>600^\circ\text{C}$ at $z\sim 35$ km.

As a third example, Figure 2c is based on the same advective rates and HP wedge geometry as Figure 2a, but the radiogenic heat production rate has been increased to $3.0 \mu\text{W}/\text{m}^3$. Following initiation of collision, temperatures within the orogen increase quickly, and by $t=12$ m.y., temperatures near the subduction contact at depths of ~ 25 km are greater than 400°C . By $t=30$ m.y., a broad region within the upper plate displays inverted geotherms associated with a local temperature maximum in excess of 600°C . Thermal

steady state has been reached by $t=100$ m.y., geotherms are inverted within the upper plate, and temperatures are $>600^\circ\text{C}$ across the orogen for $x>200$ km from $z\sim 20$ km to $z=60$ km.

For all three cases, the time to thermal steady state of the orogen as a whole (t_s) postdates full development of the HP wedge by tens of millions of years. In general, t_s decreases with increasing advective rates; doubling the advective rates reduced t_s by a factor of ~ 0.6 . The time to thermal steady state of a particular location is related to its distance from $x=0, y=0$; shallow areas close to the foreland reached thermal equilibrium by $t\sim 10$ m.y., whereas deep areas and toward the hinterland equilibrated by $t\sim t_s$.

6. Crustal Versus Asthenospheric Components of Heating

The processes of erosion, accretion and subduction not only advect heat, but they also serve to redistribute HP material within the crust. As shown in the examples above, the accumulation of HP material within the upper plate contributes significantly to the thermal budget, and the geometry of the HP wedge can exert primary control on the evolution of the thermal structure of the orogen. We next analyze the contributions of various parameters by examining the steady state thermal structures and the associated geometry of the HP wedge for a variety of different parameter combinations.

In order to better isolate and illustrate the thermal consequences of the distribution of HP crust, we have divided steady state thermal structures into two components: the steady state structure that arises from heat conducted and advected from the asthenosphere, and the thermal structure that develops due to the production, conduction and advection of heat from HP crust. We calculate the asthenosphere-derived (AD) component by setting $A=0$ and computing the resulting temperatures, and the HP crust-derived (HPD) component by setting $T_a=0$ and computing the resulting temperatures. The total thermal structure is obtained by summing the AD and HPD components.

The AD component of the steady state thermal structure is controlled by advective rates (v_c, a, e), and by the temperature at the base of the downgoing plate, T_a . In all cases, the AD component exhibits isotherms in the upper plate that dip shallowly toward the subduction zone and lowerplate isotherms that are subparallel to the subduction zone (Figures 3-6).

The HPD component of the steady state thermal structure is controlled by the rates of heat production and advection (A, v_c, a, e). Since temperature scales linearly with heat production rate, the following steady state analyses (based on a heat production rate of $1 \mu\text{W}/\text{m}^3$) can be scaled up or down to give results for any value of A . In all cases the HPD

component produces closed isotherms encircling a local temperature maximum within the upper plate (Figures 3-6).

Below, we investigate the control on the AD and HPD components of the thermal structure exerted by the subduction angle (Θ), HP wedge geometry (d_w and s_w), and convergence rate (v_c). Provided that d_r , α , k , and T_a are held constant, these four variables completely specify the thermal structure of the system.

6.1. Subduction Zone Dip (Θ)

Figure 3 displays the thermal structures for subduction dips varying from $\tan\Theta=0.1$ to $\tan\Theta=0.6$. Burial rate is held constant ($w_f=2.9$ km/m.y.) as are the vertical (z) components of all other parameters ($d_w=44$ km, and $w_u=-1$ km/m.y.), while horizontal components (s_w , u_l , and u_u) are scaled with $1/\tan\Theta$.

6.1.1. HPD component, (Figures 3a, 3b, 3c, and 3d, and Table 3). For $0.1 \leq \tan\Theta \leq 0.6$, varying the subduction angle has little effect on the thermal structures; thermal structures for subduction angles from $\tan\Theta=0.1$ to $\tan\Theta=0.4$ are nearly identical, with temperatures differing by less than 10% (Table 3). For $\tan\Theta=0.6$, temperatures within the upper plate are up to 15% lower than for $\tan\Theta=0.1$ and temperatures within the lower plate are up to 15% higher, reflecting the reduction of lateral temperature gradients by the increased horizontal conduction.

6.1.2. AD component (Figures 3e, 3f, 3g, and 3h, and Table 3). Temperatures do not vary significantly for $\tan\Theta \leq 0.4$. For $\tan\Theta=0.6$ temperatures increase slightly (<10%) in the upper plate, due to horizontal conduction from the right-hand boundary conditions.

6.1.3. Total thermal structures (HPD plus AD). Both the AD and HPD components of the thermal structure are fairly insensitive to changes in subduction zone dip for $\tan\Theta < 0.6$. Thus, total thermal structures are also be unchanged, while at higher subduction dips ($\tan\Theta \geq 0.6$) the increased horizontal conduction reduces lateral temperature gradients, resulting in a slightly cooler upper plate, and a warmer lower plate.

6.2. Maximum Depth of the HP Wedge (d_w)

The maximum depth of the HP wedge is primarily a function of accretion rate; lower accretion rates result in deeper wedges (equation (2)); for constant v_c , Θ , and s_w). In order to maintain constant surface width of the wedge we scale erosion rates using the relationship derived from equation (3),

$$\frac{e}{a} = \frac{d_w}{s_w * \tan\theta}.$$

6.2.1. HPD component (Figures 4a, 4b, and 4c, and Table 3). Increasing the maximum depth of the HP wedge (d_w) significantly raises upper plate maximum temperatures, increases temperatures somewhat throughout the hinterland, but has little effect on temperatures near the foreland. For example, increasing the maximum depth by ~50% raises the upper plate maximum temperature (T_{\max}) by a factor of two, but temperatures near the foreland ($x < 100$ km) are almost unchanged. In addition to controlling the magnitude of T_{\max} within the upper plate, the maximum depth of the HP wedge controls the location of T_{\max} . Deeper wedges have maximum temperatures located deeper and farther away from the toe of the upper plate.

6.2.2. AD component, (Figures 4d, 4e, and 4f, and Table 3). Temperatures are cooler throughout most of the orogen with decreasing a and e (increasing d_w). The lower values of a and e result in steeper particle trajectories in the lower plate and consequently steeper lower plate isotherms and cooler temperatures near the subduction contact (T_{60}). Accretion of this cool material to the upper plate results in lower temperatures throughout the upper plate and lower near-surface thermal gradients ($dT/dz_{z=0}$).

6.2.3. Total thermal structures (HPD plus AD). The AD and HPD components of the thermal structure respond in opposite ways to the maximum depth of the HP wedge; deeper wedges lead to higher temperatures for the HPD component, but lower temperatures for the AD component. Whether or not total temperatures (HPD plus AD) increase or decrease with deeper wedges depends directly on the level of radiogenic heat. For low levels of A ($\sim < 0.5 \mu\text{W}/\text{m}^3$), the AD component dominates, and deeper wedges are associated with lower temperatures overall. For higher heat production rates, the HPD component dominates, and temperatures within the upper plate increase with deeper wedges.

6.3. Surface Width of HP Wedge (s_w)

Holding v_c , d_w and Θ constant, the surface width of the HP wedge (s_w) is primarily a function of erosion rate as given by the expanded version of equation (3)

$$s_w = \frac{d_r}{e * \tan \theta} * (a - e + v_c * \sin \theta).$$

In order to maintain constant maximum depth of the wedge, we scale accretion rate to erosion rate using the relationship derived from equation (2):

$$a/e = \frac{v_c/e * \sin \theta - 1}{d_w/d_r - 1}.$$

6.3.1. HPD component (Figures 5a, 5b, and 5c, and Table 3). Increasing the surface width of the HP wedge (s_w) enlarges the expanse of heated lithosphere but does not significantly effect maximum temperatures. The surface width of the HP wedge controls the horizontal position of the maximum temperature; T_{\max} for narrower wedges is closer to the foreland, whereas T_{\max} for wider wedges is farther toward the hinterland. Temperatures near the foreland ($x < 100$ km) are fairly insensitive to changes in the surface width of the HP wedge.

6.3.2. AD component (Figures 5d, 5e, and 5f, and Table 3). Changes to e and a associated with increasing s_w result in lower temperatures in the hinterland ($x > 250$ km), while temperatures near the foreland are not significantly effected. The lower erosion rates associated with wider wedges advects hot material from deeper levels more slowly, resulting in lower temperatures and near-surface thermal gradients (T_{60} , and $T/dz_{z=0}$).

6.3.3. Total thermal structures (HPD plus AD). The two components of the thermal structures respond in opposite ways to variations in the surface width of the HP wedge; increasing s_w raises maximum upper plate temperatures slightly for the HPD component, while leading to cooler upper plate temperatures for the AD component. Thus, for low levels of A ($\sim < 1.0 \mu\text{W}/\text{m}^3$) the AD component dominates and wider wedges are associated with slightly cooler temperatures. For higher heat production rates, the HPD component dominates and temperatures within the upper plate increase slightly with wider wedges.

6.4. Convergence Velocity (v_c)

Varying the convergence velocity alone changes the geometry of the HP wedge (equations (2) and (3), constant Θ). Thus, in order to maintain constant d_w and s_w , erosion rate and accretion rate are scaled with v_c such that v_c/a and v_c/e are held constant.

6.4.1. HPD component: (Figures 6a, 6b, 6c, 6d, and 6e, and Table 3). Higher convergence velocities result in slightly lower temperatures throughout the orogen as both material and heat is moved through the system more rapidly. For example, comparison of Figures 6a and 6c shows that doubling v_c (along with a and e) decreases maximum temperatures by less than 20%, while temperatures near the foreland ($x < 100$ km) are not significantly affected. Upper plate maximum temperature are attained at shallower levels and farther from the toe of the upper plate for higher convergence velocities.

The relative insensitivity of the thermal structure to convergence velocity is independent of wedge geometry. Doubling v_c lowers maximum temperatures by $\sim 10\%$ for very narrow HP wedges ($\{a \cdot \tan \Theta\}/e = 1$) and decreases maximum temperatures by $\sim 20\%$ for infinitely wide HP wedges ($e = 0$).

6.4.2. AD component (Figures 6f, 6g, 6h, 6i, and 6j, and Table 3). Increasing convergence velocity lowers temperatures slightly throughout much of the upper plate, raises the maximum near-surface thermal gradient, but has little effect on lower plate temperatures. Temperatures are cooler at the subduction contact due to the increased efficiency of subduction of cold crust with respect to conductive thermal relaxation, while higher maximum near-surface thermal gradients are due to higher erosion rates (T_{60} , and $T/dz_{z=0}$).

6.4.3. Total thermal structures (HPD plus AD). Higher convergence velocity results in lower temperatures for both the HPD and AD thermal structures; thus temperatures for the total thermal structure will also decrease with increasing convergence velocity.

7. Synthesis of Results

Subduction, accretion, and erosion redistribute HP material, resulting in the formation of an HP wedge within the upper plate of collisional orogens. Maximum depth of the HP wedge and the rate of heat production are the primary factors controlling thermal structure. High temperatures at shallow levels ($>500^{\circ}\text{C}$ at depths of 20-30 km) result from the combination of moderately deep wedges and moderate to high rates of heat production; i.e., $d_w > 30$ km and $A > 2.5 \mu\text{W}/\text{m}^3$ or $d_w > 65$ km and $A > 1.25 \mu\text{W}/\text{m}^3$ (Figures 7a and 7b). Combinations of shallow wedges and low heat production rates result in thermal structures that are cooler than the foreland geotherm, indicating that conductive heat loss to the downgoing plate exceeds heating from the HP wedge. Inverted geotherms develop over a broad range of combinations of d_w and A , for example, $d_w > 35$ km with $A > 2.5 \mu\text{W}/\text{m}^3$ and $d_w > 65$ km with $A > 0.75 \mu\text{W}/\text{m}^3$ (Figure 8), while low values of heat production ($A < 0.5$) and/or shallow wedges ($d_w < 30$ km) do not produce temperature inversions. Higher convergence velocities reduce maximum temperatures; for example, doubling v_c , while holding A and d_w constant, reduces temperatures by about 20%.

Varying the surface width of the HP wedge changes the horizontal location of upper plate maximum temperatures and thus their vertical proximity to the underlying subduction boundary. For example, given $d_w = 44$ km and $s_w = 440$ km, T_{max} is located at $z = 34$ km and $x = 270$ km, 20 km above the subduction boundary. For the same wedge maximum depth and $s_w = 220$ km, T_{max} is located at $z = 32$ km and $x = 190$ km, 6 km above the subduction boundary.

Inverted geotherms develop within tens of millions of years, with the time required depending on the time needed to accumulate significant amounts of HP crust at intermediate

depths (>35 km) within the upper plate, roughly ~20 m.y. for $v_c = 20$ and ~10 m.y. for $v_c = 40$ km/m.y. High temperatures at shallow levels ($T > 500^\circ\text{C}$ at $z = 20\text{-}30$ km) also occur within tens of millions of years, with the time required depending on both the rate of growth of the HP wedge and the magnitude of the heat production rate; for example, 10-15 m.y. for $v_c = 40$ km/m.y. and $A = 2.5 \mu\text{W}/\text{m}^3$, and 45-55 m.y. for $v_c = 20$ km/m.y. and $A = 1.5 \mu\text{W}/\text{m}^3$.

8. Geologic Applications

A broad range of paleotemperatures and pressures are observed within orogenic systems. If, as is suggested by this study, only a few fundamental processes control the primary thermal structure of orogenic belts, then the relative importance of these processes must vary from belt to belt. Inspection of Figure 7 suggests that variations in A and d_w can lead to large differences in the maximum temperatures obtained at shallow levels, providing a reasonable explanation of the observed spectrum of temperature structures within orogenic belts.

For example, one of the best documented occurrences of inverted metamorphic field gradients is in the central Himalayan orogen, where steep to inverted isograds above a Miocene intracontinental subduction boundary (the Main Central thrust zone) are associated with maximum temperatures in excess of 600°C at paleodepths of 15-30 km [Hodges *et al.*, 1988; Hubbard, 1989; Pecher, 1989]. The development of steep to inverted field gradients, accompanied by significant crustal anatexis, began about 20-25 Ma in the central Himalayas, approximately 25-35 m.y. after the initiation of collision between India and Eurasia [Hubbard and Harrison, 1989; Hodges *et al.*, 1994; Searle *et al.*, 1988]. Rocks currently at the surface were at depths of 20-40 km during Miocene metamorphism [Hodges *et al.*, 1988; Pecher, 1989] and were subsequently denuded at averaged rates of 1-2 mm/yr. Additionally, extensive tracts of lower plate (Indian) rocks with an exposed surface width of the order of 300 km have been accreted episodically onto the upper (Eurasian) plate since the time of collision, yielding a vertical accretion rate of ~1.5 km/m.y. (for subduction angle of $\sim 15^\circ$). Paleosubduction rates are unconstrained, but modern rates of convergence across the Himalayas are ~10-25 mm/yr. [Lyon-Caen and Molnar, 1985]. Heat production rates for metamorphic and igneous rocks of the Himalayas range from ~1.5 to $>6 \mu\text{W}/\text{m}^3$, with a significant proportion (>25%) of reported values in excess of $4 \mu\text{W}/\text{m}^3$ [Scaillet *et al.*, 1990; Vidal *et al.*, 1982; Macfarlane, 1992].

Using these estimates as constraints on model parameters, model results at $t = 32$ m.y. show the development of inverted geotherms within the upper and lower plates with

maximum temperatures in excess of 600°C at depths from ~20 km to 40 km (Figure 9). A detailed discussion of metamorphism resulting from the model thermal structure is beyond the scope of this paper and is the focus of a separate paper (A. Huerta et al., The effects of accretion, erosion, and radiogenic heat on the metamorphic evolution of collisional orogens, submitted to *Tectonics*, 1998). However, Figure 9 shows that because particle paths are parallel to the solid arrows, a vertical column of rock passing through the region of high temperatures in the upper plate preserves an inverted geotherm as an inverted metamorphic gradient. The model thermal structure is compatible with observations of metamorphism from the Himalayas, and it preserves inverted geotherms, thus demonstrating that it is probably not necessary to appeal to postulated transient heat sources (e.g., frictional heating along faults like the Main Central thrust zone) or postmetamorphic structures to explain the Miocene metamorphism of the Himalayas.

As another example, the Franciscan complex represents a low-temperature high-pressure accretionary prism formed during Jurassic/Cretaceous subduction along the western coast of North America [Hamilton, 1969; Blake et al., 1988]. Composed of a number of tectonostratigraphic terranes, metamorphic grade increases from west to east, with estimated P-T conditions of ~250°C and 600 MPa in the west to maximum conditions of about 345°C and 800 MPa in the east [Blake et al., 1988, and references therein]. Accreted material consists of metasediments and basaltic metavolcanics, interpreted to be fragments of oceanic crust.

Using a low heat production rate to simulate subduction of oceanic crust ($A \approx 0.5 \mu\text{W}/\text{m}^3$) model temperatures consistent with observed conditions (of the order of 300° to 400°C at $z=20\text{-}30$ km) are computed for a broad range of d_w from <30 km to >65 km (Figures 7a, and 7b). There are numerous combinations of erosion and accretion rates which can result in wedge depths ranging from 30 to 65 km, indicating that in this situation, the thermal evolution is relatively insensitive to the magnitudes of erosion and accretion. These results emphasize the fact that the primary control on the thermal evolution of convergent orogens exclusive of arc settings is the redistribution of crust enriched in heat-producing elements into the upper plate by accretion and erosion.

9. Discussion

Unlike the transient heat sources postulated by other model studies, accretion and erosion are well-defined geologic processes known to operate in convergent orogens. When coupled with moderate rates of crustal heat production, these processes can result in high-grade metamorphism, partial melting, and the development of inverted geotherms at midcrustal levels. In addition, the broad range of metamorphic conditions associated with

orogenic belts can be explained by variations in the magnitudes of these processes. Although other processes, such as shear heating, magma migration, and fluid flow, may have an effect on the thermal evolution of the crust during orogenesis, model results show that thermal regimes consistent with observations can be reproduced solely by redistributing HP crustal material through accretion and erosion. Because surface erosion and basal accretion exert such a strong control on temperatures, we feel that thermal models that do not include these processes are inadequate representations of orogenic systems.

In the approach taken here, intraplate deformation is neglected, a process which could increase the maximum depth of the HP wedge in the upper plate and result in higher temperatures than predicted by our model. In addition, we have assumed that accretion is spatially and temporally continuous throughout the orogenic cycle, although accretion in real orogenic belts may occur episodically along a series of discrete thrust fault systems. Incorporation of these processes will not change the basic conclusions of this study, although they are aspects of orogenic systems worthy of investigation in the future.

Our results may also yield insight into the development of extensional structures within collisional orogens. Such structures have been recently recognized in a number of collisional systems, but the mechanisms which trigger episodic extension or “extensional collapse” remain unknown [Northrup, 1996; Burchfiel *et al.*, 1992, and references therein; Gee *et al.*, 1994; Hodges and Walker, 1992; Carmignani and Kligfield, 1990]. Results of this study suggest that orogens in which significant amounts of HP material are accreted to the upper plate may experience temperatures high enough for thermally induced weakening and/or melting of upper plate rocks, conditions which may precipitate extensional collapse. Thus accretion and erosion may indirectly provide the rheologic conditions necessary for development of the extensional features observed within many collisional orogens.

References

- Banks, D.A., G.R. Davies, B.W.D. Yardley, A.M. McCaig, and N.T. Grant, The chemistry of brines from an Alpine thrust system of the Central Pyrenees: An application of fluid inclusion analysis to the study of fluid behavior in orogenesis. *Geochim. Cosmochim. Acta*, 55, 1021-1030, 1991.
- Barr, T.D., and F.A. Dahlen, Brittle frictional mountain building, 2, Thermal structure and heat budget, *J. Geophys. Res.*, 94, 3923-3947, 1989.
- Barr, T.D., and F.A. Dahlen, Constraints on friction and stress in the Taiwan fold-and-thrust belt from heat flow and geochronology, *Geology*, 18, 111-115, 1990.
- Barton, M.D., and R.B. Hanson, Magmatism and the development of low-pressure metamorphic belts: Implications from the western United States and thermal modeling, *Geol. Soc. Am. Bull.*, 101, 1051-1065, 1989.
- Bird, P., Initiation of intracontinental subduction in the Himalaya, *J. Geophys. Res.*, 83, 4975-4987, 1978a.
- Bird, P., Stress and temperature in subduction shear zones: Tonga and Mariana, *Geophys. J. R. Astron. Soc.*, 55, 411-434, 1978b.
- Bird, P., M.N. Toksoz, and N.H. Sleep, Thermal and mechanical models of continent-continent convergence zones, *J. Geophys. Res.*, 80, 4405-4416, 1975.
- Blake, M.C., Jr., A.S. Jayko, and R.J. McLaughlin, Metamorphic and tectonic evolution of the Franciscan complex, northern California, in *Metamorphism and Crustal Evolution of the Western United States*, edited by W.G. Ernst, pp. 1035-1060, Prentice-Hall, Englewood Cliffs, N. J., 1988.
- Brace, W.F. and D.L. Kohlstedt, Limits on lithospheric stress imposed by laboratory experiments, *J. Geophys. Res.*, 85, 6248-6258, 1980.
- Brune, J.N., T.L. Henyey, and R. F. Roy, Heat flow, stress, and rate of slip along the San Andreas fault, California, *J. Geophys. Res.*, 74, 3821-3827, 1969.
- Burchfiel, B.C., Z. Chen, K.V. Hodges, Y. Liu, L.H. Royden, C. Deng, and J. Xu, The South Tibetan detachment system, Himalayan orogen: Extension contemporaneous with and parallel to shortening in a collisional mountain belt, 41 pp., *Geol. Soc. of Am.*, Boulder, Colo., 1992.
- Carmignani, L., and R. Kligfield, Crustal extension in the Northern Apennines: The transition from compression to extension in the Alpi Apuane core complex, *Tectonics*, 9, 1275-1303, 1990.
- Copeland, P., and T.M. Harrison, Episodic rapid uplift in the Himalaya revealed by $^{40}\text{Ar}/^{39}\text{Ar}$ analysis of detrital K-feldspar and muscovite, Bengal fan, *Geology*, 10, 354-357, 1990.
- Davies, J.H., and F. von Blanckenburg, Slab breakoff: A model of lithosphere detachment and its test in the magmatism and deformation of collisional orogens, *Earth Planet. Sci. Lett.*, 129, 85-102, 1995.
- De Yoreo, J.J., D.R. Lux, and C.V. Guidotti, Thermal modeling in low-pressure/high-temperature metamorphic belts, *Tectonophysics*, 188, 209-238, 1991.
- England, P., and P. Molnar, The interpretation of inverted metamorphic isograds using simple physical calculations, *Tectonics*, 12, 145-157, 1993.

- England, P.C., and A. Thompson, Some thermal and tectonic models for crustal melting in continental collision zones, in *Collision Tectonics*, edited by M.P. Coward and A.C. Ries, *Geol. Soc. Spec. Publ.*, 19, 83-94, 1986.
- England, P., P. Le Fort, P. Molnar, and A. Pecher, Heat Sources for Tertiary Metamorphism and Anatexis in the Annapurna-Manaslu Region Central Nepal, *J. Geophys. Res.*, 97, 2107-2128, 1992.
- Ferry, J.M., A case study of the amount and distribution of heat and fluid during metamorphism, *Contrib. Mineral. Petrol.*, 71, 373-385, 1980.
- Ferry, J.M., Overview of the petrologic record of fluid flow during regional metamorphism in northern New England, *Am. J. Sci.*, 294, 905-988, 1994.
- Ferry, J.M., and G.M. Dipple, Fluid flow, mineral reactions, and metasomatism, *Geology*, 19, 211-214, 1991.
- Gee, D.G., M. Lobkowitz, and S. Singh, Late Caledonian extension in the Scandinavian Caledonides—The Roragen Detachment revisited, *Tectonophysics*, 231, 139-155, 1994.
- Graham, C.M., and R. Powell, A garnet-hornblende geothermometer: Calibration, testing, and application to the Pelona Schist, southern California, *J. Metamorph. Geol.*, 2, 13-31, 1984.
- Hamilton, W., Mesozoic California and the underflow of Pacific mantle, *Geol. Soc. Am. Bull.*, 80, 2409-2430, 1969.
- Hodges, K.V., and J.D. Walker, Extension in the Cretaceous Sevier orogen, North American Cordillera, *Geol. Soc. Am. Bull.*, 104, 560-569, 1992.
- Hodges, K.V., M.S. Hubbard, and D.S. Silverberg, Metamorphic constraints on the thermal evolution of the central Himalayan Orogen, *Philos. Trans. R. Soc. London., Ser. A*, 326, 257-280, 1988.
- Hodges, K.V., W.E. Hames, W. Olszewski, B.C. Burchfiel, L.H. Royden, and Z. Chen, Thermobarometric and $^{40}\text{Ar}/^{39}\text{Ar}$ geochronologic constraints on Eohimalayan metamorphism in the Dinggye area, southern Tibet, *Contrib. Mineral. Petrol.*, 117, 151-163, 1994.
- Hoisch, T.D., C.F. Miller, M.T. Heitzler and E.F. Stoddard, Late Cretaceous regional metamorphism in southeastern California, in *Metamorphism and Crustal Evolution in the Western Conterminous United States, Rubey Volume VII*, edited by W.G. Ernst, pp. 538-571, Prentice-Hall, Englewood Cliffs, N.J., 1988.
- Houseman, G.A., D.P. McKenzie, and P. Molnar, Convective instability of a thickened boundary layer and its relevance for the thermal evolution of continental convergent belts, *J. Geophys. Res.*, 86, 6115-6132, 1981.
- Hubbard, M.S., Thermobarometric constraints on the thermal history of the Main Central Thrust Zone and Tibetan Slab, eastern Nepal Himalaya, *J. Metamorph. Geol.*, 7, 19-30, 1989.
- Hubbard, M.S., and T.M. Harrison, $^{40}\text{Ar}/^{39}\text{Ar}$ age constraints on deformation and metamorphism in the Main Central thrust zone and Tibetan slab, eastern Nepal Himalaya, *Tectonics*, 8, 865-880, 1989.
- Hubbard, M., L. Royden, and K. Hodges, Constraints on unroofing rates in the High Himalaya, eastern Nepal, *Tectonics*, 10, 287-298, 1991.
- Huerta, A.D., L. Royden, and K. Hodges, The interdependence of deformational and thermal processes in mountain belts, *Science*, 273, 637-639, 1996.

- Jamieson, R.A. C. Beaumont, J. Hamilton, and P. Fullsack, Tectonic assembly of inverted metamorphic sequences, *Geology*, 24, 838-842, 1996.
- Kirby, S.H., and J.W. McCormick, Inelastic properties of rocks and minerals; strength and rheology, in *Practical Handbook of Physical Properties of Rocks and Minerals*, edited by R.S. Carmichael, pp. 583-596, CRC Press, Boca Raton, Fla., 1989.
- Lachenbruch, A.H., and J.H. Sass, Heat flow and energetics of the San Andreas fault zone, *J. Geophys. Res.*, 85, 6185-6222, 1980.
- Li, Y.H., Denudation of Taiwan Island since the Pliocene Epoch, *Geology*, 4, 105-107, 1976.
- Lyon-Caen, H., and P. Molnar, Gravity anomalies, flexure of the Indian plate, and the structure, support, and evolution of Himalaya and Ganga Basin, *Tectonics*, 4, 513-538, 1985.
- Macfarlane, A.M., *The tectonic evolution of the core of the Himalaya, Langtang National Park, central Nepal*, Ph.D. thesis, Mass. Inst. of Technol., Cambridge, 1992.
- Macfarlane, A.M., An evaluation of the inverted metamorphic gradient at Langtang National Park, central Nepal Himalaya, *J. Metamorph. Geol.*, 13, 595-612, 1995.
- Molnar, P. and P. England, Temperatures, heat flux, and frictional stress near major thrust faults, *J. Geophys. Res.*, 95, 4833-4856, 1990.
- Northrup, C.J., Structural expressions and tectonic implications of general noncoaxial flow in the midcrust of a collisional orogen: The northern Scandinavian Caledonides, *Tectonics*, 15, 490-505, 1996.
- Oxburgh, E.R., and D.L. Turcotte, Thermal gradients and regional metamorphism in overthrust terrains with special reference to the eastern Alps, *Schweiz. Mineral. Petrogr. Mitt.*, 54, 641-662, 1974.
- Pecher, A., The metamorphism in the central Himalaya, *J. Metamorph. Geol.*, 7, 31-41, 1989.
- Royden, L.H., The steady state thermal structure of eroding orogenic belts and accretionary prisms, *J. Geophys. Res.*, 98, 4487-4507, 1993.
- Sacks, P.E., and D.T. Secor Jr., Delamination in collisional orogens, *Geology*, 18, 999-1002, 1990.
- Scaillot, B.C., P. France-Lanord, and P. Le Fort, Badrinath-Gangotri plutons (Garhwal, India): Petrological and geochemical evidence for fractionation processes in a high Himalayan leucogranite. *J. Volcanol. Geotherm. Res.*, 44, 163-188, 1990.
- Scholz, C.H., Shear heating and the state of stress on faults, *J. Geophys. Res.*, 85, 6174-6184, 1980.
- Scholz, C.H., J. Beavan, and T.C. Hanks, Frictional metamorphism, argon depletion, and tectonic stress on the Alpine Fault, New Zealand, *J. Geophys. Res.*, 84, 6770-6781, 1979.
- Sclater, J.G., C. Jaupart, and D. Galson, The heat flow through oceanic and continental crust and the heat loss of the Earth, *Rev. Geophys.*, 18, 269-311, 1980.
- Sclater, J.G., B. Parsons, and C. Jaupart, Oceans and continents: Similarities and differences in the mechanisms of heat loss, *J. Geophys. Res.*, 86, 11,535-11,552, 1981.

- Searle, M.P., D.J.W. Cooper, and A.J. Rex, Collision tectonics of the Ladakh-Zaskar Himalaya, in *Tectonic Evolution of the Himalayas and Tibet*, edited by R.M. Shackleton, J.F. Dewey, and B.F. Windley, pp. 117-149, R. Soc., London, 1988.
- Van Schmus, W.R., Radioactive properties of minerals and rocks, in *Practical Handbook of Physical Properties of Rocks and Minerals*, edited by R.S. Carmichael, pp. 583-596, CRC Press, Boca Raton, Fla., 1989.
- Vidal, P., A. Cocherie, and P. Le Fort, Geochemical investigations of the origin of the Manaslu leucogranite (Himalaya, Nepal), *Geochim. Cosmochim. Acta*, 46, 2279-2292, 1982.
- Yardley, B.W.D., J.P. Barber, and J.R. Gray, The metamorphism of the Dalradian rocks of western Ireland and its relation to tectonic setting, *Philos. Trans. R. Soc. London, Ser. A*, 321, 243-270, 1987.
- Zoback, M.D et al., New evidence on the state of stress of the San Andreas fault system, *Science*, 238, 1105-1111, 1987.

K. Hodges, A. Huerta, and L. Royden, and Department of Earth, Atmospheric and Planetary Geology, Massachusetts Institute of Technology, Cambridge, MA 02139. (e-mail: aud@mit.edu)

(Received August, 22, 1996; revised January 22, 1998; accepted February 3, 1998.)

Copyright 1998 by the American Geophysical Union.

Paper number 98JB00593.
0148-0227/98/98JB-00593\$09.00

Figures

Figure 1. (a) Model geometry used to simulate the thermal evolution of collisional orogens. Material is accreted from the lower plate to the upper plate at rate a (vertical component relative to subduction contact) and removed at the surface at rate e . Dip of the subduction zone, Θ , and convergence velocity, v_c , are assumed constant. At steady state, a wedge of heat-producing crust within the upper plate has a maximum depth d_w and a surface width s_w . (b) Particle paths in two frames of reference. (top) No accretion or erosion, particle paths are identical in both frames of reference. (middle) Frame of reference in which the subduction zone moves with respect to the frame of reference. (bottom) Frame of reference fixed to the toe of the upper plate ($a' = a \tan \Theta$, $e' = e \tan \Theta$).

Figure 2. Cross sections showing the growth of the wedge of heat-producing material within the upper plate of a collisional zone and the thermal evolution from $t=0$ (initiation of collision) to thermal steady state. Contours are isotherms with contour interval of 100°C , stippled pattern is area of heat-producing crust, and heavy line shows the position of the subduction surface. (a) Evolution for convergence rate $v_c=20$ km/m.y., accretion rate $a=2.0$ km/m.y., erosion rate $e=1.0$ km/m.y., and heat production rate $A=1.75$ $\mu\text{W}/\text{m}^3$. (b) Evolution for convergence rate $v_c=20$ km/m.y., accretion rate $a=1.5$ km/m.y., erosion rate $e=0.9$ km/m.y., and heat production rate $A=1.75$ $\mu\text{W}/\text{m}^3$. (c) Evolution for convergence rate $v_c=20$ km/m.y., accretion rate $a=2.0$ km/m.y., erosion rate $e=1.0$ km/m.y., and heat production rate $A=3.0$ $\mu\text{W}/\text{m}^3$. See text for further discussion. (Parameters are listed in Table 2.)

Figure 3. Steady state temperatures as a function of subduction angle (Θ) for constant vertical component of lower plate velocity ($w_l=3.9$ km/m.y.). Heavy lines shows position of subduction contact. (a)-(d) The component of thermal structure due to heat production within the crust (with $T_a=0$). Dashed lines show geometry of wedge of heat production material. (e)-(h) The component of thermal structure due to heat from the asthenosphere (with $A=0$). Dashed line shows representative particle path with arrows scaled to legend. See text for further discussion. (Parameters are listed in Table 2.)

Figure 4. Steady state temperatures as a function of depth to the base of the wedge of heat production material (d_w). Heavy lines shows position of subduction contact. (a)-(c) The component of thermal structure due to heat production within the crust (with $T_a=0$). Dashed lines show geometry of wedge of heat production material. (d)-(f) The component of thermal structure due to heat from the asthenosphere (with $A=0$). Dashed line shows representative particle path with arrows scaled to legend. (Parameters are listed in Table 2.)

Figure 5. Steady state temperatures as a function of the surface width of the wedge of heat production material (s_w). Heavy lines shows position of subduction contact. (a)-(c) The component of thermal structure due to heat production within the crust (with $T_a=0$). Dashed lines show geometry of wedge of heat production material. (d)-(f) The component of thermal structure due to heat from the asthenosphere (with $A=0$). Dashed line shows representative particle path with arrows scaled to legend. See text for further discussion. (Parameters are listed in Table 2.)

Figure 6. Steady state temperatures as a function of convergence velocity (v_c). Heavy lines shows position of subduction contact. (a)-(e) The component of thermal structure due to heat production within the crust (with $T_a=0$). Dashed lines show geometry of wedge of heat production material. (f)-(j) The component of thermal structure due to heat from the asthenosphere (with $A=0$). Dashed line shows representative particle path with arrows scaled to legend. See text for further discussion. (Parameters are listed in Table 2.)

Figure 7. Maximum upper plate temperatures as a function of heat production rate (A) and depth to the base of the heat-producing wedge (d_w) (a) at $z=20$ km, and (b) at $z=30$ km. Hatched area indicates that temperatures within the orogen are cooler than foreland temperatures. (Parameters are listed in Table 2.)

Figure 8. Maximum upper plate temperatures for combinations of heat production rate (A) and depth to the base of the heat-producing wedge (d_w) which result in inverted

geotherms. Hatched area indicates conditions that do not yield inverted geotherms within the upper plate. See text for further discussion.

Figure 9. Computed temperatures 32 m.y. after initiation of collision, based on parameters consistent with the range of values estimated for the Himalaya ($v_c=20$ km/m.y., $a=1.8$ km/m.y., $e=1.2$ km/m.y., $A=3.0 \mu\text{W}/\text{m}^3$). Solid arrow shows particle trajectories in upper plate. White line shows locations where rocks achieve maximum temperatures as they are advected through the orogen.

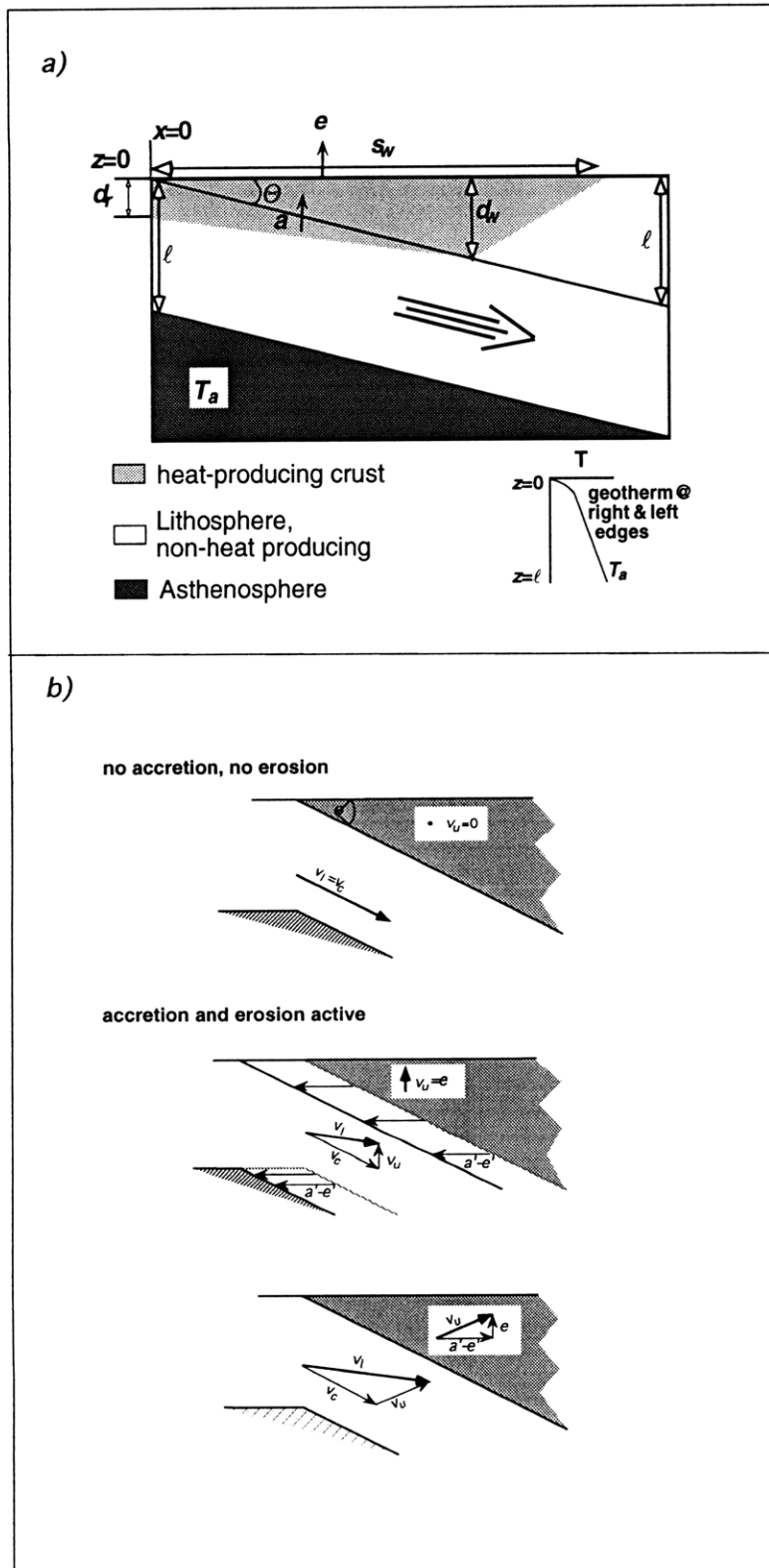
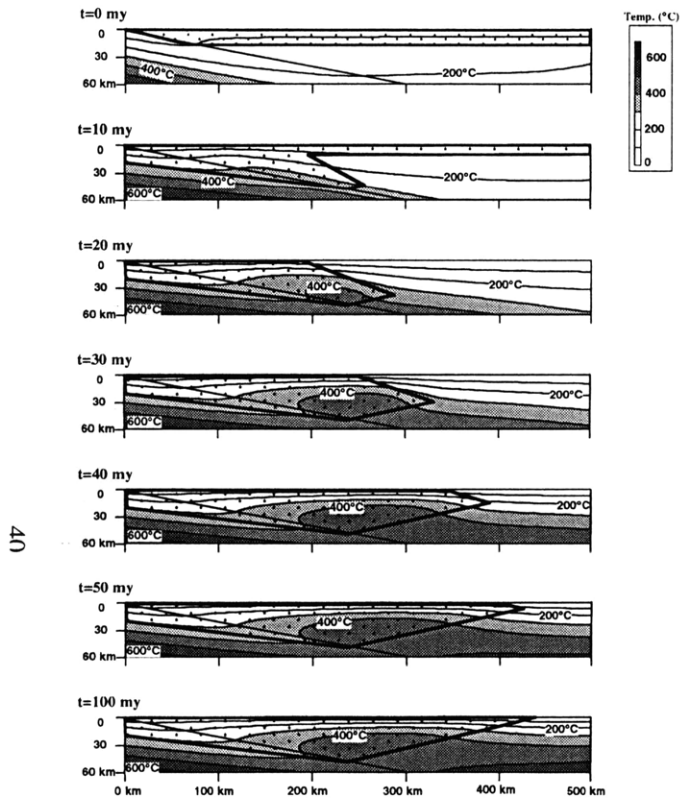


Figure 1

a) $v_c=20$ km/my, $a=2.0$ km/my, $e=1.0$ km/my, $A=1.75 \mu\text{W/m}^2$



b) $v_c=20$ km/my, $a=1.5$ km/my, $e=0.9$ km/my, $A=1.75 \mu\text{W/m}^2$

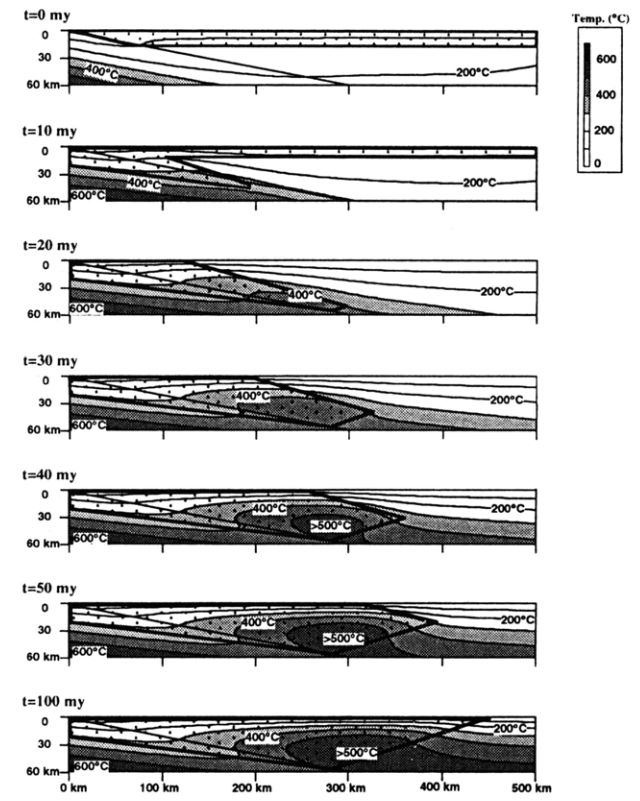


Figure 2

Figure 2, cont.

c)

$v_c = 20 \text{ km/my}$, $a = 2.0 \text{ km/my}$, $e = 1.0 \text{ km/my}$, $A = 3.0 \mu\text{W/m}^2$

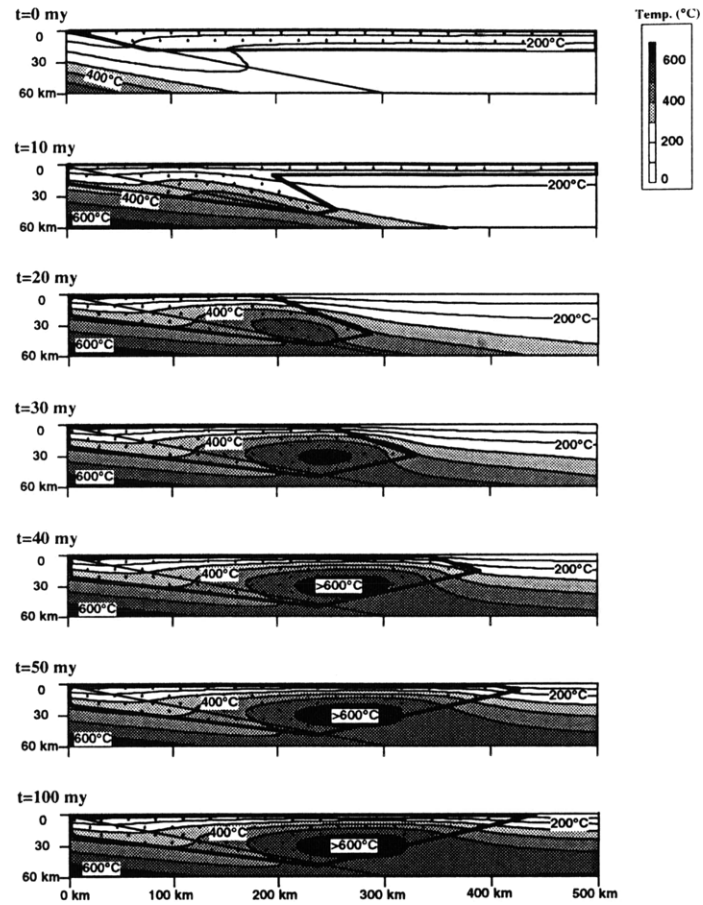


Figure 2, cont.

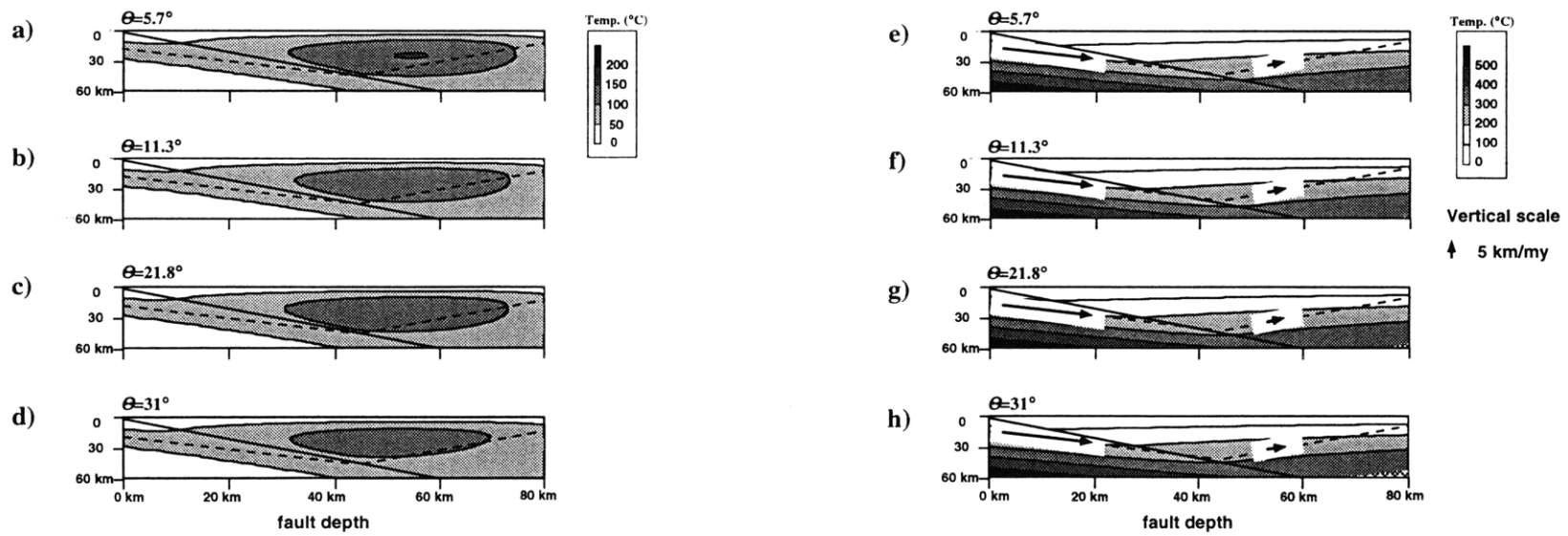


Figure 3

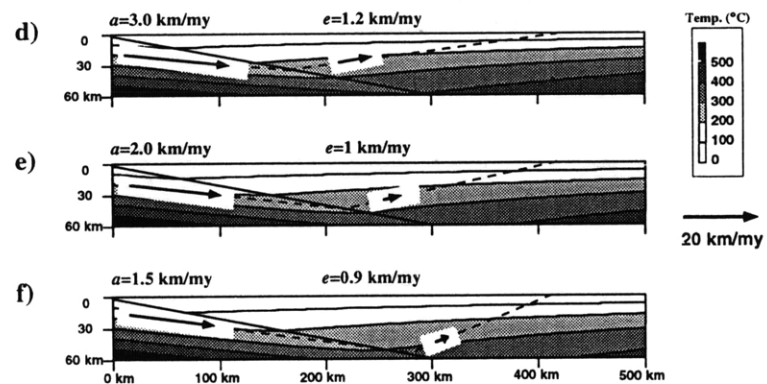
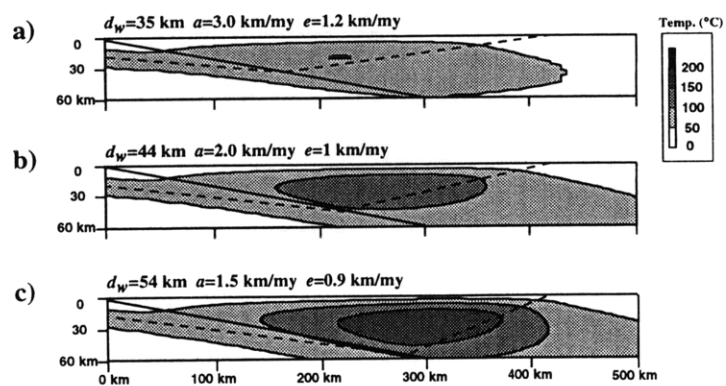


Figure 4

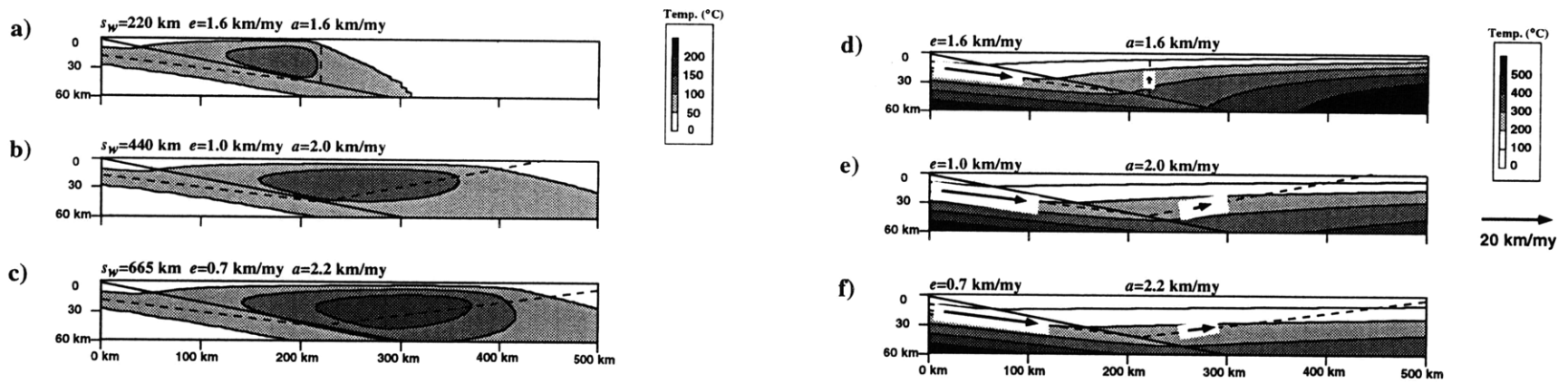


Figure 5

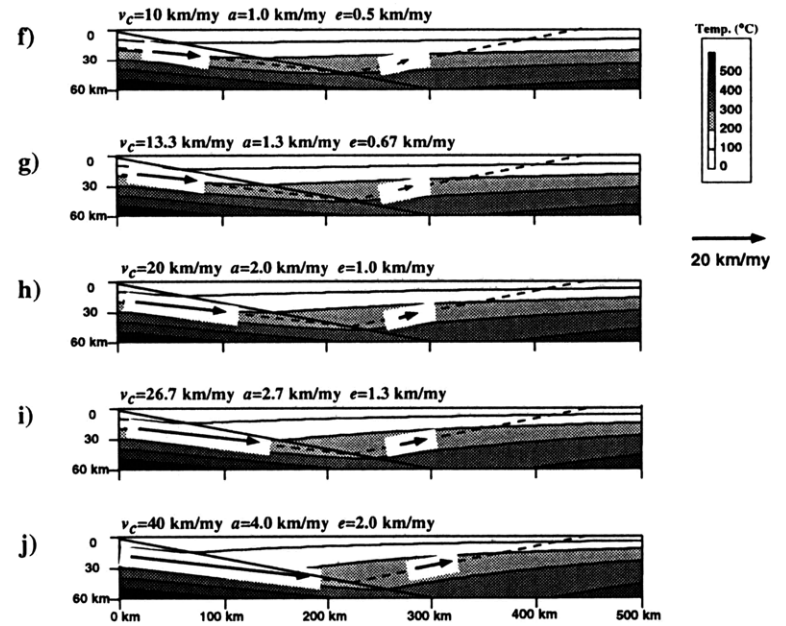
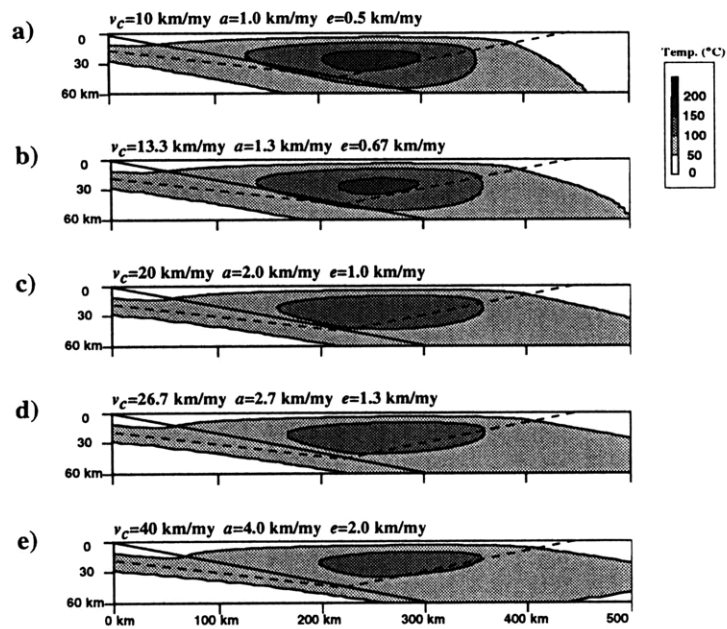


Figure 6

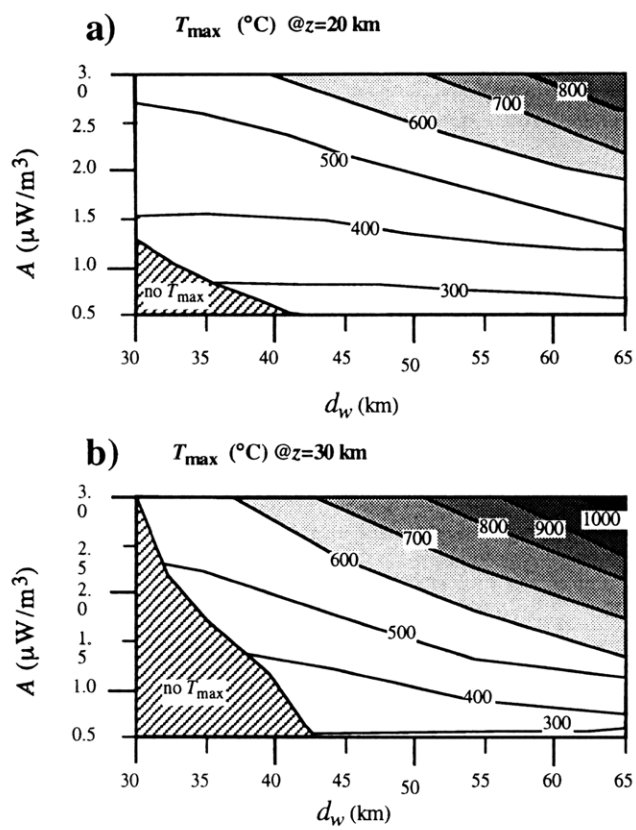


Figure 7

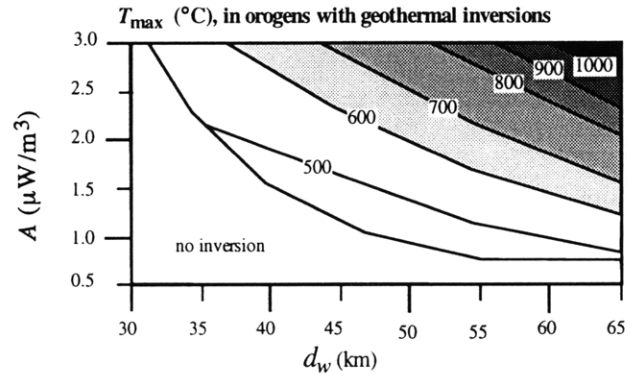


Figure 8

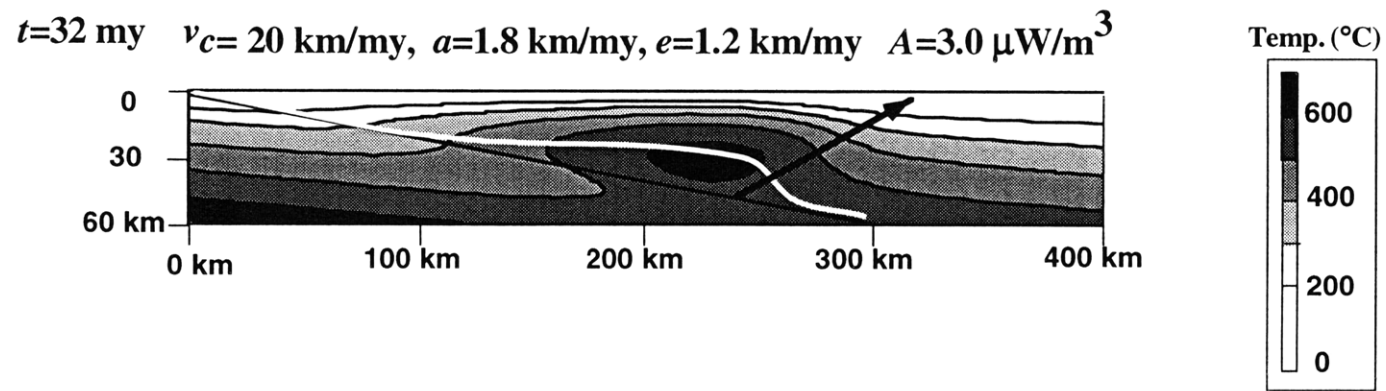


Figure 9

Table 1. Definitions of Variables and Values Used

Variable	Physical Meaning	Value or Units	Comment
a	accretion rate	km/m.y.	vertical component relative to fault contact
e	erosion rate	km/m.y.	
v_c	convergence velocity	km/m.y.	far-field velocity of downgoing plate relative to upper plate
Θ	dip of subduction zone	deg	
A	heat production rate of crust enriched in heat-producing elements	$\mu\text{W/m}$	
d_r	initial thickness of crust enriched in heat-producing elements	18 km	
l	thickness of foreland lithosphere	126 km	
T_a	temperature at base of lithosphere	1260°C	
K	thermal conductivity	2.5 W/mK	
α	thermal diffusivity	$10^{-6} \text{ m}^2/\text{s}$	
τ	time step for thermal model	0.05 m.y.	
Δz	vertical grid spacing	2 km	
Δx	horizontal grid spacing	km	$\Delta z/\tan\Theta$
x	horizontal distance from upperplate toe	km	$x=0$ is upper plate toe
z	vertical distance from surface	km	
w	vertical particle velocity	km/m.y.	w_u in upper plate, w_l in lower plate
u	horizontal particle velocity	km/m.y.	u_u in upper plate, u_l in lower plate
s_w	maximum width of HP wedge at surface	km	
d_w	maximum depth of HP wedge	km	
t_w	time to full development of HP wedge	m.y.	
t	time since initiation of collision	m.y.	
t_s	time to thermal steady state of orogen	m.y.	
T	temperature	°C	
T_{\max}	temperature maximum within upper plate	°C	
$x_{T_{\max}}$	horizontal location of T_{\max}	km	
$y_{T_{\max}}$	vertical location of T_{\max}	km	
T_{60}	temperature at subduction contact at $z=60$ km	°C	
$dT/dz_{z=0}$	near-surface thermal gradient	°C/km	

Table 2. Values of Parameters Used in Computing Temperatures in Figures 2-6 and 9

Figure	Convergence Rate v_c , km/m.y.	Accretion Rate a , km/m.y.	Erosion Rate e , km/m.y.	Heat Production A , $\mu\text{W}/\text{m}^3$	Fault Dip, θ	Maximum Depth of Wedge d_w , km	Surface Width of Wedge s_w , km	Time to Full Development of Wedge t_w , m.y.
2 a	20	2.0	1.0	1.75	$\tan\theta=0.2$	44	440	53
2 b	20	1.5	0.9	1.75		54	450	72
2 c	20	2.0	1.0	3.0		44	440	53
3 a, e	39.5	2.0	1.0	0 and 1.0	$\tan\theta=0.1$	44	887	53
3 b, f	20.0				$\tan\theta=0.2$		440	53
3 c, g	10.6				$\tan\theta=0.4$		222	53
3 d, h	7.6				$\tan\theta=0.6$		147	53
4 a, d	20	3.0	1.2	0 and 1.0	$\tan\theta=0.2$	35	440	36
4 b, e		2.0	1.0			44		53
4 c, f		1.5	0.9			54		71
5 a, d	20	1.6	1.6	0 and 1.0	$\tan\theta=0.2$	44	220	37
5 b, e		2.0	1.0				440	53
5 c, f		2.2	0.7				665	71
6 a, f	10.0	1.0	0.5	0 and 1.0	$\tan\theta=0.2$	44	440	107
6 b, g	13.3	1.3	0.67					80
6 c, h	20.0	2.0	1.0					53
6 d, i	26.7	2.7	1.3					40
6 e, j	40.0	4.0	2.0					27
9	20	1.8	1.2	3.0	$\tan\theta=0.2$	45	340	48

Unless otherwise specified, the following values are used in all figures. thermal diffusivity, $\alpha=10^{-6} \text{ m}^2/\text{s}$; thermal conductivity, $K=2.5 \text{ W/mK}$; lithospheric thickness, $l=126 \text{ km}$; initial thickness of HPE-enriched layer, $d_r=18 \text{ km}$; basal lithospheric temperature, $T_a=1260^\circ\text{C}$

Table 3. Temperatures and Surface Thermal Gradients for Figures 3–6

$T_a=0$					$A=0$			
Figure	Varied Parameter	T_{max} , °C	x_{Tmax} , km	z_{Tmax} , km	Figure	Varied Parameter	T_{60} *, °C	$dT/dz_{z=0}$ † °C/km
3a	$\tan \Theta=0.1$	151	520	24	3e	$\tan \Theta=0.1$	364	13
3b	$\tan \Theta=0.2$	145	260	24	3f	$\tan \Theta=0.2$	366	13
3c	$\tan \Theta=0.4$	144	130	24	3g	$\tan \Theta=0.4$	372	13
3d	$\tan \Theta=0.6$	128	83	22	3h	$\tan \Theta=0.6$	385	13.5
4a	$d_w=35$ km	101	220	20	4d	$d_w=35$ km	407	15
4b	$d_w=44$ km	145	260	24	4e	$d_w=44$ km	366	13
4c	$d_w=54$ km	199	300	28	4f	$d_w=54$ km	341	12
5a	$s_w=220$ km	134	190	20	5d	$s_w=220$ km	426	25.5
5b	$s_w=440$ km	145	260	24	5e	$s_w=440$ km	366	13
5c	$s_w=665$ km	153	310	26	5f	$s_w=665$ km	342	9.5
6a	$v_c=10$ km/m.y.	169	250	28	6f	$v_c=10$ km/m.y.	391	10
6b	$v_c=13.3$ km/m.y.	161	250	26	6g	$v_c=13.3$ km/m.y.	381	11
6c	$v_c=20$ km/m.y.	145	260	24	6h	$v_c=20$ km/m.y.	366	13
6d	$v_c=26.7$ km/m.y.	139	270	24	6i	$v_c=26.7$ km/m.y.	355	14.5
6e	$v_c=40$ km/m.y.	123	280	20	6j	$v_c=40$ km/m.y.	342	18

*Temperature at fault contact.

†Near-surface thermal gradient at $x=400$ km.

CHAPTER 3:

THE EFFECTS OF ACCRETION, EROSION, AND RADIOGENIC HEAT ON THE METAMORPHIC EVOLUTION OF COLLISIONAL OROGENS.

AUDREY D. HUERTA, LEIGH H. ROYDEN & KIP V. HODGES

Submitted to *Journal of Metamorphic Geology*, June 1998

Abstract

Petrologic and thermochronologic data provide our best record of the thermal structure of deeply eroded orogens, and, in principle, might be used to relate the metamorphic structure of an orogen to its deformational history. In this paper, we present a two-dimensional thermal model of collisional orogens that includes the processes of accretion and erosion to examine the pressure-temperature evolution of rocks advected through the orogen. In particular, we show that peak metamorphic temperatures within the core of a collisional orogen and distance from the toe of an orogen to the metamorphic core can be related to the relative rates of accretion, erosion, and plate convergence. Orogens displaying high metamorphic temperatures ($>600^{\circ}\text{C}$) are associated with low ratios of accretion rate to plate convergence velocity and with high heat flow through the foreland. Orogens with metamorphic cores far from the toe of the orogen are associated with high ratios of accretion rate to erosion rate.

Calculated metamorphic patterns are similar to those observed in the field and suggest reconsideration of the concept that the metamorphic record does not closely reflect geothermal gradients within an orogen. Calculated metamorphic gradients commonly mimic steady-state geotherms, and inverted thermal gradients can be preserved in the metamorphic record. In addition, specific combinations of accretion and erosion rates can result in metamorphic gradients that not only mimic steady-state geotherms, but preserve lithostatic gradients as well.

Introduction

An important goal in geologic research is to relate the metamorphic record of orogens to the basic processes of mountain building. Most thermomechanical models of the orogenic process have been unable to reproduce the high-temperature, low-pressure metamorphic conditions observed in real orogens without relying on the *ad hoc* introduction of speculative orogenic processes (e.g., mantle delamination, very high rates of shear heating along the subduction contact). However, recent numerical experiments indicate that accretion of heat-producing crust from the down-going plate to the overriding plate and surface erosion during collisional orogeny can greatly increase temperatures in model orogens and produce thermal conditions consistent with the observed metamorphic grades (Huerta *et al.*, 1996; 1998).

In light of these promising results, we further explore the effects of erosion and accretion on the pressure-temperature histories of metamorphic rocks and the distribution of metamorphic isograds in orogenic systems. Ultimately, our goal is to ask whether, and to what extent, pressure, temperature and cooling data can be useful in reconstructing the processes responsible for the observed metamorphism, and determining at what rates these processes occur.

Constraints on the metamorphic evolution of orogens

Numerous geochemical methods may be used to help reconstruct the temperature and pressure evolution of rocks as they are cycled through an orogenic system (Ghent *et al.*, 1988; Hodges, 1991; Spear, 1993). For example, temperatures and pressures at final equilibrium can be determined with reasonable precision (± 20 - 50° C and ± 100 - 150 MPa) by applying various major element thermobarometers (Hodges & McKenna, 1987; Essene, 1989; Hodges, 1991; Kohn & Spear, 1991a; Kohn & Spear, 1991b), analysis of compositionally zoned porphyroblasts and their inclusions yields information on the earlier pressure-temperature (PT) history (Spear & Selverstone, 1983; Spear, 1993), and the temperature-time (Tt) history of a sample can be constrained using isotopic thermochronometers with closure temperatures ranging from $>700^\circ$ C (U-Pb zircon) to $\sim 100^\circ$ C (fission track annealing in apatite) (McDougal & Harrison, 1988; Heaman & Parrish, 1991).

Unfortunately, most thermobarometric techniques recover the high-temperature portion of a rock's PT path, rather than the low-temperature portion which includes the closure temperatures of most isotopic thermochronometers. As a consequence, it is very difficult to reconstruct most of the pressure-time (Pt) path of a metamorphic terrain directly from

petrologic and geochemical data. Inasmuch as the Pt path is a valuable proxy for the burial and unroofing history of orogenic belts, many attempts have been made to use forward and inverse models to compensate for the limited temperature overlap between recovered PT and Tt paths (e.g., England & Richardson, 1977; Dahlen & Barr, 1989; Royden, 1993; Molnar & England, 1990; Royden & Hodges, 1984; Ruppel & Hodges, 1994). In this paper, we extend these efforts to include a new, relatively simple numerical model of collisional orogenesis that emphasizes the importance of accretion and erosion in the thermal evolution of mountain ranges (Huerta *et al.*, 1996; 1998). We begin with the hypothesis that these processes play such a dominant role in orogenic heat transfer that the metamorphic structure of any given mountain range reflects the absolute and relative rates of erosion and accretion during mountain building. We then explore how variations in these two processes should be manifested in the distribution of metamorphic isograds and in the topology of PTt paths across the orogen.

To avoid possible ambiguities we define the following terminology to describe model results presented in this paper (see Table 1 for symbols, variables, and values used). T_{max} is the maximum temperature experienced by a rock, z_m is the depth of the rock at T_{max} , and t_m is the time at which the rock reaches T_{max} (in millions of years before the rock reaches the surface). Metamorphic field gradients are displayed as a function of the horizontal distance from the toe of the orogen (x) including temperature arrays (T_{max} vs. x), depth arrays (z_m vs. x), and metamorphic age arrays (t_m vs. x). We use the term metamorphic core to describe the region at the surface where metamorphic temperatures are at a local maximum (peak T_{max}). Geotherms (profiles of T as a function of depth), either transient or steady state, display the thermal structure of a crustal column within the orogen at any one time, while piezothermic arrays (profiles of T_{max} as function of depth at T_{max}) refer to the array of peak metamorphic conditions experienced by rocks along a transect (e.g., Richardson & England, 1979). The structural position (z_{struct}) of a rock along a transect is the distance measured perpendicular to the subduction boundary from the top of the transect to the rock. Pressure-depth profiles (arrays of z_m as a function of z_{struct}) display the relationship between the structural position and the metamorphic depth of rocks along the transect.

Thermal model

In this paper we use the approach described in Huerta *et al.* (1996; 1998) to mimic the effects of convergence, accretion and erosion within collisional orogens. In this model, “continental” lithosphere (with heat-producing crust distributed uniformly above a depth of

d_r) is subducted beneath an upper plate of continental lithosphere along a planar subduction contact with constant dip Θ (Fig. 1). Accretion transfers material from the down-going plate to the upper plate across the subduction boundary (at rate a , measured vertically with respect to the subduction boundary), while erosion removes material from the surface of the upper plate (at rate e). Convergence velocity (v_c) is defined as the velocity of rocks in the down-going plate with respect to rocks in the upper plate. Initial temperatures are obtained by subducting an “oceanic” plate (no heat-producing crust) beneath the upper plate with no erosion or accretion until steady-state conditions are achieved. At the time of collision ($t=0$) continental lithosphere (with heat-producing crust) in the down-going plate enters the orogenic system, and accretion and erosion are initiated. (For simplicity, this approach ignores internal deformation within the down-going or upper plate).

We use a frame of reference fixed with respect to the toe of the upper plate in order to eliminate computational complications that arise in a reference frame that is not stationary with respect to the subduction boundary. To illustrate this point, Fig. 2 shows particle paths in two frames of reference, one fixed to the toe of the upper plate (lower panel), and a more familiar frame of reference that does not move horizontally with respect to rocks in the upper plate (middle panel). When erosion and accretion rates are zero, particle paths in the two frames of reference are identical (upper panel); rocks in the upper plate are stationary, and rocks in the down-going plate move parallel to the subduction contact at the convergence velocity. The two frames of reference present very different views when a and e are non-zero. In the more familiar frame of reference (lower panel), rocks in the upper plate move vertically upwards at a rate e , and the subduction contact moves horizontally with velocity $(a-e)/\tan\Theta$. Rocks in the down-going plate move at a velocity that is the sum of the upper plate velocity and the convergence velocity. This frame of reference is cumbersome, since accretion continually moves the toe of the upper plate with respect to the frame and the thickness of the upper plate changes with time at any position. Such complications are eliminated if we use a reference frame fixed to the toe of the upper plate. In this case (middle panel), the velocity of upper plate rocks has a horizontal component $(a-e)/\tan\Theta$ and a vertical component $-e$, the subduction boundary is stationary, and the velocity of rocks in the down-going plate is, as before, the sum of the upper plate velocity and the convergence velocity.

During subduction, the accretion of heat-producing crust from the down-going plate to the upper plate results in the development of a wedge of heat-producing crust in the upper plate. The wedge grows with time until a steady-state geometry is attained. At this time, the surface width of the wedge is such that the amount of heat-producing crust removed from

the surface by erosion equals the amount of heat-producing crust accreted to the upper plate. The steady-state size of the wedge is a function of the initial thickness of the heat-producing layer in the down-going plate, convergence velocity, erosion rate, accretion rate, and subduction angle. For cases where $e \neq 0$, the wedge reaches a steady-state shape by time:

$$t_w = \left[\frac{d_r}{e} \right] * \left[1 + \frac{v_c}{a} * \sin \theta \right], \quad \text{Equation 1}$$

with a steady-state maximum depth (d_w) and surface width (s_w) of:

$$d_w = \left[\frac{d_r}{a} \right] * [a - e + v_c \tan \theta] \quad \text{Equation 2}$$

$$s_w = d_w * \left[\frac{a}{e * \tan \theta} \right]. \quad \text{Equation 3}$$

This redistribution of heat-producing crust is a crucial factor in determining the thermal and metamorphic history of an orogen, and heat production within the wedge can be a significant part of the overall heat budget. For example, Huerta *et al.* (1996; 1998) have shown that the depth of the wedge and the magnitude of the heat production rate (A) within the wedge exert primary control on the magnitude of temperatures within the orogen, while the width of the wedge determines the lateral extent of high temperatures within the upper plate.

As the heat-producing wedge grows and erosion brings rocks towards the surface, temperatures throughout the orogen increase until a steady-state thermal regime is achieved. In general, temperatures within an orogen will come to a steady state by $t \sim 1.5 t_w$, and orogens with quickly developing wedges can come to thermal steady state within tens of millions of years. For example, Figure 3 shows the thermal evolution of a convergent zone as it evolves from the cool oceanic subduction regime to the steady-state thermal structure of a collisional orogen. Early in the evolution of the orogen, temperatures increase rapidly; by $t=40$ my, upper plate temperatures are in excess of 545°C at $z=40$ km. From $t=40$ my to $t=70$ my, temperatures continue to increase slowly. At $t=70$ my, the heat-producing wedge is fully developed ($t_w=69$ my), with maximum upper plate temperatures of 637°C , or 98% of the maximum steady-state temperature. By $t=100$ my, temperatures across the orogen have reached steady state, with a maximum upper plate temperature of 647°C . The elapsed time to thermal a steady state for a particular location is directly related to the time it takes for a rock to travel from $x=0$ to that location, which itself is a function both of location and

the advective rates. In general, temperatures in the region of the heat-producing wedge are within 98% of steady-state temperatures by $t=t_w$.

Steady-state metamorphism

The metamorphic record of an orogen reflects not only the thermal structure of the orogen, but also the interaction between the thermal structure and the particle paths of rocks moving through the system. To illustrate this point, we examine the metamorphic signature of three examples with similar thermal structures but different particle paths. For each case, collision has occurred for a sufficient time such that the metamorphic record of rocks exposed at the surface is time-invariant.

We focus on combinations of parameters that produce thermal structures compatible with the high-temperature, low-pressure conditions ($>500^\circ\text{C}$ at ~ 20 km) common to many collisional orogens. Case A has a deep and narrow heat-producing wedge with moderate heat production, case B has a moderately deep and wide wedge with relatively high heat production, and case C has a shallow and wide wedge with very high heat production (Table 2). For each case, convergence rate, subduction angle, and the thickness of the layer of heat-producing upper crust are the same. Thermal structures for the three cases are similar; temperatures exhibit a local maximum in the upper plate of $\sim 650^\circ\text{C}$ at ~ 300 km from the toe of the orogen and ~ 25 km deep, closed 600°C isotherms, and inverted geotherms within the upper plate (Fig. 4, Table 3).

Particle paths show the impact of changing the relative rates of accretion and erosion. Examples with higher ratios of v_c/a have steeper particle trajectories in the down-going plate and deeper heat-producing wedges, while examples with higher ratios of a/e have shallower particle trajectories in the hanging wall and wider heat-producing wedges. Although the thermal structures are generally similar, differences in particle paths result in different temperature-depth histories for individual rocks and distinct metamorphic temperature arrays observed at the surface.

For all cases, the metamorphic temperatures, pressures, and ages increase with distance from the toe of the orogen until metamorphic temperatures reach a local maximum in the metamorphic core of the orogen, and T_{max} decreases with distance immediately beyond the core. The distance from the toe of the orogen to the metamorphic core varies from 300 km (Case A) to 440 km (Case C) (Fig. 4, Table 3). Although peak metamorphic temperatures are similar for the three cases (reflecting the similar maximum temperatures within the upper plate), metamorphic depths and ages in the core vary somewhat ($z_m=30$ -38 km and $t_m=32$ -38 ma) and the PT histories are different. Rocks were buried to a

maximum depth of 57 km in Case A , while rocks were buried to a maximum depth of 42 km in Case C (Fig. 5, Table 3).

Portions of the piezothermic arrays closely approximate portions of crustal geotherms within the orogen (Fig. 5). Shallow portions of piezotherms ($0 \text{ km} < z_m < 15 \text{ km}$) mimic geotherms from near the foreland, and deep portions of the piezotherm ($z_m > \sim 25\text{-}35 \text{ km}$) are steep-to-inverted and mimic geotherms from the high-temperature region of the upper plate. Pressure-depth profiles of the inverted portion of the piezotherms for Cases A and B are not consistent with a lithostatic pressure difference ($\Delta z_{struct} \gg \Delta z_m$). For Case C, however, the inverted portion of the piezotherm has a near-lithostatic pressure-depth profile ($\Delta z_m = \Delta z_{struct}$).

These metamorphic records are similar to commonly observed metamorphic patterns in real orogens: metamorphic temperatures, depths, and ages increase with distance from the toe of the orogen; PT paths are counter-clockwise; rocks are heated during burial and reach their maximum temperature either at the end of burial or during early stages of unroofing; and inverted piezotherms develop, similar to those observed in places like the Himalaya (Le Fort, 1975; Hubbard, 1989). To better understand the relationship between metamorphism and the processes acting within an orogen, we investigate how varying specific tectonic processes affects regional metamorphic patterns and the PT and Tt paths of rocks within the metamorphic core.

Since accretion and erosion rates control the paths of rocks advected through an orogen and exert primary control on the thermal structure of the orogen by controlling the geometry of the heat-producing wedge, it is impossible to isolate the impact of varying accretion or erosion rates alone. Instead, we examine the impact of varying a and e together. First we modify the surface width of the heat-producing wedge while holding the maximum depth constant. Then we modify the maximum depth of the heat-producing wedge while holding the surface width constant. In the following examples, we use Case A as a basis of comparison and vary only a and e , keeping all other input parameters constant (Table 2).

Broadening the surface width of the heat-producing wedge does not change the magnitude of maximum temperatures within the orogen, but increases the distance from the toe of the orogen to the locus of maximum temperatures and broadens the region enclosed by the 600°C isotherm (Fig. 6, Table 4). The distance from the toe of the orogen to the metamorphic core also depends on the width of the heat-producing wedge, so that doubling the width of the heat-producing wedge almost doubles the distance to the metamorphic core. Peak metamorphic temperatures within the core do not change as the width is varied, but the metamorphic age of rocks in the core increases with increasing wedge width, and

rocks from the metamorphic core cool much more slowly in orogens with wide wedges (Fig. 7 Table 4). Deep portions of each of the piezothermic arrays mimic crustal geotherms, but the depth sampled by the piezotherm decreases with increasing wedge width. In addition, pressure-depth profiles of orogens with very wide wedges approximate lithostatic gradients.

Because the thermal structure of an orogen is strongly dependent on the depth of the heat-producing wedge, decreasing the wedge depth from 60 km to 40 km decreases maximum temperatures within the wedge from $\sim 650^{\circ}\text{C}$ to $\sim 450^{\circ}\text{C}$ and decreases the magnitude of the geothermal inversion (Fig. 8, Tables 5). These changes in the thermal structure are reflected in the metamorphic record. Shallow wedges are associated with cooler metamorphic temperatures within the metamorphic core, and less of a decrease in temperature on the “back” side of the core, opposite the subduction boundary. Varying the depth of the wedge does not change the distance from the toe of the orogen to the location of peak metamorphic temperatures. PT and Tt paths from the metamorphic cores show that rocks from orogens with shallow wedges are not buried as deeply and cool more slowly than rocks from orogens with deep wedges (Fig. 9, Table 5). In all cases, deep portions of the piezothermic arrays mimic the steep-inverted portions of crustal geotherms. Pressure-depth profiles of orogens with shallow wedges approximate lithostatic gradients.

Variations in the foreland geotherm can also affect the metamorphic record of an orogen. Increasing A and/or d_r in the down-going plate (while holding s_w and d_w constant) increases temperatures within the orogen, and metamorphic temperatures increase accordingly. The location of the metamorphic core as well as metamorphic pressures and ages within the core remain relatively unaffected.

To understand the relationship between piezotherms and geotherms, we consider in detail the relationship between the thermal structure of the orogen and particle paths. Consider a column of rocks perpendicular to the subduction contact passing through the high-temperature region of Case C (Fig. 4), where isotherms are closed and thermal gradients are inverted (Fig. 10). As the column passes through this region, rocks higher in the column achieve T_{max} sooner than lower rocks, and arrays of T_{max} vs. z_m will not record the thermal gradient of any one crustal column. However, as long as the particle paths are not vertical, within some portion of the crustal column, shallower rocks will pass through the hottest region, while deeper rocks will pass below the hottest region. Thus the column will preserve an inverted metamorphic temperature gradient similar to the geotherms in this region. If particle paths are relatively horizontal ($a/(\tan\Theta^*e) > \sim 8$), the metamorphic depths of the column of rocks will record a nearly lithostatic gradient.

Only in model orogens that have closed isotherms can piezotherms look like geotherms, and only in the case of relatively horizontal particle paths will $\Delta z_m \sim \Delta z_{struct}$. These results may provide a resolution to the apparent contradiction between numerical experiments which indicate that piezotherms should bear little resemblance to any actual geotherm within an orogen (England & Richardson, 1977) and the piezotherms from the Himalaya that record steep-to-inverted temperature gradients and pressure gradients consistent with lithostatic gradients (Macfarlane, 1995; Hubbard, 1989; Hodges *et al.*, 1988).

Transient metamorphic evolution

The above analysis is based on orogens which have evolved for sufficient time that the metamorphic records are invariant in time. These general observations are also valid for orogens with evolving metamorphic records. For example, we track the metamorphic history of Case A (Fig. 3) as it evolves from the subduction regime to a fully-developed collisional orogen (Fig. 11, Table 2). Following initial collision, rocks from the down-going plate are cycled through the orogen and brought to the surface of the upper plate, and the surface width of accreted crust increases at a rate of ~ 5 km/my. By $t=40$ my, nearly 200 km of the upper-plate surface is accreted crust. Metamorphic temperatures for $x < 140$ km are within 95% of the steady-state metamorphic temperatures, and between 140 km $< x < 185$ km temperatures are within 78% of the steady-state metamorphic temperatures. At $t=80$ my, the thermal structure of the orogen has been at a steady state for ~ 10 my ($t_w=69$ m.y.), the surface width of accreted crust is nearly 400 km, and peak temperatures within the metamorphic core reach $\sim 575^\circ\text{C}$, or $\sim 90\%$ of invariant peak metamorphic temperatures. By $t=120$ my, temperatures within the core no longer change, and metamorphic temperatures across the orogen are invariant by $t=160$ my.

In general, the transient metamorphic record approximates the steady-state metamorphic record. Once crust has been cycled through the orogen and brought to the surface, metamorphic temperatures are within $\sim 70\%$ of invariant temperatures. In general, metamorphic temperatures near the foreland become invariant within a few tens of millions of years after initial collision, and temperatures in the region of the core become invariant after an elapsed time of roughly $1.5 \times t_w$.

Discrete accretion

In real orogenic belts, accretion rarely acts continuously and may occur episodically, transferring discrete slabs of the down-going plate to the upper plate. To investigate how

this may affect the metamorphic record, we modify our model such that convergence and erosion act continuously while accretion occurs episodically, at regular intervals. During each accretion cycle of duration t_a , the lower plate is subducted and erosion removes material from the upper plate. At the end of the cycle accretion instantaneously transfers a slab of the down-going plate of vertical thickness h to the upper plate, and a new cycle begins with subduction continuing along a new surface at the base of the accreted slab.

The thermal structures of orogens undergoing episodic accretion do not achieve steady-state. However, after an elapsed time roughly $1.5 \times t_w$, temperatures throughout the orogen will cycle systematically over a time period equal to the accretion cycle. We calculate the thermal structures and metamorphic evolution for a case of thin-slab accretion (6 km) and thick-slab accretion (18 km) that have achieved cyclic steady state and compare them to the results for Case A from above (Figs. 4 & 5, Table 2). (To construct orogens with equivalent time-averaged s_w and d_w the convergence velocity for cases of slab accretion has to be increased slightly, while the time-averaged accretion rate and the erosion rate are kept the same.)

In both cases of discrete slab accretion maximum upper-plate temperatures do not change noticeably during the accretion cycle, but the location of maximum upper-plate temperatures migrates towards the toe of the orogen between accretion events (Fig. 12). Maximum upper plate temperatures for slab accretion are somewhat cooler than for the continuous accretion case ($\sim 600^\circ\text{C}$ vs. $\sim 650^\circ\text{C}$), perhaps reflecting the additional cooling due to the higher convergence rate.

For ease of comparison, we determine field gradients immediately following accretion. At that time, the slab adjacent to the foreland has not been eroded, and T_{max} , z_m , and t_m observed at the surface are all zero. Each slab experiences the same metamorphic history as it is subducted, accreted, and unroofed by erosion, only the level of exposure varies from slab to slab. Slabs further from the foreland have been attached to the upper plate for a longer time and are more deeply eroded.

The field gradients of orogens undergoing slab accretion are generally similar to continuous accretion field gradients; T_{max} , z_m , and t_m all increase with distance from the toe of the orogen, and metamorphic temperatures reach a peak $T_{max} \sim 600^\circ\text{C}$ in the metamorphic core located at $x \sim 300\text{--}400$ km. However, in the cases of slab accretion there are distinct steps in the field gradients. In most cases, the steps are located at the contacts between slabs. However, far from the toe of the orogen, the steps may occur within a slab. Rocks exposed near the foreland achieve T_{max} at the time of accretion. Thus, for these slabs, t_m and z_m are constant across the slab, and steps in the field gradients at slab contacts reflect the different erosion levels.

To understand the morphology of the field gradients far from the toe of the orogen, we examine PT and Tt paths in and near the slab of the metamorphic core for the thick-slab case (Fig 13). Maximum temperatures for rocks in this region are achieved in the upper plate, sometime after accretion, and z_m and t_m vary across the region. Rocks located at the left-hand edge of the core-slab ($x=270$ km) show a complex PT history: temperatures increase for a short period during unroofing, decrease as cold crust is subducted below, increase again after the underlying slab is accreted, and then decrease again until they reach the surface. For these rocks maximum temperatures are achieved at shallow levels, after accretion of the underlying slab. Meanwhile, temperatures for rocks on the right-hand edge of the core-slab ($x= 350$ km) are not as strongly affected by the subduction and accretion of the underlying slab, and maximum temperatures are achieved during early stages of unroofing, prior to accretion of the underlying slab. Thus, maximum temperatures for rocks within the slab are achieved at different times and depths, and t_m and z_m step within the slab. The PT history of rocks immediately to the left of the core-slab ($x=260$ km) show a simple cooling history, reaching maximum temperatures during early stages of unroofing, at the same time and depth as rocks in the overlying core-slab, and the field gradients are continuous across the contacts. Thus, model results imply that episodic accretion can result in continuous field gradients across structural discontinuities, and metamorphic discontinuities where there is no structural break. Is their field evidence to corroborate this conclusion? Relict fault contacts without metamorphic breaks are not uncommon in real orogens. However, step-like increases of metamorphic pressure equivalent to ~15 km within structurally coherent transects have not been reported. Since only metamorphic pressures change dramatically at the predicted metamorphic break, it is conceivable that there would be no change in mineral assemblages (as most mineral reactions are relatively insensitive to pressure changes at these conditions; Spear & Cheney, 1989), and such a metamorphic break would not be recognized in the field.

Discussion

The processes of accretion and erosion and the resulting accumulation of a wedge of heat-producing crust in the upper plate exert primary control on the metamorphic evolution of collisional orogens. Two key features of the metamorphic pattern, peak metamorphic temperatures and the distance from the toe of the orogen to the metamorphic core, are strongly dependent on the wedge geometry. High peak metamorphic temperatures are associated with deep wedges, while orogens with metamorphic cores located at a large distance from the toe of the orogen are associated with wide wedges. In turn, the dimensions of the wedge are directly controlled by the relative rates of accretion (a),

erosion (e) and plate convergence (v_c) such that high values of v_c/a result in deep wedges, and high values of a/e result in wide wedges (Eqns 2 & 3). Thus, we may be able apply these simple relationships and use petrologic data to constrain the rates of orogenic processes.

As an example, we use petrologic data from the Himalaya to constrain the depth and width of the heat-producing wedge and to estimate rates of accretion and erosion. These results can then be compared to independently constrained estimates of accretion and erosion rates. Within the Himalaya, peak metamorphic temperatures are on the order of 600-700°C at depths of ~20-30 km (Hubbard, 1989, Macfarlane, 1995), while measured heat production rates range from ~1.5 to >6 $\mu\text{W}/\text{m}^3$, with an average reported value of 2.6 $\mu\text{W}/\text{m}^3$ (Scharer, 1984; Scharer *et al.*, 1986; France Lanord & Le Fort, 1988; Cuney, *et al.*, 1984; Vidal *et al.*, 1982; Macfarlane, 1992). Average surface heat flow of the northern Indian continent is ~70 mW/m^2 (Rao *et al.*, 1976), corresponding to $d_r=18$ km for $A=2.6$ $\mu\text{W}/\text{m}^3$. From this, we estimate wedge depths for the Himalaya of $d_w=52 \pm 12$ km (Fig. 14). The maximum distance from the metamorphic core to the toe of the Himalayan orogen provides a minimum value of $s_w \sim 150$ km. Using these estimates of maximum depth and surface width of the heat-producing wedge, current convergence rates across the Himalaya (15-20 mm/yr .; Lyon-Caen & Molnar, 1985, Bilham *et al.*, 1997) and slab dip (7° - 15° ; Makovsky *et al.*, 1996; Lyon-Caen & Molnar, 1985), and equations 2 and 3, we estimate rates of accretion and erosion of $a=1.4 \pm 1.0$ km/my and $e=1.8 \pm 0.7$ km/my .

How do these rates compare to estimates of Himalayan accretion and erosion rates based on other evidence? During the past ~50 my slabs of the Indian plate have been accreted to the Eurasian plate (Gansser, 1964). The total width of material accreted over the 50 my extends 300 km from the suture zone to the active Himalayan front, giving an estimated accretion rate of 1.2 ± 0.5 km/my for $\Theta \sim 11 \pm 4^\circ$. Erosion within the Higher Himalaya has carved some of the deepest gorges in the world, and has been responsible for supplying sediment to the largest delta, the Bengal fan. Estimates for long-term erosion rates in the central Himalaya range from 0.5 to >5 km/my , (Hubbard *et al.*, 1991; Corrigan & Crowley, 1989; Copeland & Harrison, 1990).

The rates of erosion and accretion estimated from the distribution of metamorphism within the Himalaya are thus consistent with independent estimates of erosion and accretion rates. These results suggest that metamorphism may be strongly linked to the deformational history of orogenic belts via erosion and accretion, and that it may be feasible to invert metamorphic data to obtain information about the deformational history of orogenic systems.

References

- Bilham, R., Larson, K., Freymueller, J., Ranabhat, R., Sapkota, S.N., Shrestha, P.L., Thakuri, M.C., Timilsina, U.R., Tiwari, D.R., Vidal, G., Vigny, C., Galy, A. & de-Voogd, B., 1997. GPS measurements of present-day convergence across the Nepal Himalaya. *Nature*, **386**, 61-64.
- Copeland, P. & Harrison, T.M., 1990. Episodic rapid uplift in the Himalaya revealed by $^{40}\text{Ar}/^{39}\text{Ar}$ analysis of detrital K-feldspar and muscovite, Bengal fan. *Geology*, **10**, 354-357.
- Copeland, P., Parrish, R. & Harrison, T.M., 1988. Identification of inherited radiogenic Pb in monazite and its implications for U-Pb systematics. *Nature*, **333**, 760-763.
- Corrigan, J.D. & Crowley, K.D., 1989. Thermal history of sites 717 and 718, ODP Leg 116, central Indian Ocean; constraints from numerical simulations and apatite fission-track data. *Abstracts with Programs - Geological Society of America*, **21**, 320.
- Cuney, M., Le Fort, P. & Zhixiang, W., 1984. Uranium and thorium geochemistry and mineralogy in the Manaslu Leucogranite (Nepal, Himalaya). In: *Geology of granites and their metallogenic relations; proceedings of the international symposium* (eds Xu, K. & Tu, G.), pp. 853-873. Scientific Press, Beijing.
- Dahlen, F.A. & Barr, T.D., 1989. Brittle frictional mountain building; 1, Deformation and mechanical energy budget. *Journal of Geophysical Research*, **B, 94**, 3906-3922.
- England P.C. & Richardson, S.W., 1977. The influence of erosion upon the mineral facies of rocks from different metamorphic environments. *Journal of the Geological Society of London*, **134**, 201-213.
- Essene, E.J., 1989. The current status of thermobarometry in metamorphic rocks. In: *Evolution of metamorphic belts; proceedings of the 1987 joint meeting of the Metamorphic Studies Group and IGCP project 235*. (eds Daly, J.S., Cliff R.A. & Yardley, B.W.D.), pp. 1-44. Geological Society of London. London, United Kingdom.
- France Lanord, C. & Le Fort, P., 1988. Crustal melting and granite genesis during the Himalayan collision orogenesis. *Transactions of the Royal Society of Edinburgh: Earth Sciences*, **79**, 183-195.
- Gansser, A., 1964. *Geology of the Himalayas*, pp. 289. Wiley Interscience, New York.
- Ghent, E.D., Stout, M.Z., & Parrish, R.R., 1989. Determination of metamorphic pressure-temperature-time (PTt) paths. In: *Heat, Metamorphism and Tectonics* (eds Nisbet, E.B.G., & Fowler, C.M.R.), pp. 155-188. Mineralogical Association of Canada, Toronto.
- Heaman, L & Parrish, R., 1991. U-Pb geochronology of accessory minerals. In: *Applications of radiogenic isotope systems to problems in geology; short course handbook*. (eds Heaman, L. & Ludden, J.N.), pp. 59-102. Mineralogical Association of Canada, Toronto.
- Hodges, K.V., Hubbard, M. S. & Silverberg, D.S., 1988. Metamorphic constraints on the thermal evolution of the central Himalayan orogen. *Philosophical Transactions of the Royal Society of London*, **A326**, 257-280.
- Hodges, K.V., 1991. Pressure-temperature-time paths, *Annual Review of Earth and Planetary Sciences*, **19**, 207-236.

- Hodges, K.V. & McKenna, L.W. , 1987. Realistic propagation of uncertainties in geologic thermobarometry. *American Mineralogist*, **72**, 671-680.
- Hubbard, M.S. , 1989. Thermobarometric constraints on the thermal history of the Main Central Thrust Zone and Tibetan Slab, eastern Nepal Himalaya. *Journal of Metamorphic Geology*, **7**, 19-30.
- Hubbard, M., Royden, L. & Hodges, K. , 1991. Constraints on unroofing rates in the High Himalaya, eastern Nepal. *Tectonics*, **10**, 287-298.
- Huerta, A.D., Royden, L. & Hodges K., 1996. The Interdependence of Deformational and Thermal Processes in Mountain Belts. *Science*, **273**, 637-639.
- Huerta, A.D., L. Royden and K. Hodges, 1998. The thermal structure of collisional orogens as a response to accretion, erosion, and radiogenic heating. *Journal of Geophysical Research-B*, **103**, 15287-15302.
- Kohn-Matthew, J. & Spear, F.S., 1991(a). Error propagation for barometers; 1, Accuracy and precision of experimentally located end-member reactions. *American Mineralogist*, **76**, 128-137.
- Kohn-Matthew, J. & Spear, F.S., 1991(b). Error propagation for barometers; 2, Application to rocks. *American Mineralogist*, **76**, 138-147.
- Le Fort, P., 1975. Himalayas: The collided range. Present knowledge and of the continental arc. *American Journal of Science*, **275-A**, 1-44.
- Lyon-Caen, H. & Molnar, P., 1985. Gravity anomalies, flexure of the Indian plate, and the structure, support, and evolution of Himalaya and Ganga Basin. *Tectonics*, **4**, 513-538.
- Macfarlane, A.M., 1992. The Tectonic Evolution of the Core of the Himalaya, Langtang National Park, Central Nepal. *Ph.D. thesis, Massachusetts Institute of Technology, Cambridge*.
- Macfarlane, A.M., 1995. An evaluation of the inverted metamorphic gradient at Langtang National Park, Central Nepal Himalaya. *Journal of Metamorphic Geology*, **13**, 595-612.
- Makovsky, Y., Klempere, S.L., Huang, L. & Lu D., 1996. Structural elements of the southern Tethyan Himalaya crust from wide-angle seismic data. *Tectonics*, **15**, 997-1005.
- McDougal, I. & Harrison, T.M., 1988. Geochronology and Thermochronology by the $^{40}\text{Ar}/^{39}\text{Ar}$ Method, pp. 208. Oxford University Press, New York.
- Molnar, P. & England, P., 1990. Temperatures, Heat Flux, and Frictional Stress Near Major Thrust Faults, *Journal of Geophysical Research*, **95**, 4833-4856.
- Rao, R.U.M., Rao, B.V. & Narain, H., 1976. Radioactive heat generation and heat flow in the Indian Shield. *Earth and Planetary Science Letters*, **30**, 57-64.
- Richardson, S.W., & England, P.C., 1979. Metamorphic consequences of crustal eclogite production in overthrust orogenic zones. *Earth and Planetary Science Letters*, **42**, 183-190.
- Royden, L. & Hodges, K.V., 1984. A technique for analyzing the thermal and uplift histories of eroding orogenic belts; a Scandinavian example. *Journal of Geophysical Research*, **89**, 7091-7106.
- Royden, L.H., 1993. The Steady State Thermal Structure of Eroding Orogenic Belts and Accretionary Prisms. *Journal of Geophysical Research*, **98**, 4487-4507.

- Ruppel, C. & Hodges, K.V., 1994. Pressure-temperature-time paths from two-dimensional thermal models; prograde, retrograde, and inverted metamorphism. *Tectonics*, **13**, 17-44.
- Scharer, U., 1984. The effect of initial ^{230}Th disequilibrium on young U-Pb ages: the Makalu case, Himalaya. *Earth and Planetary Science Letters*, **67**, 191-204.
- Scharer, U., Xu, R. & Allegre, C., 1986. U-(Th)-Pb systematics and ages of Himalayan leucogranites, South Tibet. *Earth and Planetary Science Letters*, **77**, 35-48.
- Spear, F.S. & Cheney, J.T., 1989. A petrogenetic grid for pelitic schists in the system SiO_2 - Al_2O_3 - FeO - MgO - K_2O - H_2O . *Contributions to Mineralogy and Petrology*, **101**, 149-164.
- Spear, F.S. & Selverstone, J., 1983. Quantitative P-T paths from zoned minerals: theory and tectonic applications, *Contributions to Mineralogy and Petrology*, **83**, 348-357.
- Vidal, P., Cocherie, A. & Le Fort, P., 1982. Geochemical investigations of the origin of the Manaslu leucogranite (Himalaya, Nepal), *Geochimica Cosmochimica Acta*, **46**, 2279-2292.

Figures

- Fig. 1 Model geometry used to simulate the thermal evolution of collisional orogens. Material is accreted from the lower plate to the upper plate at rate a (measured vertically) and removed at the surface at rate e . During subduction, a wedge of heat producing crust forms within the upper plate and, at steady state, achieves a maximum depth d_w and a surface width s_w .
- Fig. 2 Particle paths in two frames of reference. Upper panel: no accretion or erosion, particle paths are identical in both frames of reference. Middle panel: frame of reference which is fixed with respect to the horizontal position of particles in the upper plate so that the subduction boundary moves laterally at rate $(a'-e')$, where $a'=a/\tan\Theta$, and $e'=e/\tan\Theta$. Lower panel: frame of reference fixed with respect to the toe of the upper plate so that the position of the subduction boundary remains fixed through time. v_u , velocity of upper plate with respect to frame of reference; v_l , velocity of lower plate with respect to frame of reference; v_c , velocity of lower plate with respect to upper plate.
- Fig. 3 Cross sections showing the distribution of heat-producing crust within the upper plate and the thermal evolution from $t=0$ (initiation of collision) to thermal steady state at $t=80$ my (accretion rate $a=1.2$ km/my, erosion rate $e=1.12$ km/my, and heat production rate $A=1.75$ $\mu\text{W}/\text{m}^3$, see Table 2 for other parameters). Contours are isotherms with contour interval of 200°C , stippled-pattern is area of heat producing crust, and heavy line shows the position of the subduction boundary
- Fig. 4 Steady-state thermal structures (top) and metamorphic field gradients (bottom) for three model orogens that produce maximum upper plate temperatures of about 600°C at depths of ~ 30 km (see Table 2 for parameters). Top panels: solid white line shows position of the subduction boundary, heavy black arrows show particle trajectories and outline region of heat-producing crust, and dashed white line shows positions where rocks achieve their maximum temperatures, T_{max} . Bottom panels: shaded region of field gradients shows general location of the "metamorphic core" where maximum metamorphic temperatures are present at the surface. For rocks that reach the surface at a distance x_{sur} from the toe of the orogen, T_{max} =maximum metamorphic temperature, z_m = depth at T_{max} , and t_m = time at T_{max} (relative to the time at which the rock reaches the surface).
- Fig. 5 Steady-state temperature-time (Tt) and pressure-temperature (PT) paths (top), steady-state thermal structures (middle), and steady-state piezothermic arrays and pressure-depth profiles (bottom) for three model orogens that produce maximum upper plate temperatures of about 600°C at depths of 30-50 km (see Table 2 for parameters). Top panels: PT and Tt paths for rocks that reach the surface at $x=240$ km, $x=540$ km, and for the rock that passes through the locus of maximum upper plate temperatures. Middle panel: solid white line shows position of subduction boundary, heavy black lines show particle paths for rocks that reach the surface at $x\sim 240$ km, $x\sim 540$ km, and for the rock that passes through the locus of maximum upper plate temperatures. Bottom left panel: bold line shows array of metamorphic temperatures versus metamorphic depth (T_{max} vs. z_m), thin lines display geotherms (T vs. z). Bottom right panel: bold line shows array of metamorphic depths versus upper plate structural position (z_m vs. z_{struct}), dashed line indicates lithostatic gradient ($\Delta z_m = \Delta z_{struct}$).
- Fig. 6 Steady-state thermal structures (top) and metamorphic field gradients (bottom) as a function of surface width of the heat-producing wedge (see Table 2 for parameters). Top panels: solid white line shows position of the subduction

boundary, heavy black arrows show particle trajectories and outline region of heat-producing crust, and dashed white line shows positions where rocks achieve their maximum temperatures, T_{max} . Bottom panels: shaded region of field gradients shows general location of the “metamorphic core” where maximum metamorphic temperatures are present at the surface. For rocks that reach the surface at a distance x_{sur} from the toe of the orogen, T_{max} =maximum metamorphic temperature, z_m = depth at T_{max} , and t_m = time at T_{max} (relative to the time at which the rock reaches the surface).

Fig. 7 Steady-state temperature-time (Tt) and pressure-temperature (PT) paths (top), steady-state thermal structures (middle), and steady-state piezothermic arrays and pressure-depth profiles (bottom) as a function of surface width of the heat-producing wedge (see Table 2 for parameters). Top panels: PT and Tt paths for the rock that passes through the locus of maximum upper plate temperatures. Middle panel: solid white line shows position of subduction boundary, heavy black lines show particle paths for the rock that passes through the locus of maximum upper plate temperatures. Bottom left panel: bold line shows array of metamorphic temperatures versus metamorphic depth (T_{max} vs. z_m), thin lines display geotherms (T vs. z). Bottom right panel: bold line shows array of metamorphic depths versus upper plate structural position (z_m vs. z_{struct}), dashed line indicates lithostatic gradient ($\Delta z_m = \Delta z_{struct}$).

Fig. 8 Steady-state thermal structures (top) and metamorphic field gradients (bottom) as a function of maximum depth of the heat-producing wedge (see Table 2 for parameters). Top panels: solid white line shows position of the subduction boundary, heavy black arrows show particle trajectories and outline region of heat-producing crust, and dashed white line shows positions where rocks achieve their maximum temperatures, T_{max} . Bottom panels: shaded region of field gradients shows general location of the “metamorphic core” where maximum metamorphic temperatures are present at the surface. For rocks that reach the surface at a distance x_{sur} from the toe of the orogen, T_{max} =maximum metamorphic temperature, z_m = depth at T_{max} , and t_m = time at T_{max} (relative to the time at which the rock reaches the surface).

Fig. 9 Steady-state temperature-time (Tt) and pressure-temperature (PT) paths (top), steady-state thermal structures (middle), and steady-state piezothermic arrays and pressure-depth profiles (bottom) as a function of maximum depth of the heat-producing wedge (see Table 2 for parameters). Top panels: PT and Tt paths for the rock that passes through the locus of maximum upper plate temperatures. Middle panel: solid white line shows position of subduction boundary, heavy black lines show particle paths for the rock that passes through the locus of maximum upper plate temperatures. Bottom left panel: bold line shows array of metamorphic temperatures versus metamorphic depth (T_{max} vs. z_m), thin lines display geotherms (T vs. z). Bottom right panel: bold line shows array of metamorphic depths versus upper plate structural position (z_m vs. z_{struct}), dashed line indicates lithostatic gradient ($\Delta z_m = \Delta z_{struct}$).

Fig. 10 Detail of steady-state thermal structure and particle paths for Case C (Fig. 4, see Table 2 for parameters) showing the passage of a column of rock through the hot region of the upper plate. Symbols represent rocks within the column, bold symbols indicate locations where rocks achieve T_{max} . Note preservation of inverted gradient in the metamorphic record

Fig. 11 Evolution of metamorphic field gradient for Case A (Fig. 4, see Table 2 for parameters). Thick lines show metamorphic conditions of rocks which have been

cycled through the orogen and have reached the surface, thin line shows steady-state metamorphic temperatures for comparison.

- Fig. 12 Thermal structures (top) and metamorphic field gradients (bottom) during steady state or cyclic steady state for orogens with the same average accretion rate (h/t_a) and erosion rate (e) as Case A (Fig. 4) as a function of thickness of the accreted slab (h) (see Table 2 for parameters). Top panels: solid white line shows position of the subduction boundary. Bottom panels: shaded region of field gradients shows general location of the “metamorphic core” where maximum metamorphic temperatures are present at the surface, dashed lines indicate surface location of relict subduction boundaries.
- Fig. 13 Metamorphic field gradient (bottom) and pressure-temperature (PT) and temperature-time (Tt) paths (top) for rocks near and within the metamorphic core for the case of thick-slab accretion ($h=18$ km) during cyclic steady state (see Table 2 for parameters). Top: dash-dot lines indicate accretion events, bold dots indicate conditions at T_{max} . Bottom: dashed lines indicate surface location of relict subduction boundaries.
- Fig. 14 Maximum upper plate temperatures as a function of heat production rate (A) and maximum depth of the heat producing wedge (d_w). (a) Maximum upper-plate temperatures at $z=20$ km, and (b) maximum upper-plate temperatures at $z=30$ km. (From Huerta *et al.*, 1998).

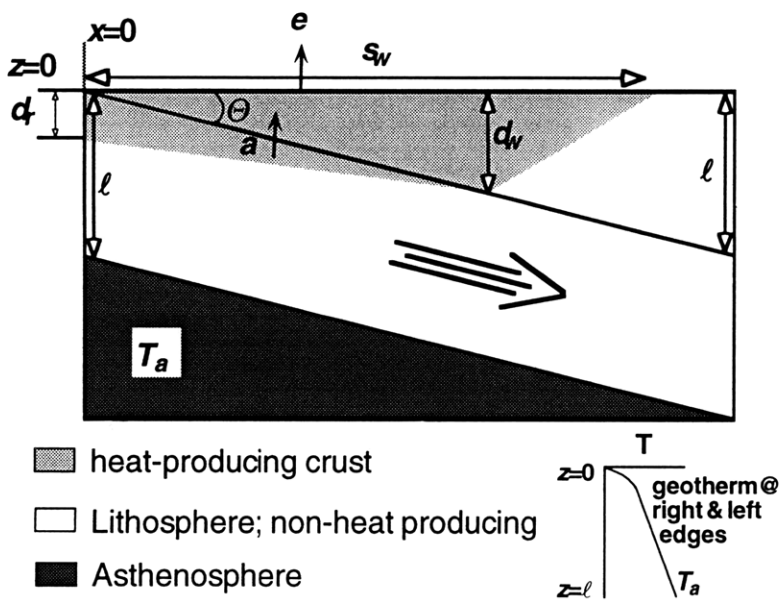


Figure 1

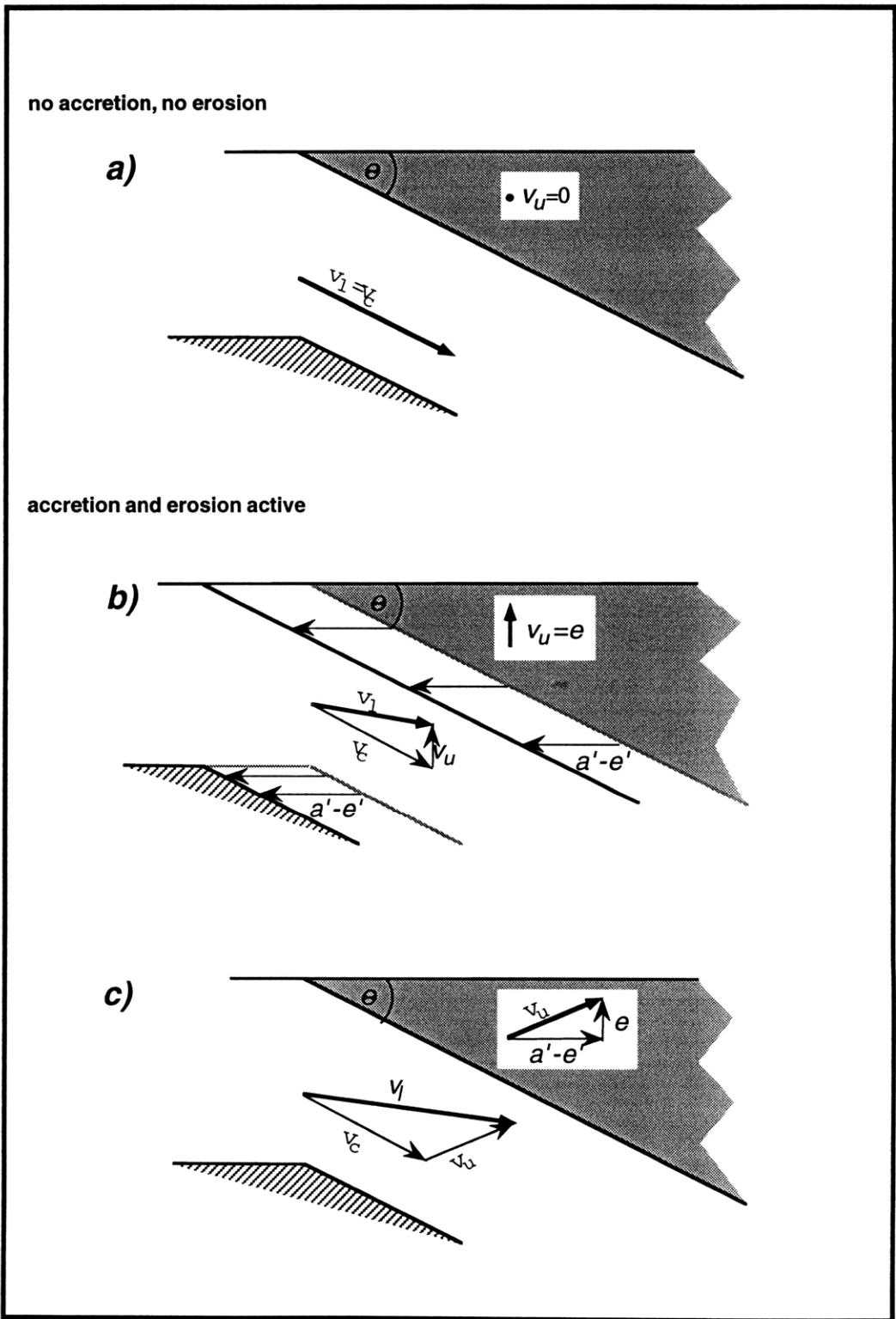


Figure 2

$a=1.2 \text{ km./my}$, $e=1.12 \text{ km/my}$, $A=1.75 \mu\text{W/m}^3$

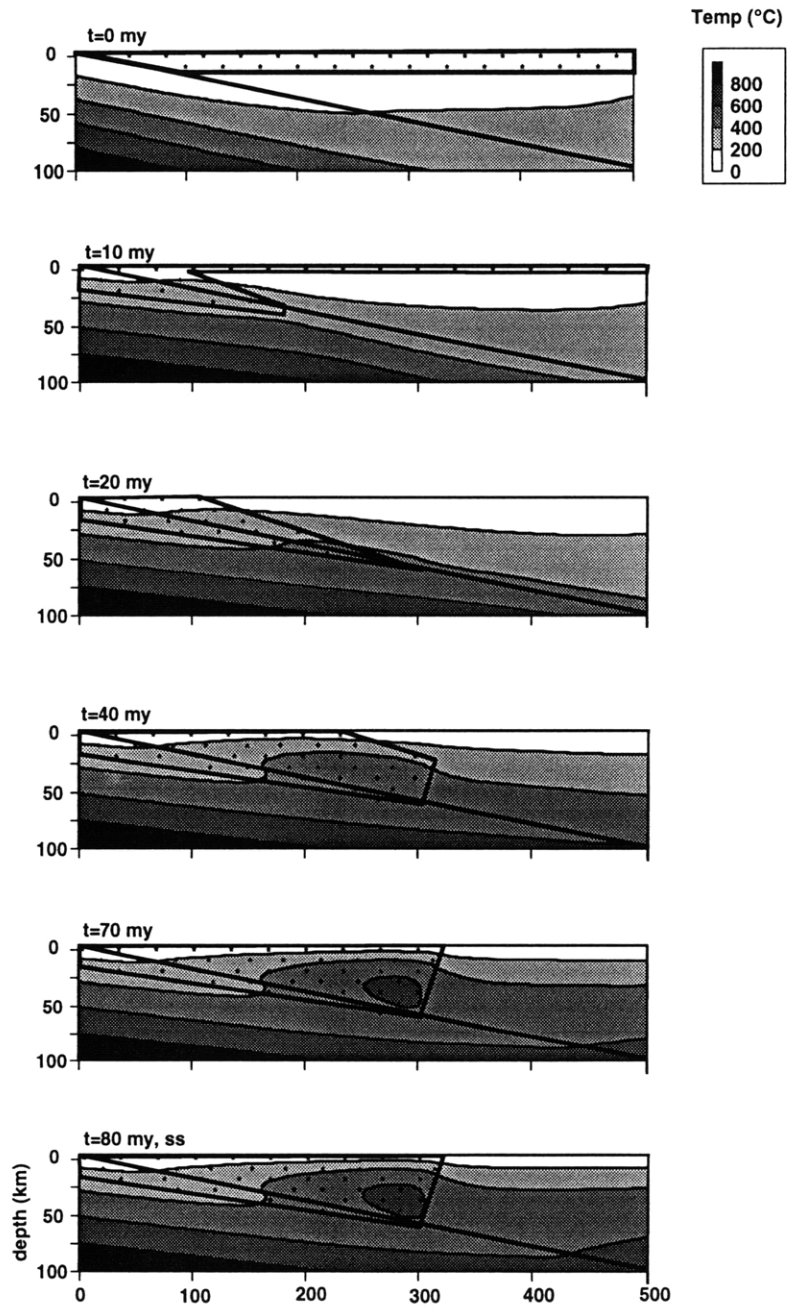


Figure 3

Case A: $a=1.2$ km./my, $e=1.12$ km/my, $A=1.75 \mu\text{W}/\text{m}^3$

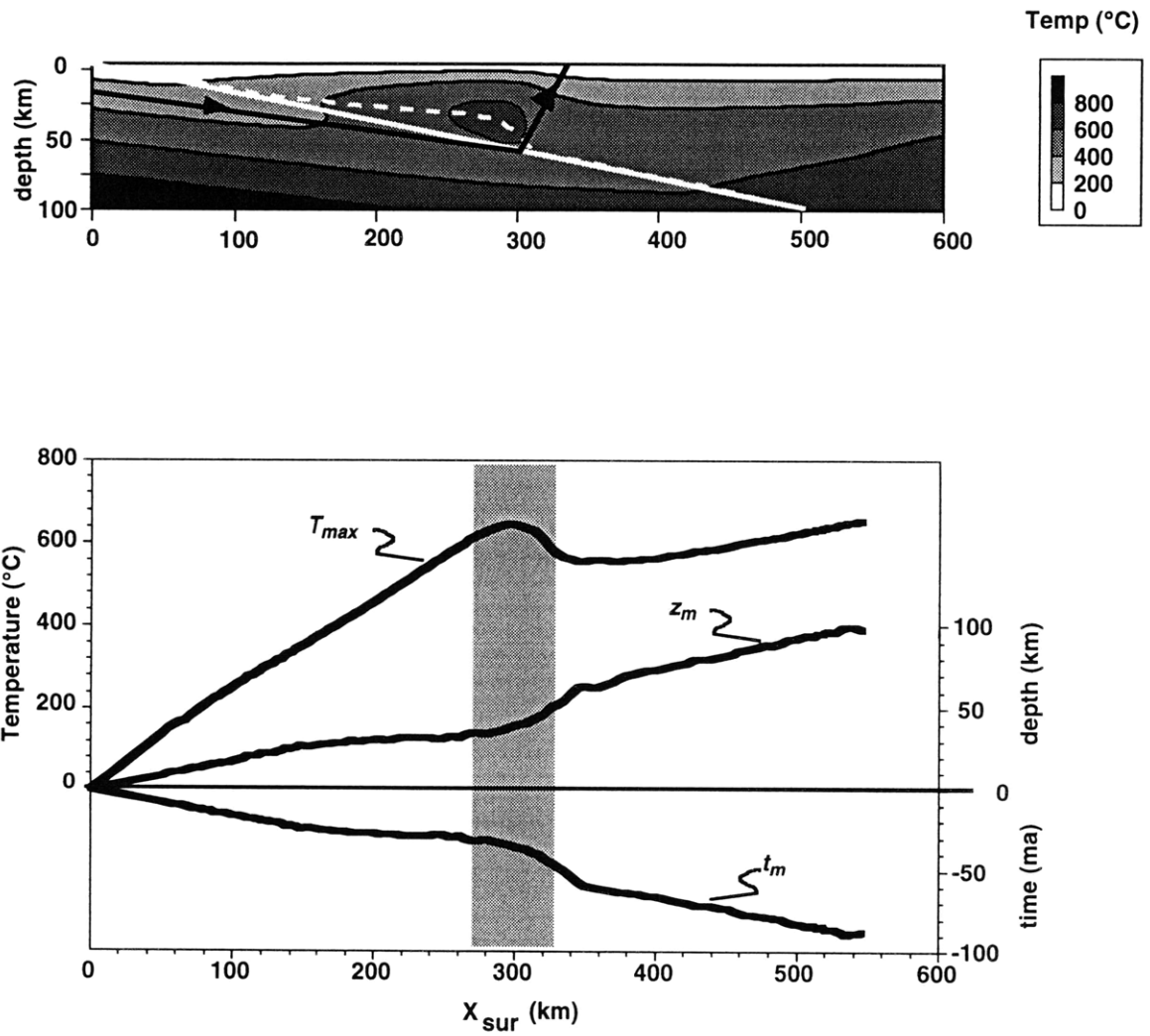


Figure 4

Case B: $a=1.46$ km./my, $e=1.0$ km/my, $A=2.0 \mu\text{W}/\text{m}^3$

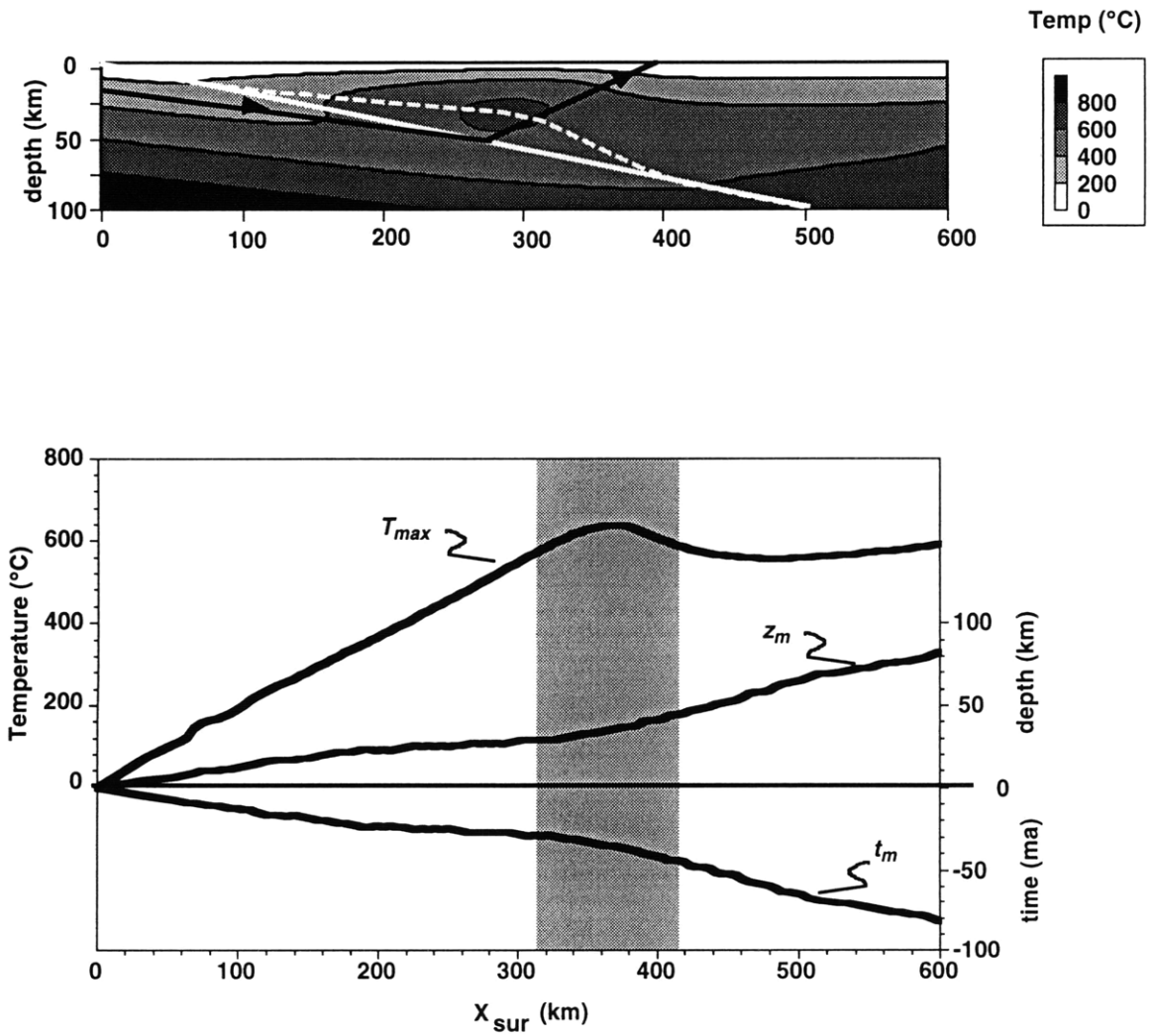


Figure 4, con't

Case C: $a=2.0$ km./my, $e=0.93$ km/my, $A=3.0 \mu\text{W}/\text{m}^3$

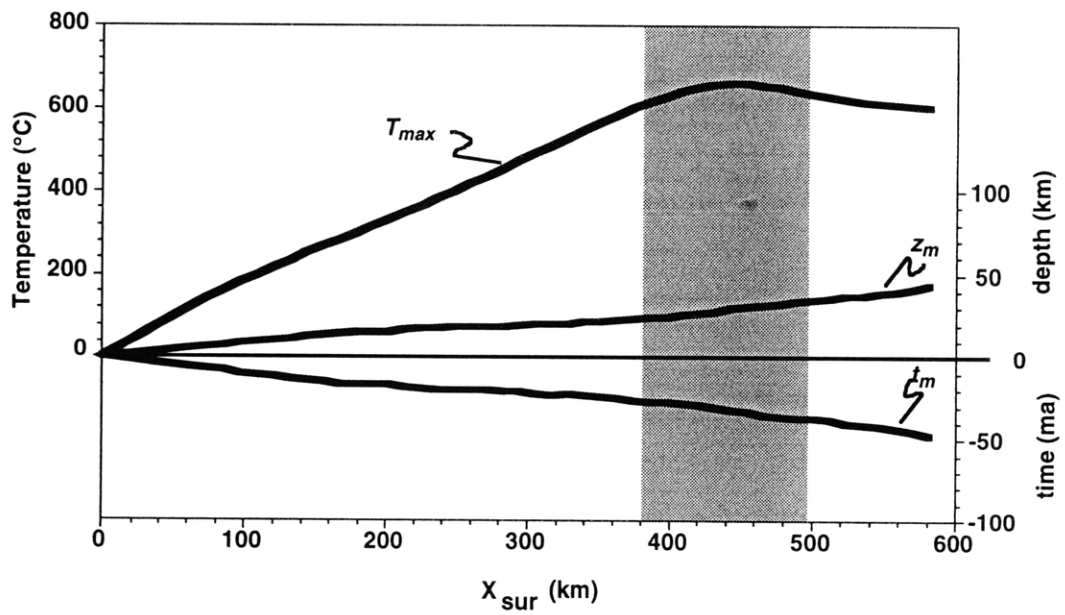
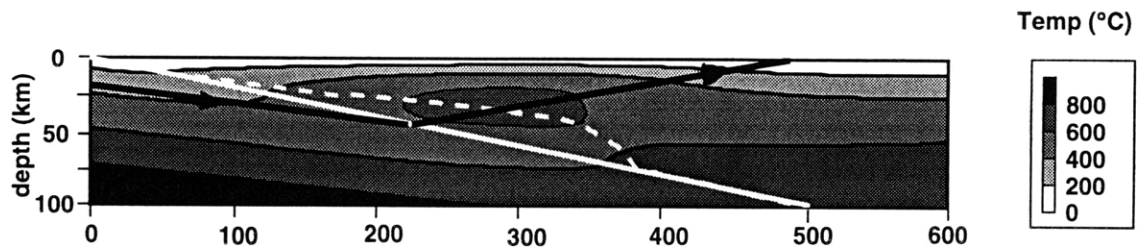


Figure 4

Case A: $a=1.2$ km/my, $e=1.12$ km/my, $A=1.75 \mu\text{W}/\text{m}^3$

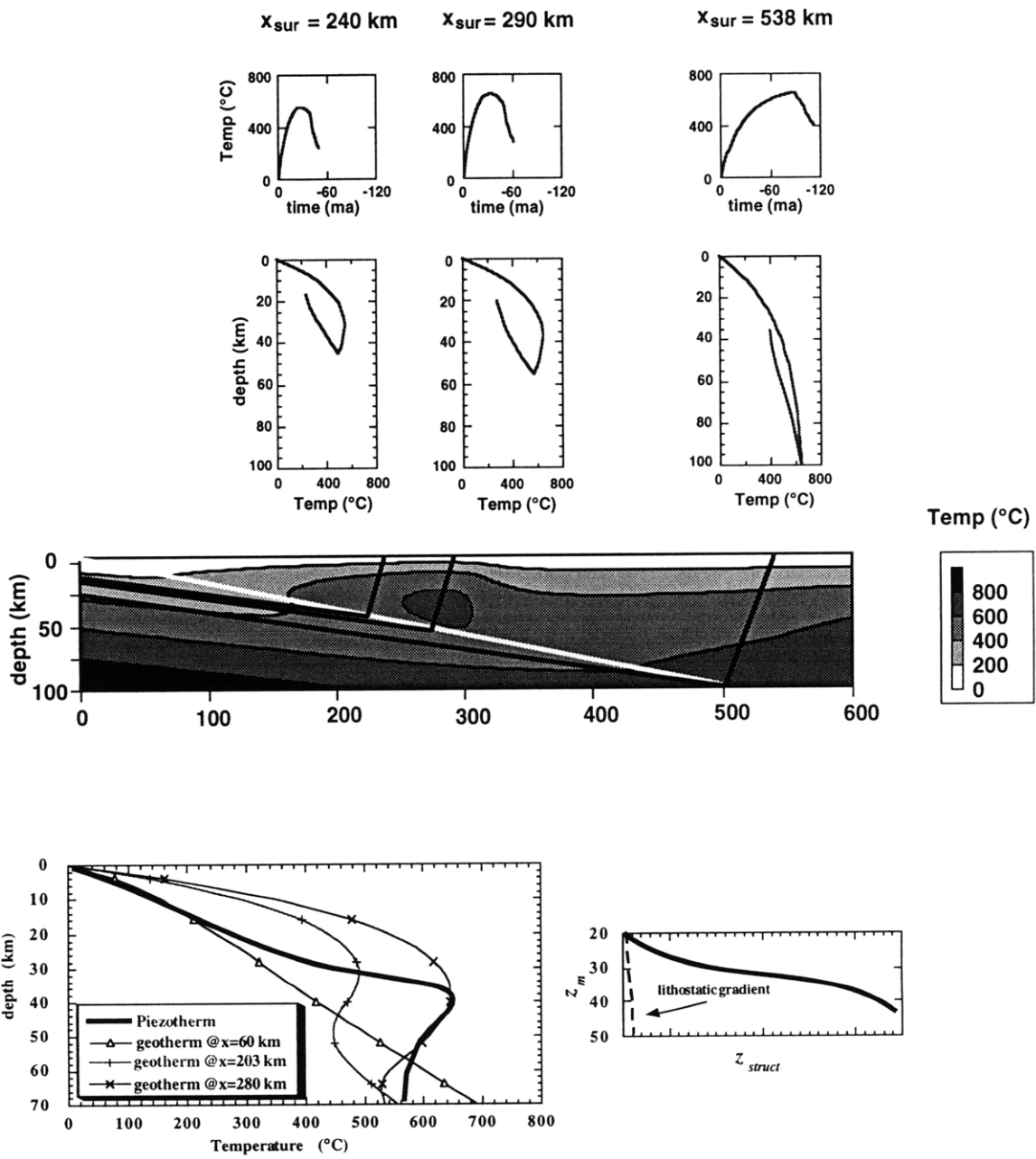


Figure 5

Case B: $a=1.46$ km/my, $e=1.0$ km/my, $A=2.0 \mu\text{W}/\text{m}^3$

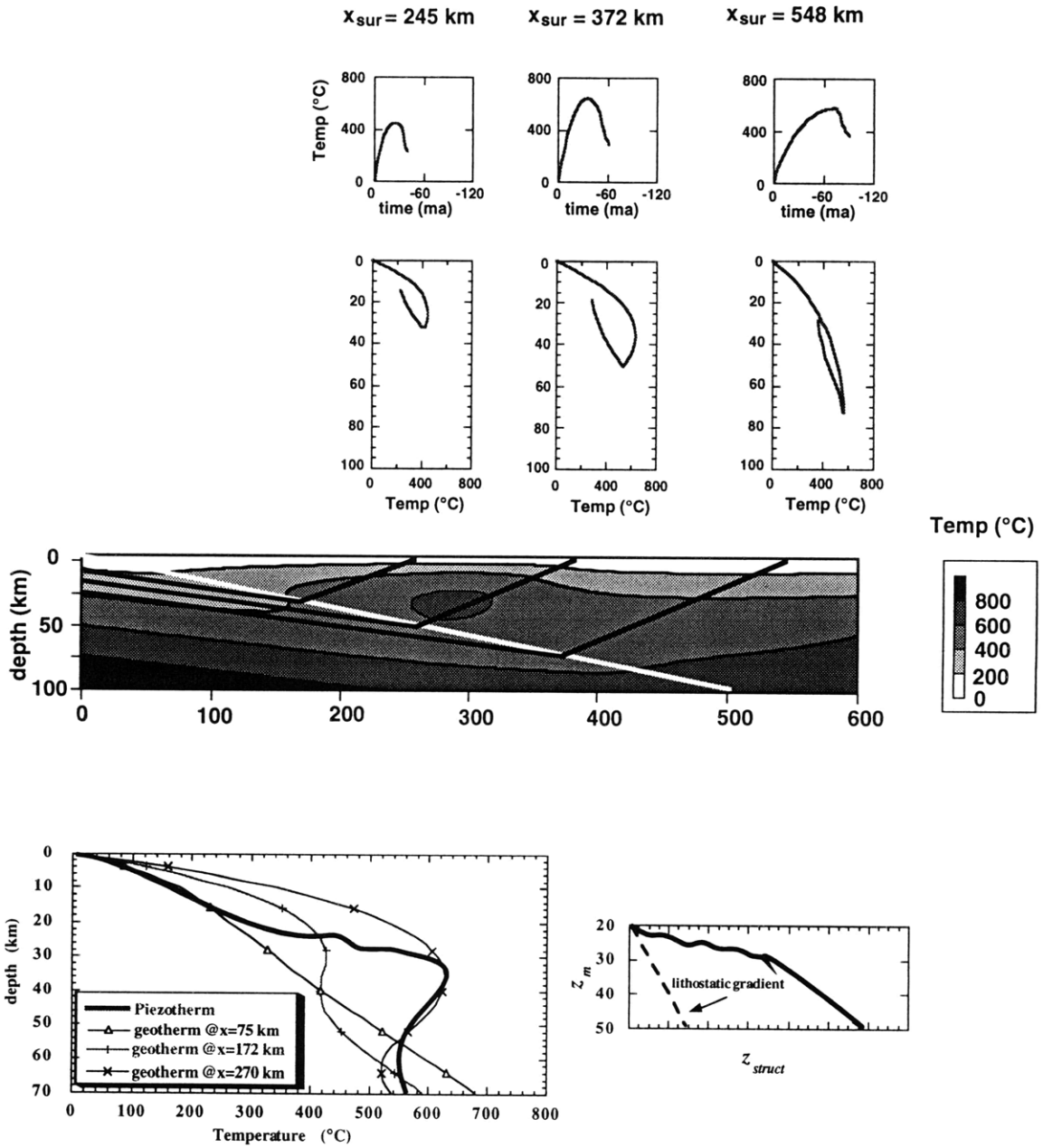


Figure 5, con't

Case C: $a=2.0$ km/my, $e=0.93$ km/my, $A=3.0 \mu\text{W/m}^3$

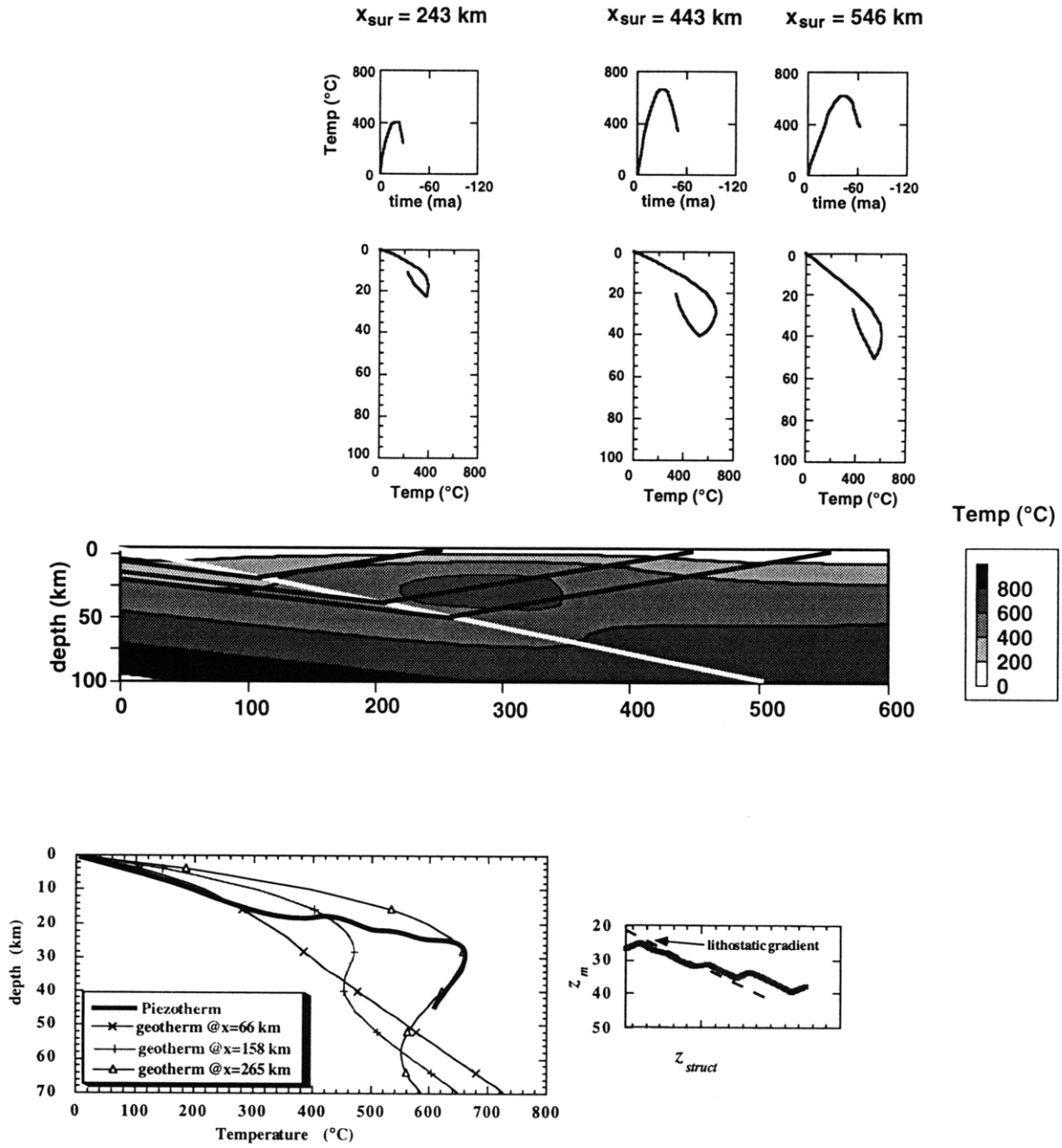


Figure 5, con't

$s_w=320$ km

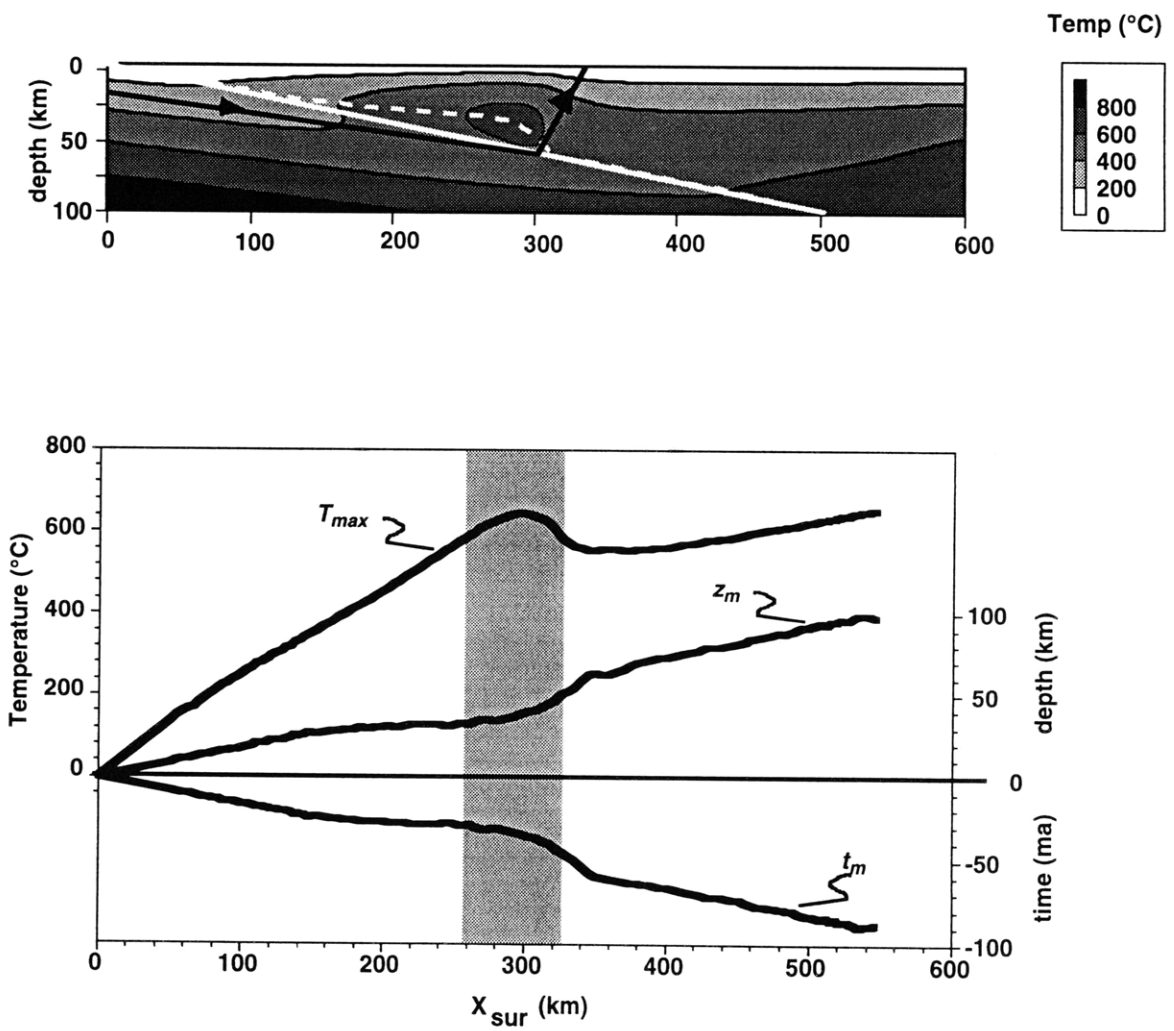


Figure 6

$s_w=480$ km

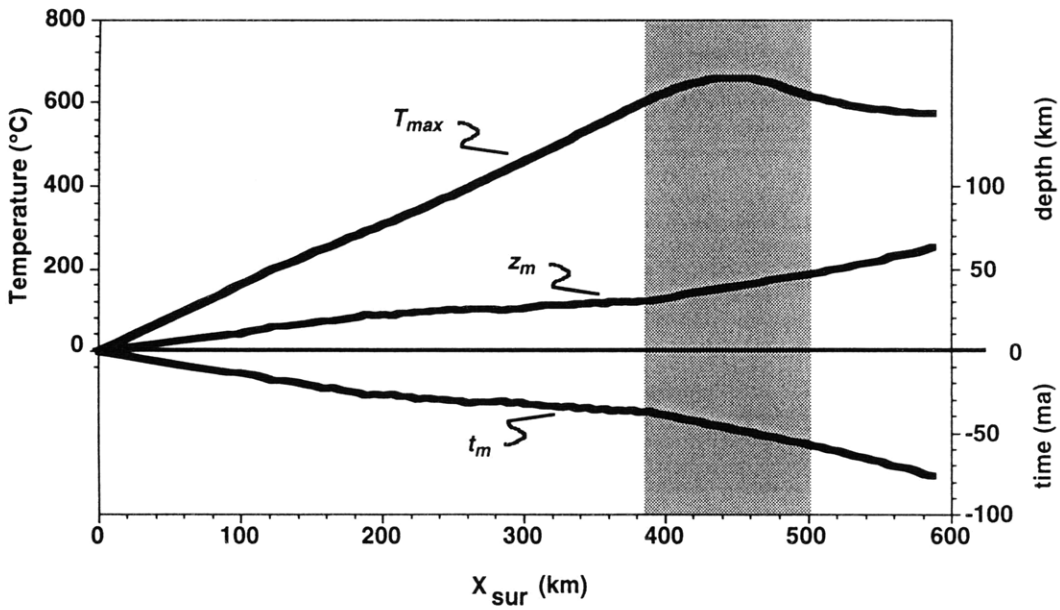
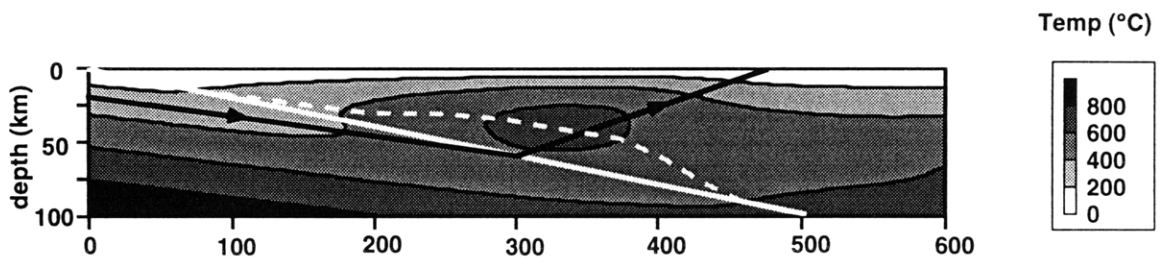


Figure 6, con't

$s_w=640$ km

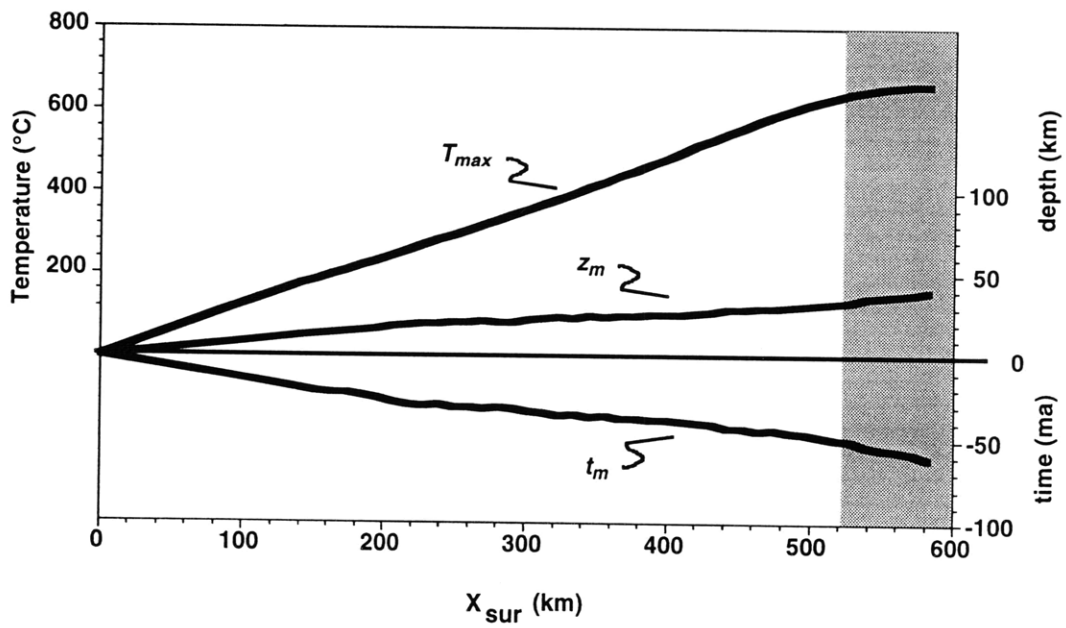
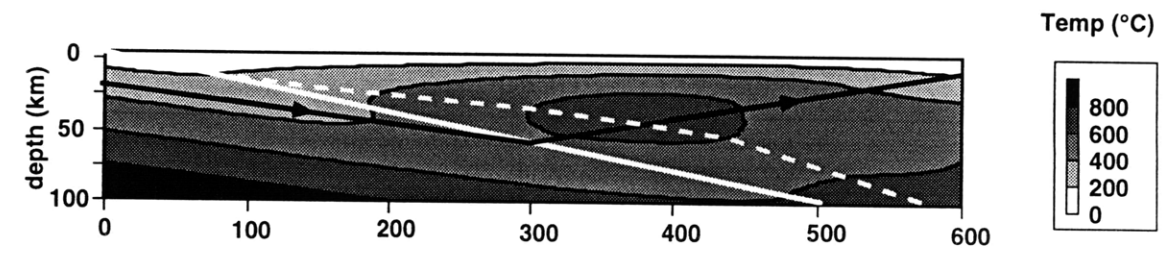


Figure 6, con't

$s_w = 320$ km

$x_{sur} = 290$ km

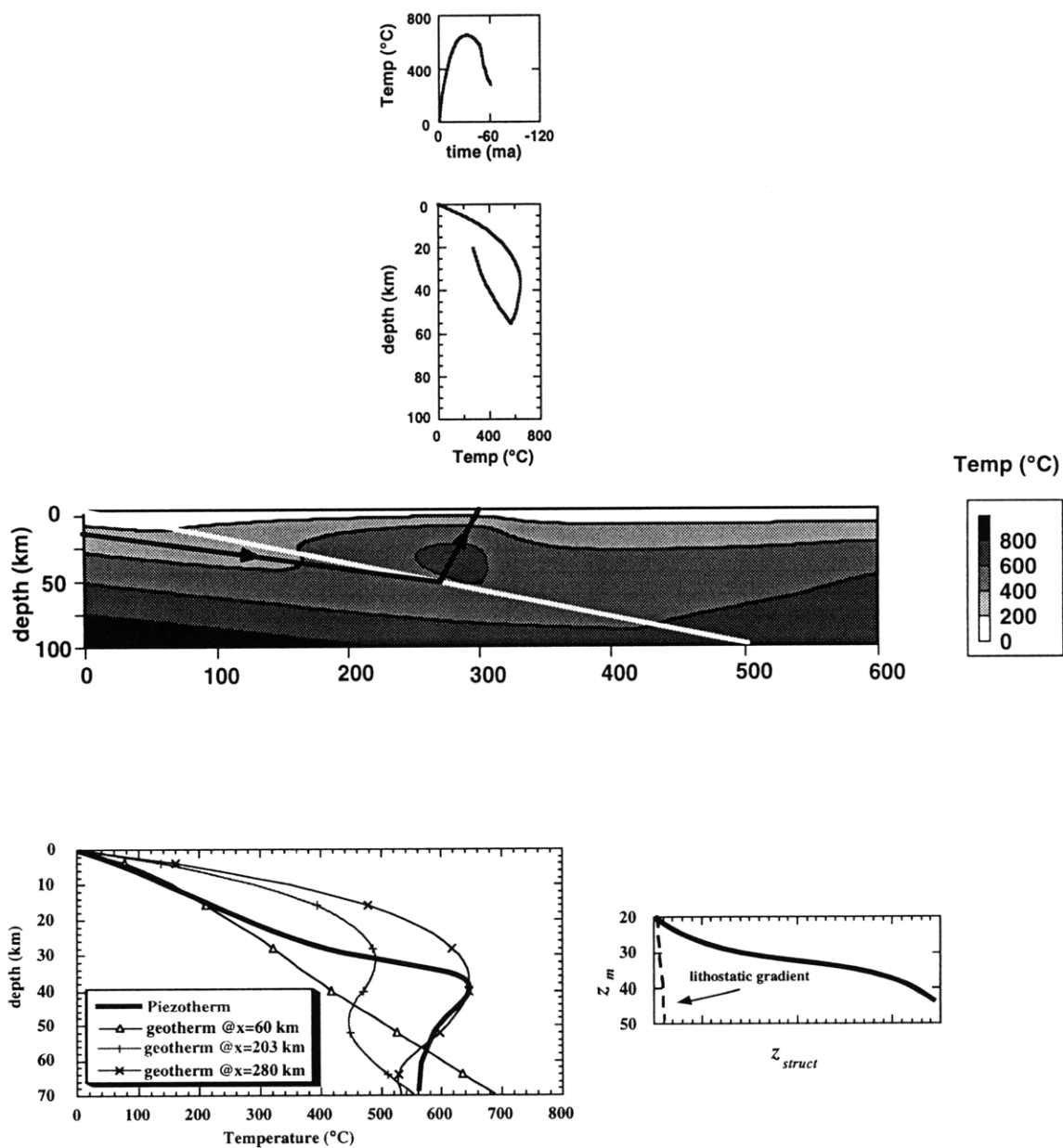


Figure 7

$s_w=480$ km

$x_{sur}=450$ km

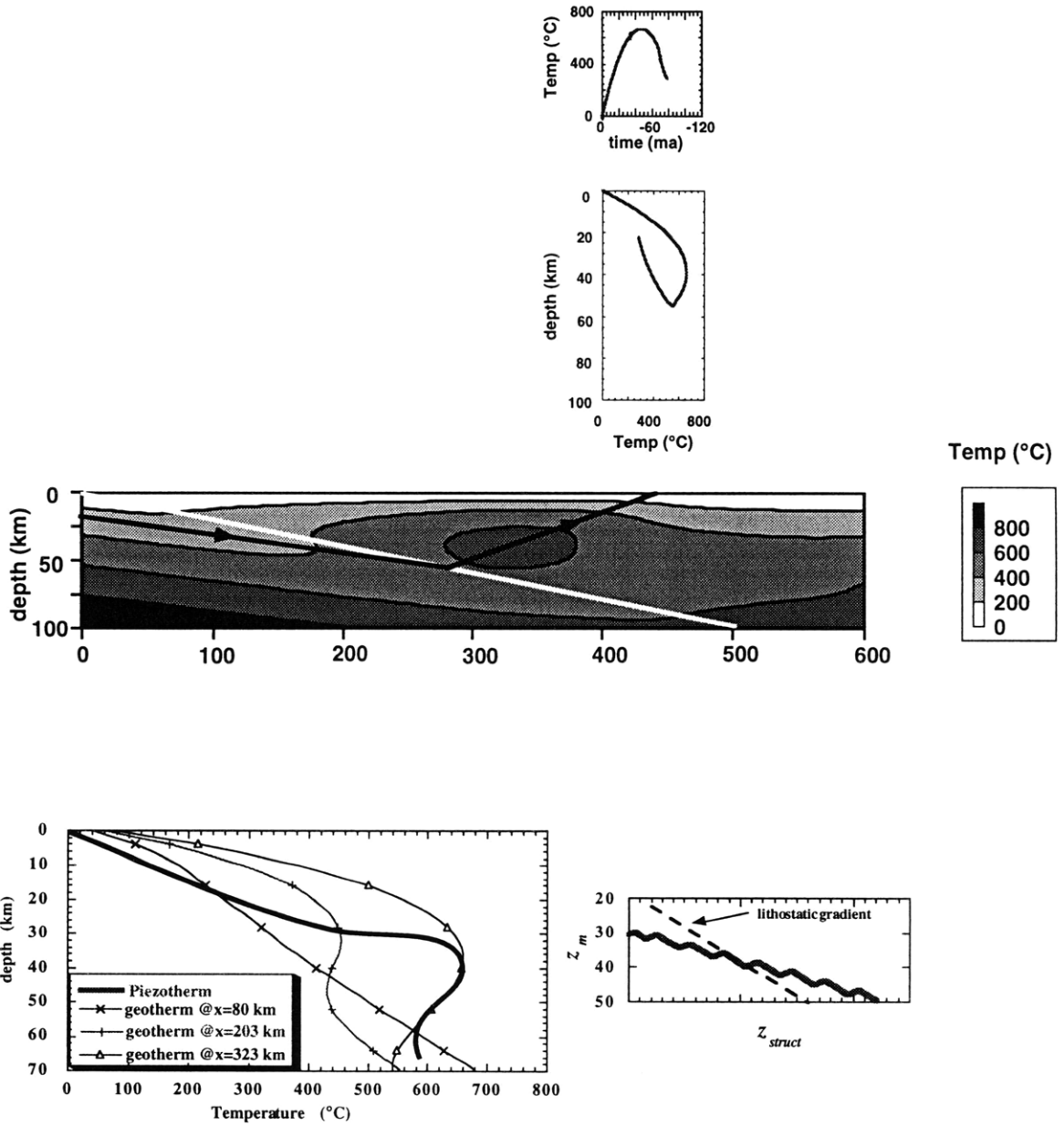


Figure 7, con't

$s_w=640$ km

$x_{sur}=585$ km

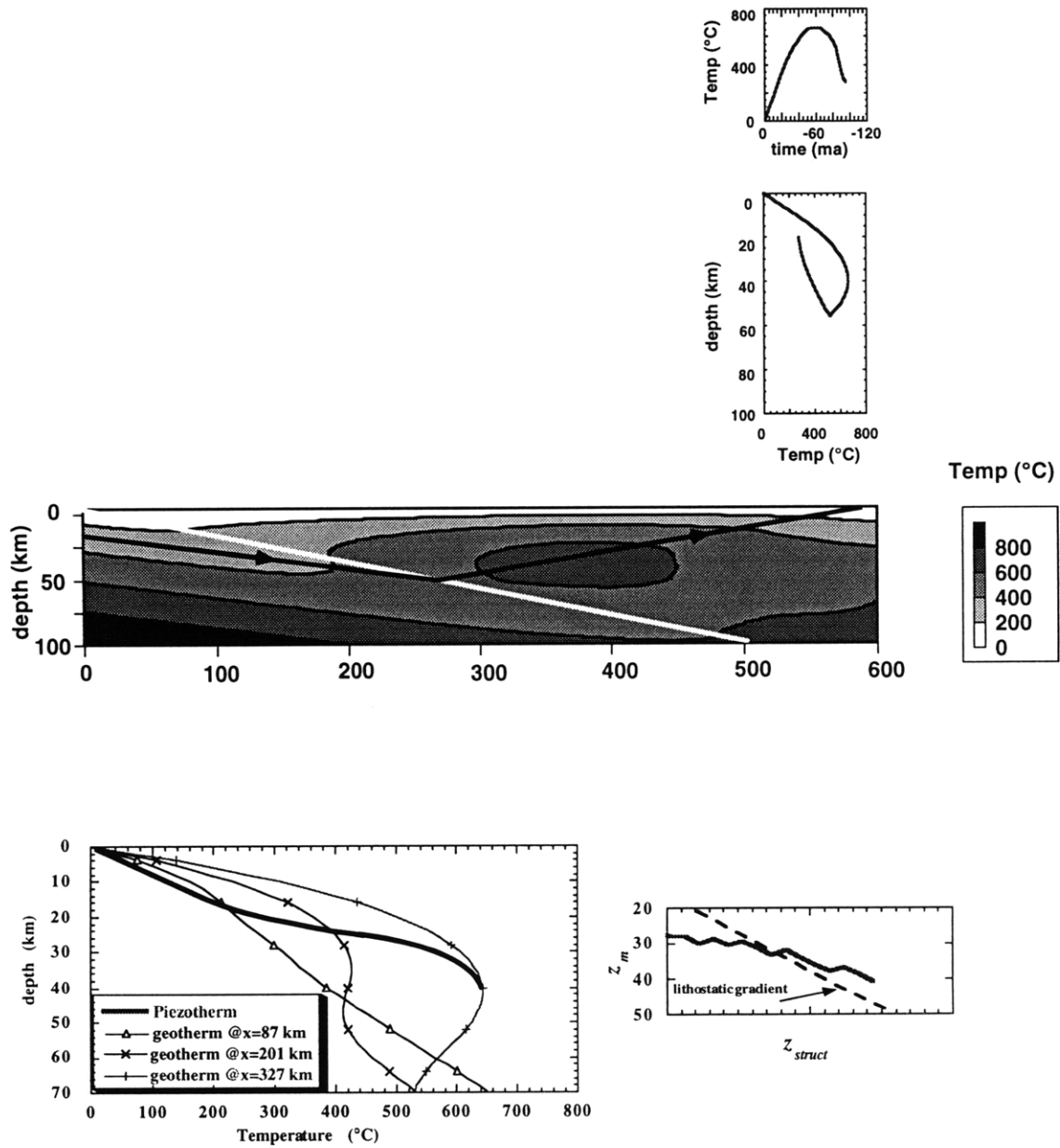


Figure 7, con't

$d_w=60$ km

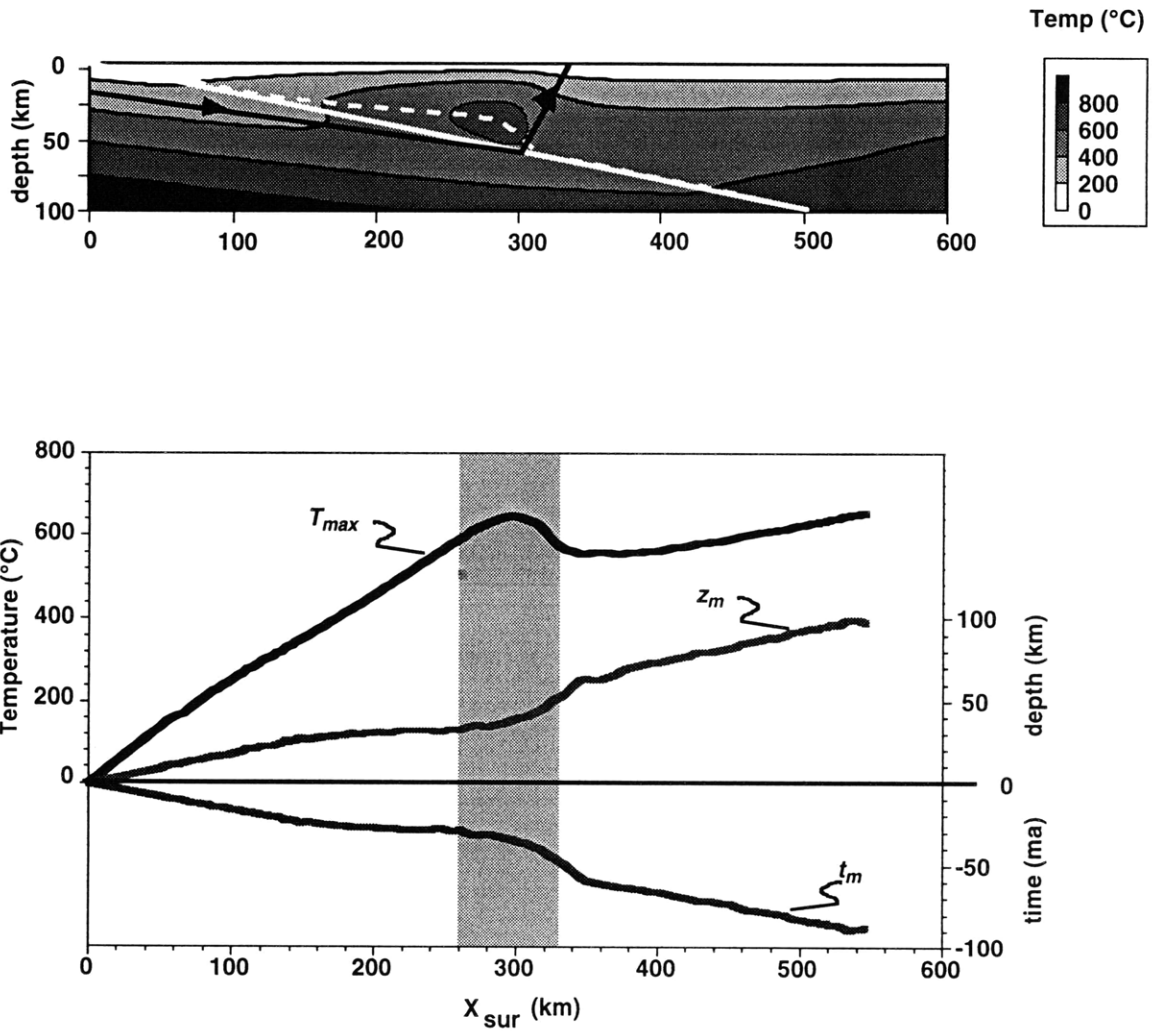


Figure 8

$d_w = 50$ km

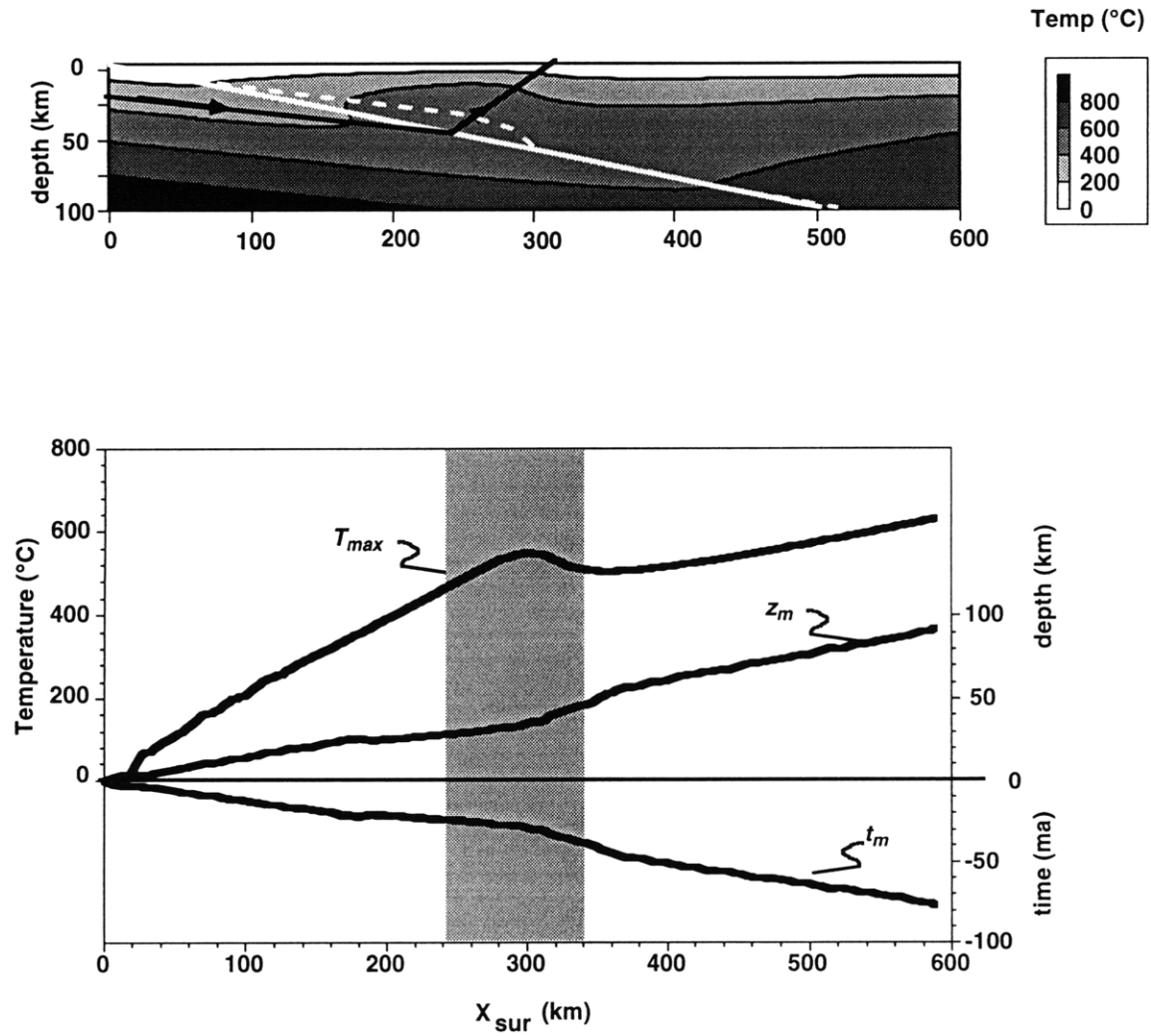


Figure 8, con't

$d_w=40$ km

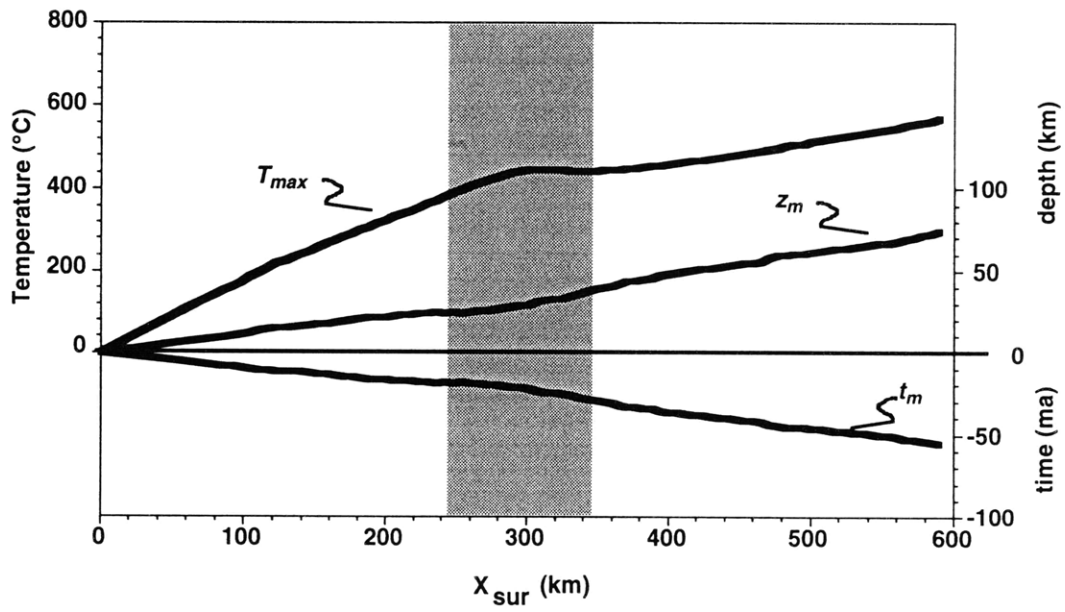
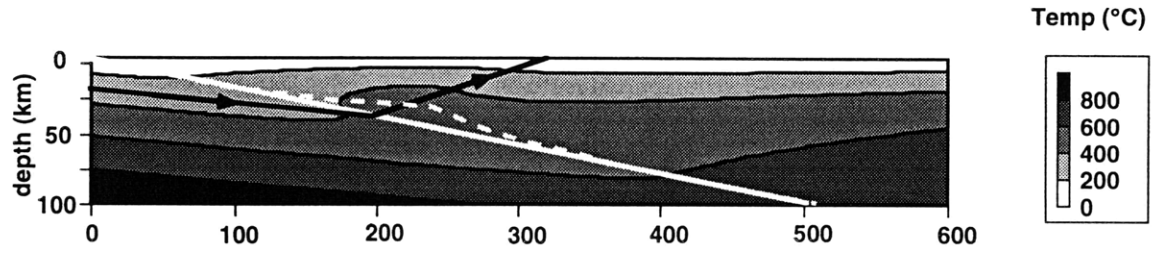


Figure 8, con't

$d_w = 60$ km

$x_{sur} = 290$ km

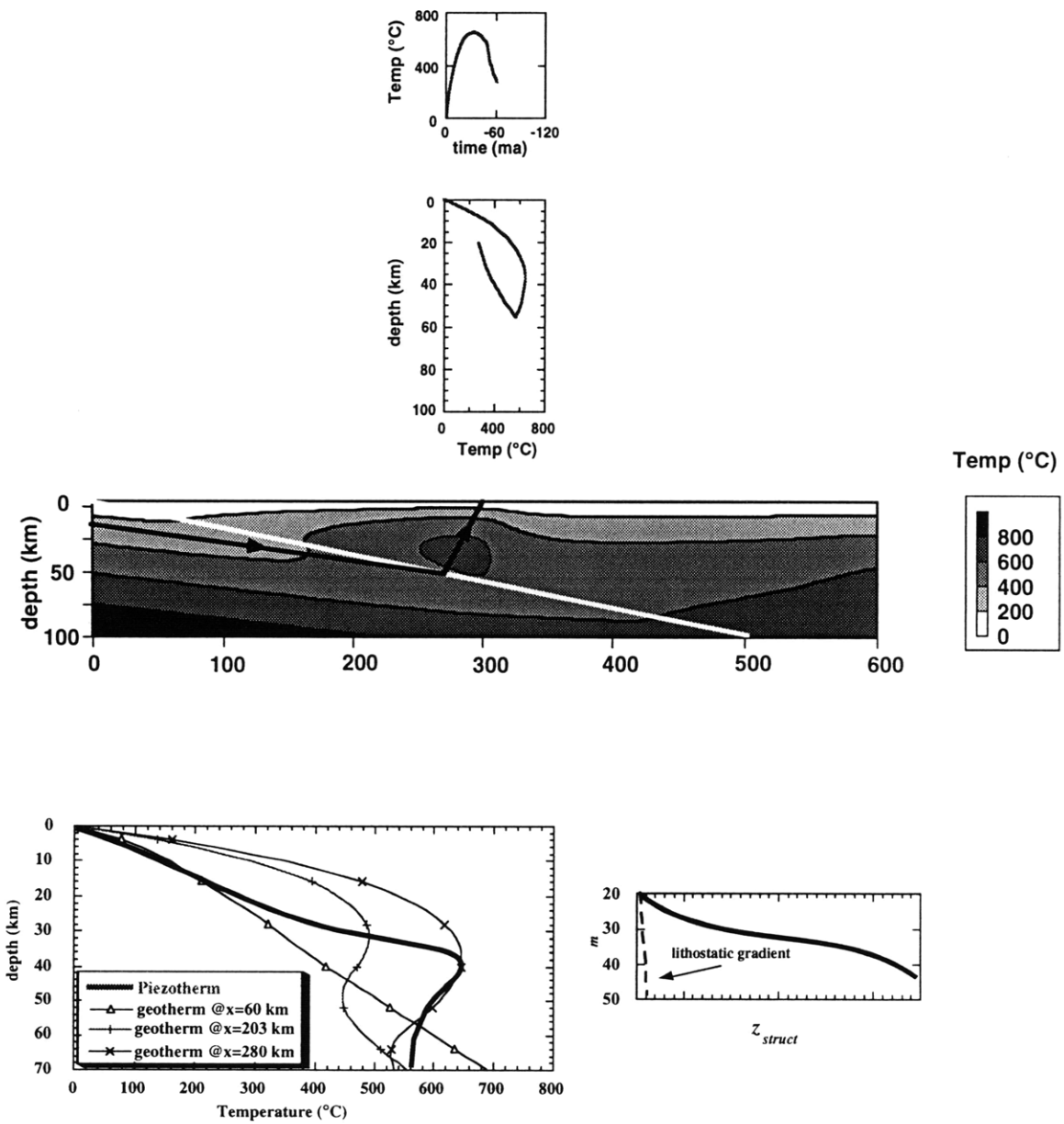


Figure 9

$d_w = 50$ km

$x_{sur} = 305$ km

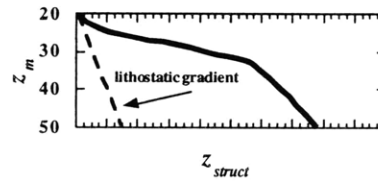
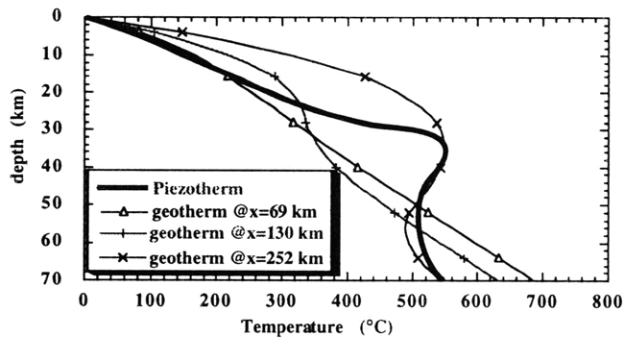
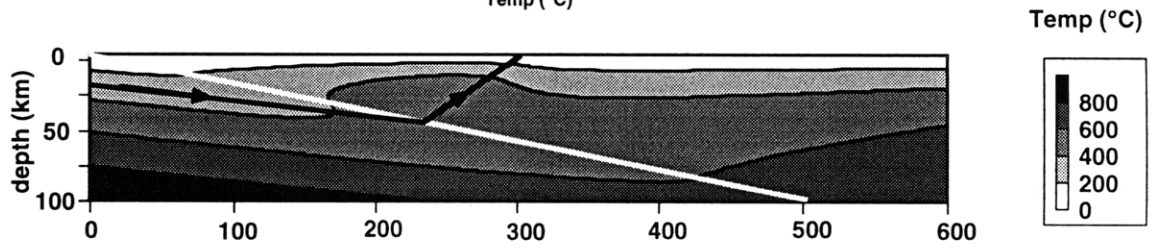
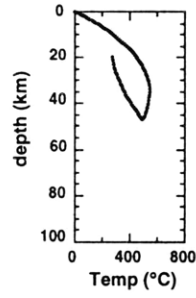
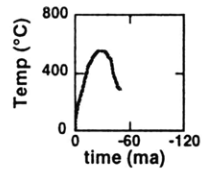


Figure 9, con't

$d_w = 40$ km

$x_{sur} = 305$ km

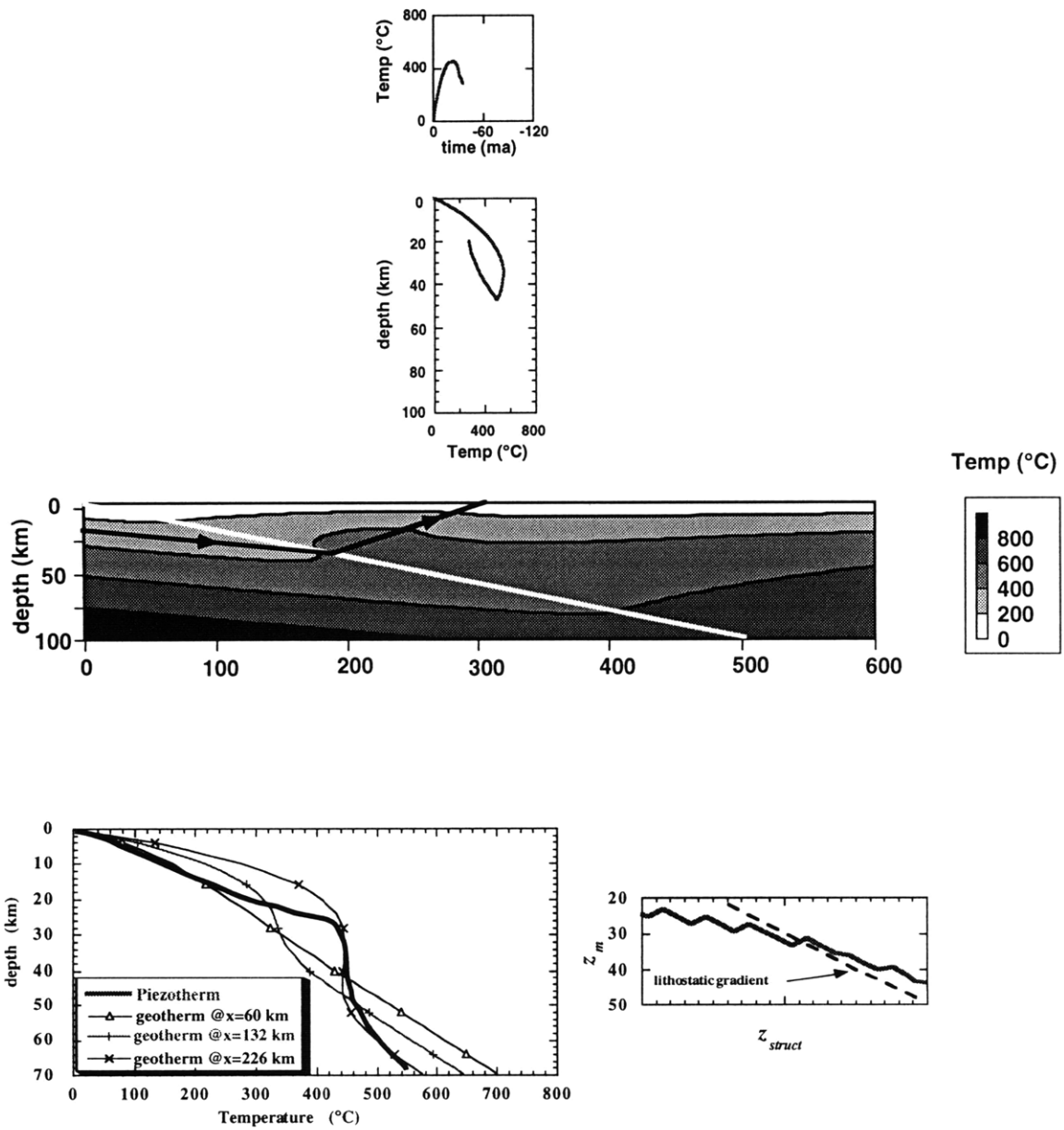


Figure 9, cont't

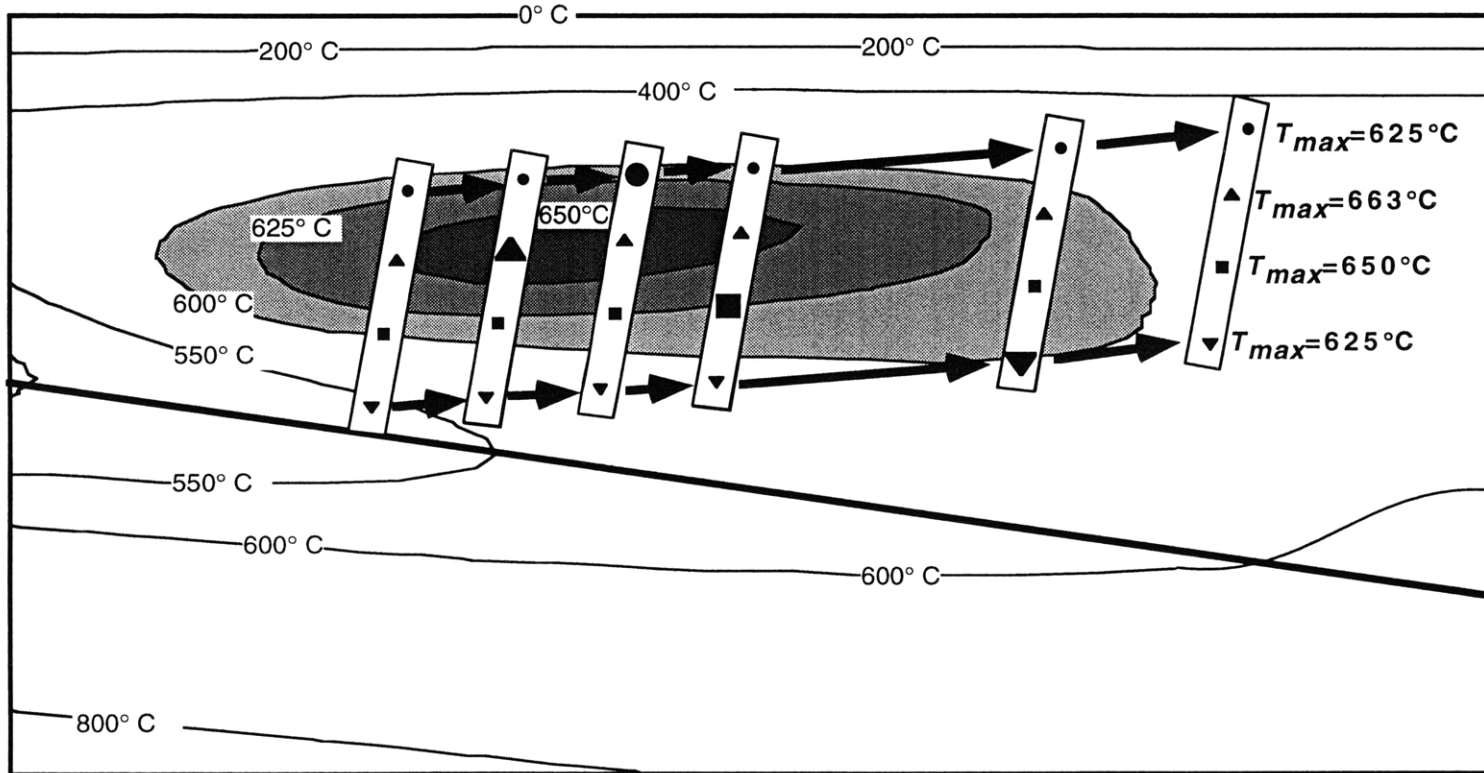
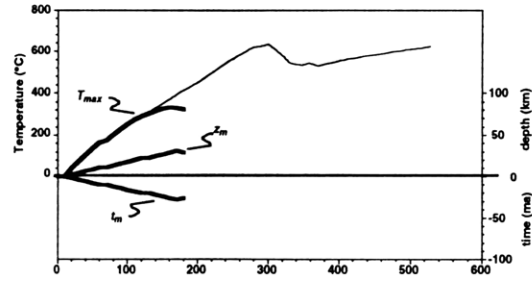
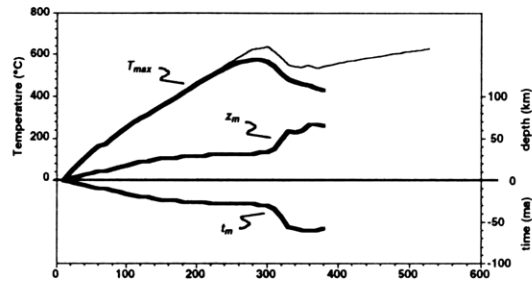


Figure 10

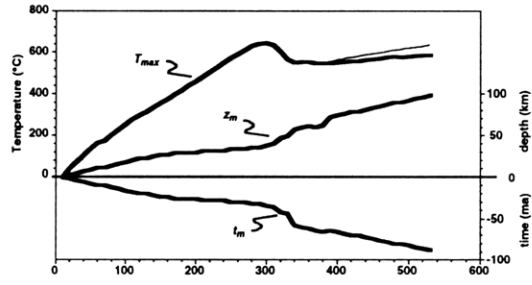
$t=40$ my



$t=80$ my



$t=120$ my



$t=160$ my

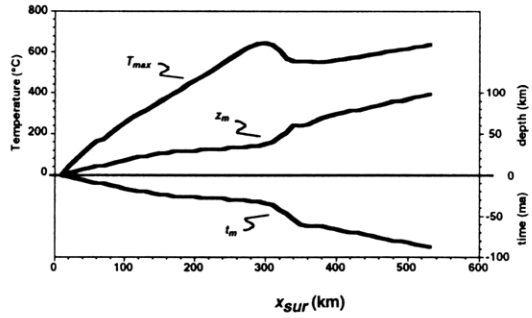


Figure 11

Case A: $a=1.2$ km/my

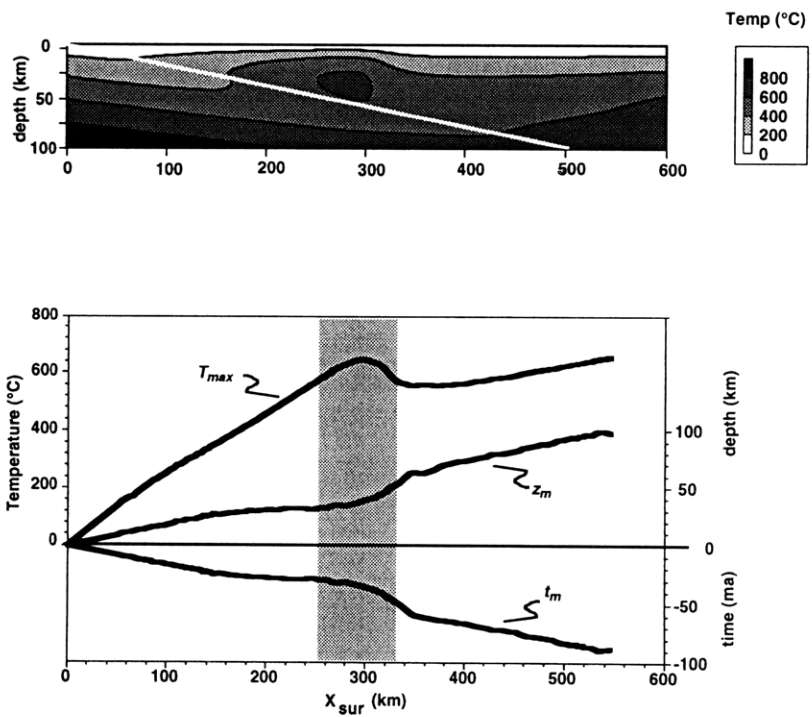


Figure 12

$h=6$ km, $t_g=5.04$ my, $v_c=20.9$ km/my

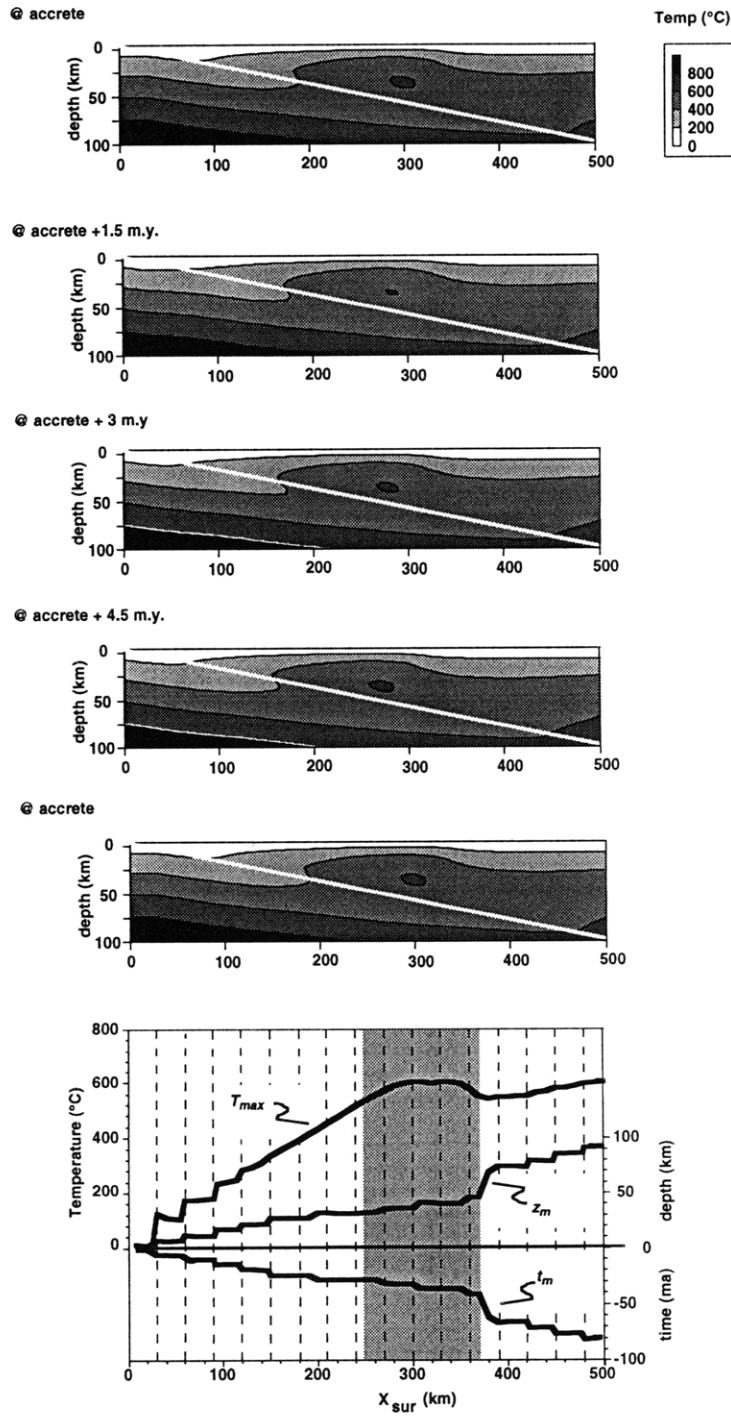


Figure 12, cont

$h=18 \text{ km}$, $t_a=15.2 \text{ my}$, $v_c=22.7 \text{ km/my}$

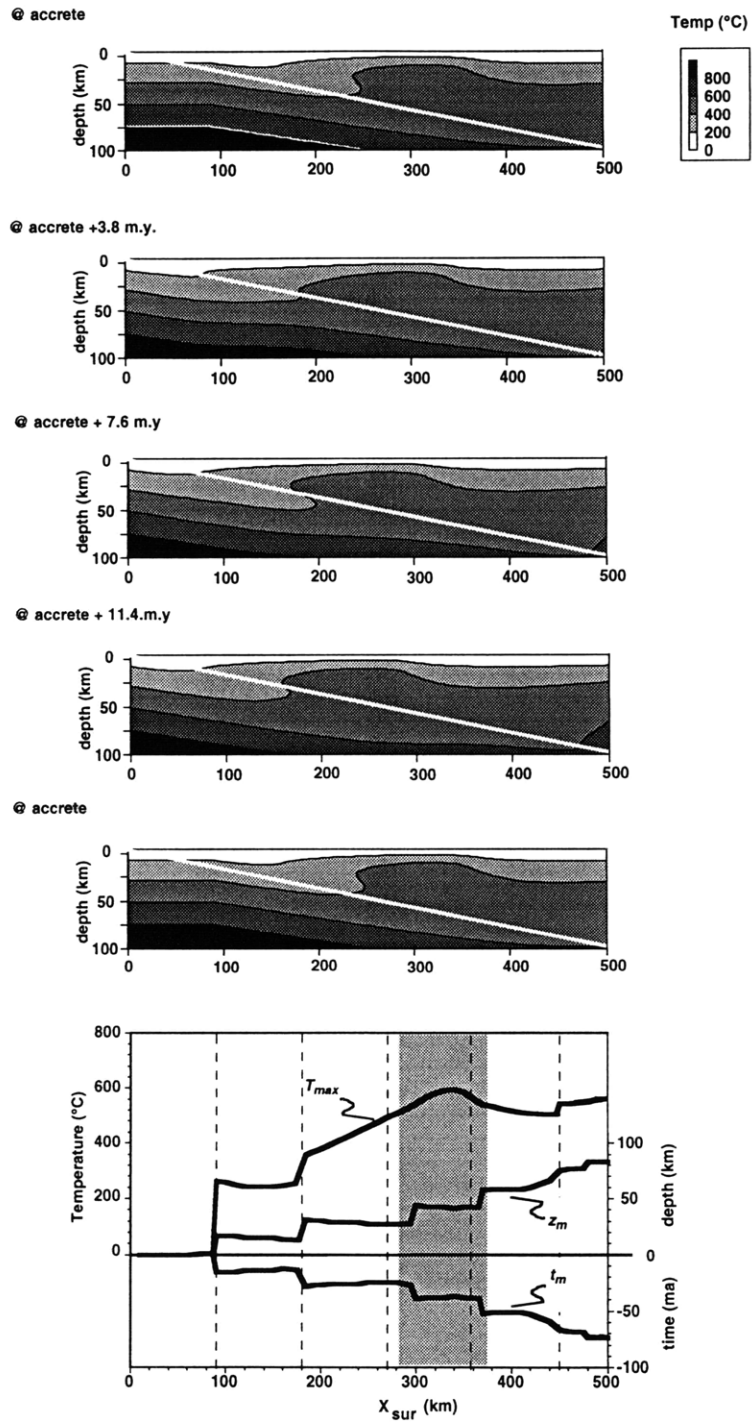


Figure 12, con't

$h = 18 \text{ km}, t_a = 15.2 \text{ my}$

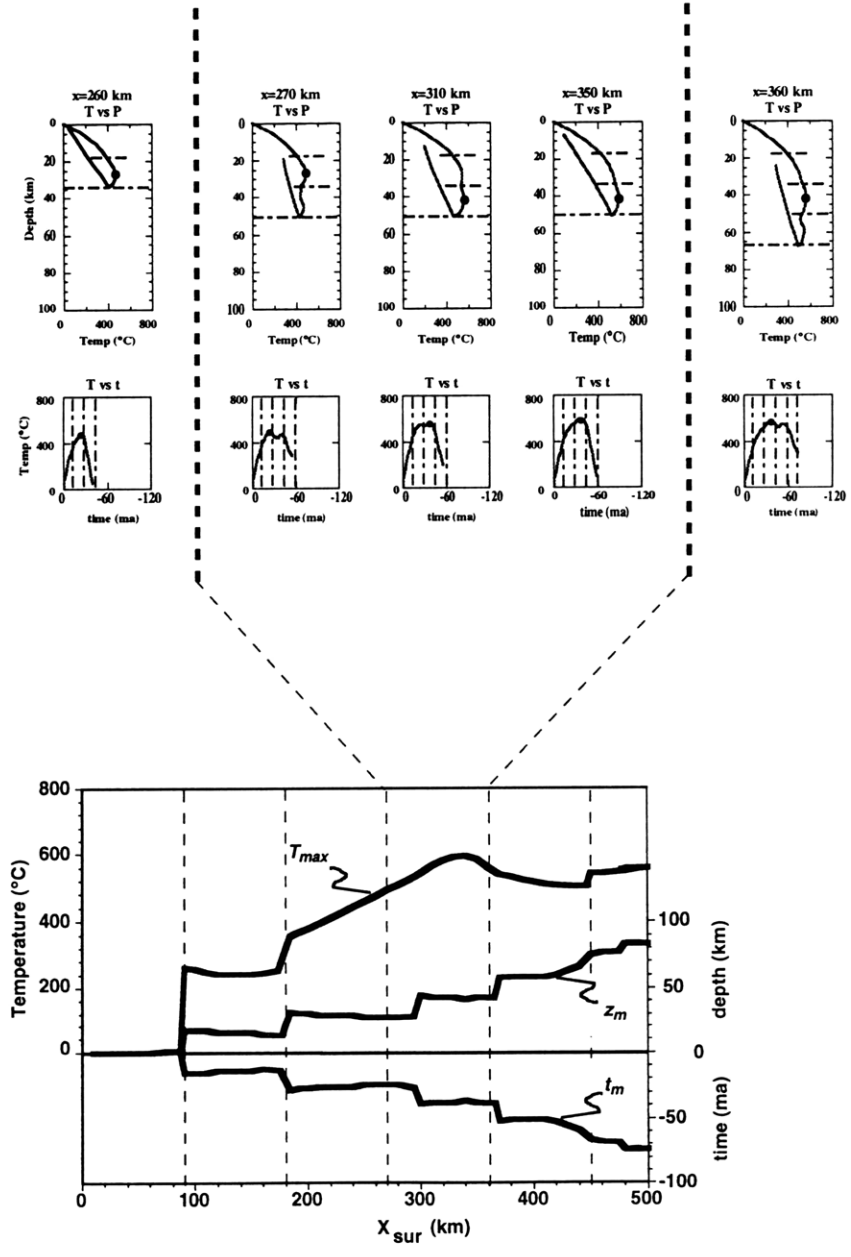


Figure 13

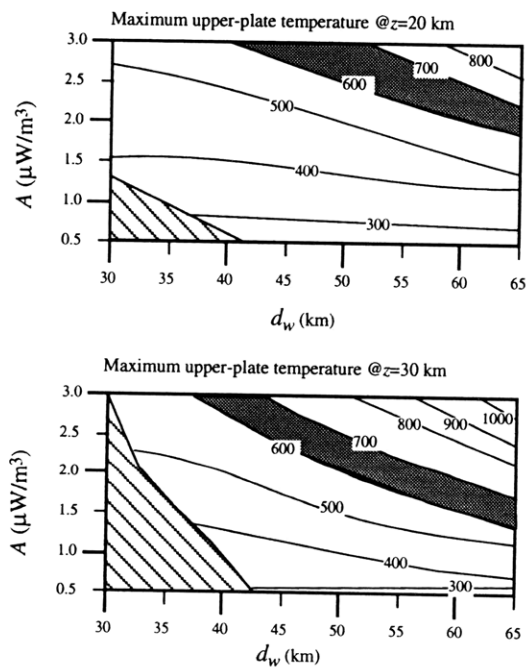


Figure 14

TABLE 1. Definitions of Variables and Values Used

Variable	Physical Meaning	Value or Units	Comments
x	horizontal distance from upper-plate toe	(km)	
z	vertical distance from surface	(km)	
$T(x,y)$	temperature at a location within the orogen	(°C)	
T_{max}	maximum temperature experienced by a rock	(°C)	
z_m	depth at T_{max}	(km)	
t_m	time at T_{max}	(Ma)	elapsed time between T_{max} and surfacing
z_{struct}	structural distance within a column of rock	(km)	measured perpendicular to the subduction boundary
a	accretion rate	(km/my)	vertical component relative to fault surface
h	vertical thickness of accreted slab	(km)	
t_a	period of accretion cycle	(my)	
e	erosion rate	(km/my)	
v_c	convergence velocity	(km/my)	velocity of rocks in the down-going plate relative to rocks in the upper plate
A	radioactive heat production rate	(μ W/m)	
Θ	dip of subduction zone	(11.3°)	
d_r	initial thickness of heat-producing layer	18 km	
s_w	maximum surface width of heat-producing wedge	(km)	
d_w	maximum depth of heat-producing wedge	(km)	
t_w	time to steady state shape of heat-producing wedge	(my)	
t	time since initiation of collision	(my)	
ℓ	thickness of foreland lithosphere	126 km	
T_a	temperature at base of lithosphere	1260° C	
K	thermal conductivity	2.5 W/mK	
α	thermal diffusivity	10^{-6} m ² /s	
τ	time step for thermal model	0.05 my	
Δz	vertical grid spacing	2 km	
Δx	horizontal grid spacing	10 km	$\Delta z/\tan\Theta$
x_{max}	width of area modeled	630 km	$\ell/\tan\Theta$

TABLE 2. Values of Parameters Used in Computing Temperatures in Figures 3-9 , 12 and 13

Figure Number	Comments	Accretion rate (a) km/my	Erosion rate (e), km/my	Heat Production Rate (A) $\mu\text{W}/\text{m}^3$	Maximum Depth of wedge (d_w) km	Surface width of wedge (s_w) km	Time to full development of wedge (t_w) my
3	Case A	1.2	1.12	1.75	60	320	69
4 , 5 a	Case A	1.2	1.12	1.75	60	320	69
b	Case B	1.46	1.0	2.0	54	440	66
c	Case C	2.0	0.93	3.0	45	480	57
6, 7 a	$s_w=320$ km (Case A)	1.2	1.12	1.75	60	320	69
b	$s_w=480$ km	1.33	0.83			480	86
c	$s_w=640$ km	1.39	0.67			640	103
8, 9 a,	$d_w=60$ km (Case A)	1.2	1.12	1.75	60	320	69
b	$d_w=50$ km	1.54	1.2		50		53
c	$d_w=40$ km	2.12	1.33		40		39
11	Case A	1.2	1.12	1.75	60	320	69
12 a	Continuous (Case A)	1.2; continuous	1.12	1.75	60	320	53
b	Thin slab	1.2; 6 km/5 m.y.	1.12		60 (avg)	320 (avg)	53
c	Thick slab	1.2; 18 km/15.2 m.y.	1.12		60 (avg)	320 (avg)	53

Unless otherwise specified, the following values are used in all figures: convergence velocity, $v_c=20$ km/m.y.; subduction angle, $\tan\Theta=0.2$; thermal diffusivity, $\alpha=10^{-6}$ m²/s; thermal conductivity, $K=2.5$ W/mK; lithospheric thickness, $l=126$ km; initial thickness of HPE-enriched layer, $d_r=18$ km; basal lithospheric temperature, $T_a=1260^\circ\text{C}$.

TABLE 3.

Figure Number	Comments	Varied Input Parameters			Thermal Structure		Field Gradients				Tt Paths
		Heat Production rate (A) $\mu\text{W}/\text{m}^3$	Accretion rate (a) km/m.y.	Erosion rate (e) km/m.y.	Maximum Upper Plate Temperature $^{\circ}\text{C}$	Maximum upper plate geothermal inversion $^{\circ}\text{C}/\text{km}$	Distance to metamorphic core km	Peak T_{max} in metamorphic core $^{\circ}\text{C}$	z_m at peak T_{max} km	t_m at peak T_{max} Ma	Cooling Rate # $^{\circ}\text{C}/\text{m.y.}$
4,5 a	Case A	1.75	1.2	1.12	646	-74/18=-4.1	296	646	38	34	31.3
b	Case B	2.0	1.46	1.0	637	-90/22=-4.1	367	637	38	38	25.8
c	Case C	3.0	2.0	0.93	662	-102/24=-4.3	443	662	30	32	19.4

#For sample from metamorphic core cooling from 500° C to 0°C

TABLE 4

Figure Number	Comments	Varied Input Parameters		Thermal Structure		Field Gradients				Tt Paths
		Accretion rate (a) km/m.y.	Erosion rate (e) km/m.y.	Maximum Upper plate temperature $^{\circ}\text{C}$	Maximum upper plate geothermal inversion $^{\circ}\text{C}/\text{km}$	Distance to metamorphic core km	Peak T_{max} in metamorphic core $^{\circ}\text{C}$	z_m at Peak T_{max} km	t_m at Peak T_{max} km	Cooling Rate # $^{\circ}\text{C}/\text{m.y.}$
6, 7 a	$s_w=320$ km (Case A)	1.2	1.12	646	-74/18=-4.1	296	646	38	34	31.3
b	$s_w=480$ km	1.33	0.83	661	-106/26=-4.1	448	661	38.5	46	20.4
c	$s_w=640$ km	1.39	0.67	664	-112/32=-3.5	582	664	41	61	17.1

#For sample from metamorphic core cooling from 500° C to 0°C

TABLE 5

Figure Number	Comments	Varied Input Parameters		Thermal Structure		Field Gradients				Tt Paths
		Accretion rate (a) km/m.y.	Erosion rate (e) km/m.y.	Maximum Upper plate temperature °C	Maximum upper plate geothermal inversion °C/km	Distance to metamorphic core km	Peak T_{max} in metamorphic core °C	z_m at Peak T_{max} km	t_m at Peak T_{max} km	Cooling Rate # °C/m.y.
8, 9 a	$d_w=60$ km	1.2	1.12	646	-74/18=-4.1	295	646	38	34	31.3
b	(Case A)	1.54	1.2	548	-36/12=-3.0	300	548	34.4	29	25.0
c	$d_w=50$ km	2.12	1.33	447	-10/12=-0.8	307	447	31.3	24	18.7
	$d_w=40$ km									

#For sample from metamorphic core cooling from 500° C to 0°C

CHAPTER 4:

CONSTRAINING THE RATES OF OROGENIC PROCESSES FROM PETROLOGIC DATA.

Abstract

The metamorphic record of collisional zones reflects the interplay between the thermal structure of an orogen and the particle paths of rocks advected through the orogen. Since the thermal structure of an orogen is determined primarily by the distribution of crust enriched in heat-producing elements, which is controlled by advective processes, it may be possible to directly relate the metamorphism of an orogen to the deformational and erosional history of the orogen. Here we explore this hypothesis by applying a two-dimensional numerical model to simulate the metamorphic record of orogens in which crust is advected by the processes of subduction, accretion and erosion. Results indicate that metamorphic patterns within orogens are strongly affected by only a few parameters; the advective rates (convergence velocity, erosion rate, and accretion rate), the rate of heat production of the upper crust, and the geometry of the orogen (dip of the subduction zone, thickness of the upper crust). Variations in each of these parameters effects the metamorphic pattern in a unique way.

As a test of the applicability of this model, we compare the observed metamorphic record of the Himalaya to synthetic metamorphic records. Model results generated from independently constrained values of the critical parameters display a broad range of predicted metamorphic patterns. However, when model results are constrained to match specific metamorphic data, the set of successful parameter combinations is a very limited. Variations in any of the parameters by over ~30% results in synthetic metamorphic records that do not satisfy the metamorphic data of the Himalaya. These results imply that when the metamorphic and deformational history of an orogen is well documented, this information can be used to constrain the rates of deformational and erosional processes.

Introduction

The broad spectrum of metamorphic conditions encountered in mountain ranges attests to the complex thermal structure of such settings. An important heat source in continental crust is the thermal energy released during the radioactive decay of elements within the crust. The distribution of these elements plays a critical role in the thermal structure of evolving orogens. Because deformational and erosional processes largely govern the distribution of heat-producing crust in mountain ranges, we would suspect that such processes also largely govern the thermal structure. Indeed, recent numerical experiments exploring the thermal evolution of collisional zones suggest that regional metamorphic patterns are dictated by the geometry and rate of accretion of crust to an orogen and the subsequent removal of crust from the system by erosional or tectonic denudation (Huerta et al., 1996; 1998; submitted). If the processes of accretion and denudation have such control, then observed metamorphic patterns should provide a way to constrain the rates of these processes in ancient orogenic settings.

To begin, we inquire if the processes of accretion and denudation alone can be responsible for metamorphism in orogens by comparing synthetic metamorphic patterns to the observed metamorphism in the Tertiary Himalayan orogen. This mountain belt is sufficiently eroded to display a rich metamorphic history, but still young enough that parameters such as plate convergence rate and regional erosion rates are relatively well constrained. By substituting Himalayan values for these variables into our numerical model, we produce synthetic metamorphic patterns and pressure-temperature-time paths that are remarkably consistent with the metamorphism documented within the Himalaya. However, substitution of the complete range of acceptable parameter values also produces results that are not only inconsistent with Himalayan observations but are also physically impossible. The extreme sensitivity of the model results to the rates and geometry of accretion and denudation suggests that knowledge of the metamorphic evolution of an orogen may be used to deduce the deformational and denudational history of ancient mountain belts. As an example, we show how metamorphic observations in the Nepalese Himalaya may provide better constraints on Tertiary denudation and accretion rates in the Himalayan orogen. Realization of the full potential of this approach requires detailed and well integrated petrologic, geochronologic, and structural studies.

General model description

Huerta et al. (1996; 1998; submitted) described a two-dimensional finite difference model that was developed to simulate the thermal response and metamorphic record of a collisional orogen undergoing accretion and erosion. In the model, one plate of continental lithosphere, with heat-producing crust to a depth of d_r , is continuously subducted beneath another plate of continental lithosphere at velocity v_c (Fig. 1; see Table 1 for symbols, variables, and values used). At the same time, erosion continuously removes material from the surface of the upper plate at rate e , while accretion episodically transfers slabs of the down-going plate (with vertical thickness d_r) to the upper plate with a periodicity of t_a . After each accretion event, subduction continues along a new contact at the base of the accreted slab.

As the orogen develops, the accretion of heat-producing crust from the down-going plate to the upper plate and the erosion of crust from the surface of the upper plate results in the growth of a wedge of heat-producing crust in the toe of the upper plate (Fig. 1). Eventually, the surface width of this wedge increases to the point that a balance is achieved between the amount of heat-producing crust added by accretion and the amount removed by erosion. The time required to reach this condition is

$$t_w = \frac{1}{e} \left[(v_c \sin \theta - e) t_a + d_r \right] + t_a$$

Beyond this stage, the geometry of the heat-producing wedge oscillates with each accretion cycle (Fig. 2). During each cycle, the thickest portion of the wedge varies between a maximum thickness of

$$d_{max} = d_r + t_a (v_c \sin \theta - e)$$

and a minimum thickness of

$$d_{min} = d_r + t_a (v_c \sin \theta - e) - \frac{t_a e}{\tan \theta}$$

with a time-averaged thickness of

$$d_w = (d_{max} + d_{min}) / 2. \quad (1)$$

The surface width of the wedge also oscillates during each cycle, with a maximum width of

$$s_{max} = \left(\frac{d_r}{\tan \theta} \right) * \text{CEIL} \left[\frac{d_{max}}{e * t_a} \right]$$

a minimum width of

$$s_{min} = \left(\frac{d_r}{\tan \theta} \right) * \text{FLOOR} \left[\frac{d_{max}}{e * t_a} \right]$$

and a time-averaged surface width of

$$s_w = s_{max} * \left\{ \left[\frac{d_{max}}{e * t_a} \right] - \text{FLOOR} \left[\frac{d_{max}}{e * t_a} \right] \right\} - s_{min} * \left\{ \left[\frac{d_{max}}{e * t_a} \right] - \text{CEIL} \left[\frac{d_{max}}{e * t_a} \right] \right\} \quad (2)$$

(where $\text{FLOOR}[x] = \text{greatest integer } \leq x$; and $\text{CEIL}[x] = \text{least integer } \geq x$)

Given a constant temperature at the base of the lithosphere (T_a), this redistribution of heat-producing crust controls the thermal evolution of a mountain belt. This is illustrated in Figure 3, where we track the distribution of heat-producing crust and the temperature structure of an orogen in which accretion and erosion are active. Prior to collision ($t < 0$ m.y.), subduction of oceanic lithosphere with no erosion or accretion results in low temperatures within the orogen. Following the initiation of collision ($t > 0$ m.y.), temperatures within the orogen increase as continental lithosphere is subducted, heat-producing crust accumulates within the upper plate, and erosion brings hot, deep material towards the surface. In cases where a moderately-thick wedge develops with a nominal heat production rate ($d_w > 35$ for $A > 1.75 \mu\text{W}/\text{m}^3$), a local temperature maximum arises at mid-crustal levels within the upper plate, and geotherms are inverted within both the upper and lower plates.

Throughout the evolution of the orogen, maximum temperatures within the upper plate are controlled primarily by the thickness of the heat-producing wedge and the heat-production rate of this crust, while the lateral extent of high temperatures within the upper plate is determined by the surface width of the heat-producing wedge in the upper plate (Huerta et. al., 1996; 1998). A few million years after the heat-producing wedge reaches the oscillatory stage, temperatures in the region of the heat-producing wedge reach a maximum, and oscillate up to this maximum during each accretion cycle.

The evolving metamorphic field gradient of an orogen reflects the interplay between the thermal structure of the orogen and the movement of rocks through the orogen by subduction, episodic accretion, and continuous erosion (Fig. 3). Immediately following the first accretion event, rocks exposed at the surface of the just-accreted slab have not been subducted and are unmetamorphosed. Once this slab is accreted to the upper plate, erosion removes material from its surface, exposing rocks that have been at depth. After the next accretion event, this slab is displaced away from the active subduction zone, and weakly metamorphosed rocks are exposed at the surface. As the orogen evolves, accretion displaces each slab farther from the foreland, and continued erosion exposes progressively deeper levels. Each rock particle experiences its peak temperature (T_m) either at the time of accretion or following accretion as it passes through the high-temperature region within the upper plate. Thus, peak metamorphic temperatures, depths (z_m) and ages (t_m) generally increase with distance from the foreland, reflecting deeper erosional levels in slabs located farther from the foreland.

Examining a surface transect across the model orogen after several accretion cycles, we find that peak metamorphic temperatures increase from the foreland in a step-like fashion to a region where T_m reaches a local maximum before smoothly falling off again on the back side. We refer to this zone of maximum metamorphic temperatures loosely as the “metamorphic core” of the orogen. The existence of a metamorphic core in our model is a direct consequence the presence of a local temperature maximum and the inverted geotherms in the upper plate; rocks exposed in the metamorphic core record the high temperature region in the upper plate, while rocks exposed on the back side of the metamorphic core passed below and around the region of high temperatures and record lower peak temperatures.

Two key features of the metamorphic record depend strongly on only a few model parameters: maximum metamorphic temperatures, and the distance from the metamorphic core to the toe of the orogen (Huerta et al., submitted). Maximum metamorphic temperatures are controlled primarily by the thickness of the heat-producing wedge (d_w) and the rate of heat production (A), while the distance from the toe of the orogen to the metamorphic core is controlled by the surface width of the heat producing wedge (s_w). In turn, the average thickness and width of the heat-producing wedge are controlled by the convergence velocity (v_c), erosion rate (e), duration of the accretion cycle (t_a), and the subduction geometry (d_s, θ) through Equations 1 and 2. Thus, our model predicts that a few combinations of the input parameters (A, d_w , and s_w) determine the first-order metamorphic characteristics of collisional orogens.

Each of the input parameters influences the metamorphic evolution of an orogen by affecting either the thermal structure of the orogen and/or the particle paths of rocks moving through the orogen. To investigate the effects of these parameters we independently varied each and compared the resulting synthetic steady-state thermal structures and metamorphic records. We began by determining the thermal structure and metamorphic record of an orogen using nominal values of $A = 2 \mu\text{W}/\text{m}^3$, $v_c = 20 \text{ km}/\text{my}$, $d_r = 20 \text{ km}$, $t_a = 10 \text{ m.y.}$, $e = 1 \text{ km}/\text{my}$, and $\Theta = 15^\circ$ (Fig. 4). This combination of input parameters resulted in a heat-producing wedge with average depth and width of $d_w = 57 \text{ km}$ and $s_w = 460 \text{ km}$. Temperatures within the upper plate reached a local-maximum of $T = 615^\circ\text{C}$ at $z = 36 \text{ km}$, $x = 300 \text{ km}$. Metamorphic temperatures and depths displayed at the surface increased in a step-wise for a distance of $\sim 220 \text{ km}$ from the toe of the orogen. Beyond that point T_m increased smoothly to the metamorphic core at $x \sim 420 \text{ km}$, where metamorphic temperatures reached a local maximum of $T_m \sim 615^\circ$ at depths of $z_m = 34 \text{ km}$. For comparison, we investigated variations in the input parameters designed to produce a cooler upper plate.

Decreasing heat production rate, A

Decreasing the heat-production rate by a factor of two ($A = 1 \mu\text{W}/\text{km}^3$) resulted in a much cooler orogen and lower metamorphic temperatures than in the original model orogen. Geotherms were inverted below a region of maximum upper-plate temperatures, and the resulting metamorphic core had maximum temperature of $T_m = 435^\circ\text{C}$ at $z_m = 34 \text{ km}$. Since particle paths were unchanged, the locations of the maximum upper plate temperatures and the metamorphic core were relatively unchanged.

Decreasing convergence velocity, v_c

Decreasing the convergence velocity by a factor of two ($v_c = 10 \text{ km}/\text{my}$) resulted in a shallower and narrower heat-producing wedge ($d_w = 31 \text{ km}$, $s_w = 270 \text{ km}$). At low convergence velocities cool portions of the down-going plate were not subducted to great depths, resulting in higher temperatures near the subduction zone and relatively flat upper-plate isotherms. Since no local temperature maximum developed in the upper plate, then no metamorphic core developed.

Decreasing thickness of the accreted slab, d_r

Decreasing the thickness of the accreted slab by a factor of two ($d_r = 10 \text{ km}$) resulted in a slightly shallower and significantly narrower heat-producing wedge ($d_w = 47 \text{ km}$, $s_w = 190 \text{ km}$). Upper plate temperatures were cooler than in the original model orogen, and

the upper-plate temperature maximum was positioned closer to the toe. Decreasing d , steepened particle paths in the upper plate, and the metamorphic core was centered closer to the toe of the orogen ($x \sim 180$ km), with cooler maximum metamorphic temperatures of $T_m = 385^\circ\text{C}$.

Decreasing accretion period t_a

Decreasing the accretion period by a factor of two ($t_a = 5$ my) produced a shallower and wider heat-producing wedge ($d_w = 38$ km, $s_w = 610$ km). Maximum temperatures in the orogen were cooler and located closer to the foreland. Decreasing the accretion rate also resulted in shallower particle paths in the upper plate, and the metamorphic core was farther from the toe of the orogen ($x \sim 660$ km) with cooler maximum metamorphic temperatures of $T_m = 416^\circ\text{C}$.

Increasing erosion rates, e

Increasing erosion rates by a factor of two ($e = 2$ km/my) resulted in a shallower and narrower heat-producing wedge ($d_w = 42$ km, $s_w = 195$ km). Maximum upper plate temperatures were cooler and located closer to the toe of the orogen than in the original model orogen. Higher erosion rates steepened particle paths in the upper plate, and the metamorphic core was centered closer to the toe of the orogen ($x \sim 180$ km), with cooler maximum metamorphic temperatures of $T_m = 490^\circ\text{C}$.

Decreasing dip of the subduction boundary, θ

Decreasing the dip of the subduction zone by a factor of two ($\theta = 7.5^\circ$) decreased the thickness and increased the width of the heat-producing wedge ($d_w = 31$ km, $s_w = 550$ km). At a low subduction angle, cool portions of the down-going plate were not subducted to great depths, resulting in higher temperatures near the subduction zone and relatively flat upper-plate isotherms. Since no local temperature maximum developed in the upper plate, no metamorphic core developed.

Implications

Each of the model orogens examined in our sensitivity analysis has a distinct metamorphic pattern. Varying any single parameter affected either the particle paths of rocks in the upper plate and/or the thermal structure of the orogen, factors which directly control the maximum temperature and location of the metamorphic core. Thus, although we

selectively varied each parameter such that temperatures in the orogen were reduced, metamorphic temperatures at a given location were not necessarily lower. Each variation affected the field gradient in a unique way, with distinct predicted maximum temperatures and location of the metamorphic core (if present). The results indicate that these parameters can exert first-order control on the metamorphic evolution of an orogen, and that a given metamorphic pattern may be the result of a unique combination of parameters. We look to the central Himalaya to test this hypothesis, where the metamorphic evolution has been extensively studied and critical input parameters can be fairly well constrained. Synthetic metamorphic patterns based on these input parameters are then compared with the actual metamorphic patterns.

Modeling the Himalayan Orogen

The Himalayan orogen, one of the most striking examples of continental deformation and metamorphism, formed as a consequence of collision and subsequent convergence of the Indian and Eurasian continents (Gansser, 1964; Patriat & Achache, 1984). Initial collision was accommodated along the Indus-Tsangpo suture zone, which marks the contact between Indian crust to the south and Eurasian crust to the north. The zone of convergence between India and Eurasia has migrated to the south with time, and today it is accommodated within Indian lithosphere ~300 km south of the Indus-Tsangpo suture zone. Between the presently active convergence zone and the original suture zone, slabs of Indian crust have been accreted to the orogen along relict subduction zones (Fig. 5). In addition to these crustal-scale thrust zones, the orogen has been disrupted by normal faults exposed near the range crest. These normal-movement structures, collectively referred to as the South Tibetan detachment system (STDS; Burchfiel et al., 1992), are thought to have helped moderate the crustal thickness gradients in the region since Neogene time (Burchfiel & Royden, 1985).

Thus, four north-dipping, orogen-scale fault systems divide the Indian crust into four distinct tectonostratigraphic zones, each of which display different degrees of metamorphism. Immediately south of the suture zone is the Tibetan zone which consists of predominately unmetamorphosed sedimentary rocks. Its southern boundary is the South Tibetan detachment system. Beneath the detachment system, the Greater Himalayan zone contains amphibolite facies rocks and defines the metamorphic core of the orogen. The upper half to two-thirds of the section typically exhibits evidence of anatexis during Himalayan metamorphism (Gansser, 1964; Burg et al., 1984; Grujic et al., 1996; Hodges et al., 1996; Pecher, 1977). The Main Central thrust (MCT) system, a north-dipping relict

subduction zone, separates the Greater Himalayan zone from the underlying Lesser Himalayan zone (Brunel & Kienast, 1986; Gansser, 1964; Le Fort, 1975; Pecher, 1989). Rocks of the Lesser Himalayan zone are weakly metamorphosed (chlorite-garnet grade) in most areas, although in some transects the uppermost rocks contain amphibolite facies assemblages (Pecher, 1978). The Main Boundary thrust system, another north-dipping intracontinental subduction zone, separates the Lesser Himalayan zone from the underlying the Subhimalayan zone. Rocks within the Subhimalayan zone consist of folded and faulted foreland basin molasse. The Main Frontal thrust system marks the base of the Subhimalayan zone and currently accommodates some of the convergence between the Himalayan orogen and the Indian plate (Johnson et al. 1979; Alam, 1989; Najman et al., 1993).

Within and adjacent to the Greater Himalayan zone, metamorphic and igneous rocks commonly contain mineral assemblages appropriate for thermobarometric and thermochronologic analysis, providing information on the thermal and deformational history of the Himalayan metamorphic core. Although details vary from location to location throughout the central Himalaya, rocks within the Greater Himalayan zone experienced Oligocene (Eohimalayan) intermediate-pressure, high-temperature metamorphism followed by Miocene (Neohimalayan) intermediate- to low-pressure, high-temperature, metamorphism (Hodges et al., 1988; Pecher, 1989). The Eohimalayan event has been obscured throughout much of the central Himalaya by subsequent metamorphism, however, relict assemblages from a few areas reveal Eohimalayan temperatures of $\sim 400^{\circ}\text{C}$ to 600°C and pressures of ~ 350 MPa near the top of the Greater Himalayan zone, increasing to temperatures of ~ 450 - 700°C and pressures of ~ 1200 MPa at the base (Fig. 6a; Swapp & Hollister, 1991; Hodges et al, 1994; Hodges & Silverberg, 1988; Macfarlane, 1995; Pognante & Benna, 1992; Brunel & Kienast; 1986). Most data suggest an age ~ 35 - 40 Ma for Eohimalayan metamorphism (Inger & Harris, 1992; Coleman, in press; Hodges et al, 1996), although ages as young as ~ 25 Ma have been suggested (Hodges et al., 1994). During the Miocene, Neohimalayan metamorphism was synchronous with anatexis and emplacement of leucogranite bodies within the Greater Himalayan zone, as well as displacement along both the Main Central thrust and South Tibetan detachment systems. Temperatures ranged from 450°C to 800°C at pressures of 350 MPa to 1100 MPa (Fig. 6b; Inger & Harris, 1992; Hodges et al, 1988; Hodges et al., 1993; Hubbard, 1989; Macfarlane, 1995).

Structural studies show that early shearing fabrics related to the Main Central thrust system developed synchronously with Neohimalayan metamorphism of the Greater

Himalayan zone (Hubbard, 1988; Parrish & Hodges, 1993; Hodges et al., 1996; Coleman, in press; Hodges & Silverberg, 1988; Metcalfe, 1993). Although neither the exact age of initiation nor the duration of movement on the MCT system are constrained, syn-metamorphic movement on the MCT has been dated at ~22.5-18 Ma (Hubbard and Harrison, 1989; Parrish and Hodges, 1996; Hodges et al., 1996; Coleman, in press), while recently obtained Th-Pb ages for monazites from the MCT zone suggest that at least some syn-metamorphic thrust movement occurred in Miocene-Pliocene time (Harrison et al., 1997). In some areas, there is a distinct metamorphic break at the MCT system, indicating that some movement was clearly post-metamorphic (Gansser, 1964; Hodges & Silverberg, 1988; Caby et al., 1983; Macfarlane et al., 1992; Macfarlane, 1992; Brunel & Kienast, 1986, Hodges et al, 1996).

One of the most distinctive characteristics of the Himalaya is the common occurrence of inverted metamorphic gradients. Throughout the central and eastern portions of the orogen, the degree of metamorphism within the Greater Himalayan zone increases structurally upward from kyanite grade to sillimanite grade (Gansser, 1966; Le Fort, 1975). Results of quantitative thermobarometry also display metamorphic temperatures that increase with structural distance above the base of the section (Fig. 7; Macfarlane, 1995; Hubbard, 1989; Hodges et al., 1988). Since the metamorphic pressure gradients across the sections are nominally consistent with a lithostatic gradient, these results have been interpreted as preserved inverted geothermal gradients.

In several areas, an inverted metamorphic gradient also exists below the MCT in the underlying Lesser Himalayan zone, passing downwards from garnet grade to chlorite grade (Le Fort, 1975). Traditionally, Himalayan geologists inferred a genetic relationship between the two metamorphic inversions, but recent studies suggest that metamorphism in the Lesser Himalayan zone may be a Late Miocene-Pliocene phenomenon (Harrison et al., 1997). Thus, although metamorphic grade appears to increase smoothly across the MCT system, in some cases metamorphism of the Lesser Himalayan zone may be much younger than Neohimalayan metamorphism of the Greater Himalayan zone.

Our present level of understanding of the Himalayan orogen permits us to limit, but not closely constrain, a variety of parameters that are of fundamental importance to the thermal and mechanical evolution of the range: the duration of collision (t); the dip of the subduction zone (θ); the convergence velocity (v_c); the period of accretion (t_a); the thickness of accreted slabs (d_r); the heat production rate of the upper crust (A); and the time-integrated erosion rate (e).

Duration of collision (t)

The exact timing of collision between India and Eurasia certainly varies along the Indus-Tsangpo suture, and current estimates range from 65-38 Ma (Rowley, 1996; Searle, 1986; Searle et al., 1988; Klootwijk et al., 1992). In the Western Himalaya stratigraphic evidence suggests that suturing may have initiated before 55.5 Ma, and perhaps as early as 66 Ma (Beck et al., 1995). The general transition from oceanic subduction to continental collision is thought to be reflected by the decrease in convergence rate sometime between 55-40 Ma (Patriat & Achache, 1984), while the marked decrease in convergence rate and rotation of India with respect to Eurasia since ~45 Ma is interpreted as marking the time of complete collision (Dewey et al., 1989). Although the exact timing of collision in the central Himalaya is still unknown, we use a range of

$$40 \text{ Ma} \leq t \leq 60 \text{ Ma}$$

Parameter range 1

Dip of the subduction zone (θ)

Based on gravity measurements, a regional dip of 7.5-15° has been determined for the Main Frontal thrust in the Himalayan foreland (Lyon-Caen & Molnar, 1985), while seismic imaging reveals a dip of 7.5° for the basal decollement beneath the High Himalaya (Makovsky et al, 1996). Although the initial dips of the intracontinental subduction zones are unknown, it is likely that their geometry was similar to the geometry today. Thus we take the dip of the subduction zones as

$$7.5 \leq \theta \leq 20^\circ$$

Parameter range 2

Convergence velocity (v_c),

Convergence velocity between the Himalaya and the subducting Indian continent over the last 15-20 m.y. has averaged 10 -15 km/m.y. (Lyon-Caen and Molnar, 1985), while GPS measurements indicate a modern convergence rate of ~20 km/my (Bilham et al., 1997). Assuming that convergence velocity has not varied significantly over the history of collision, we assume that the range of convergence rates has been

$$10 \text{ km/my} \leq v_c \leq 20 \text{ km/my}$$

Parameter range 3

Accretion period (t_a),

One method to estimate the accretion period(t_a) is to divide the duration of collision by the number of subduction boundaries. Since three relict subduction zones have accommodated convergence over the past 60-45 m.y. (movement on the current subduction zone initiated recently), this approach permits a range of estimated accretion periods between 20 m.y. and 15 m.y. Another method for estimating the accretion period involves estimating the elapsed time between principal movement on the MCT and the next-youngest fault, the MBT. Uncertainties on the age and movement history of these structures to an even broader range of estimates for the accretion period: 9-23 Ma. We adopt the conservative range since it includes estimates provided by the alternative method:

$$9 \text{ my} \leq t_a \leq 23 \text{ my} \quad \textit{Parameter range 4}$$

Thickness of the accreted slabs (d_r),

The present-day structural thickness of the Greater Himalayan zone ranges from <10 km to a maximum of ~25 km, providing the most direct constraint for the thickness of the accreted slabs (Le Fort, 1975). Variations in thickness are, in part, due to the overlying South Tibetan detachment system which has removed varying amounts of the Greater Himalayan zone. Additional irregularities in the thickness are due to internal deformation (e.g., Hodges et al., 1996; Grujic. et al, 1996). Although it is impossible to determine the original, undeformed thickness of the Greater Himalayan zone, we use the present-day thickness range of

$$10 \text{ km} \leq d_r \leq 25 \text{ km} \quad \textit{Parameter range 5}$$

Heat production rate in the upper crust (A),

Calculated heat production rates based on measured chemistry of rocks within the Himalaya range from ~1.5 to >8 $\mu\text{W}/\text{m}^3$, with over 25% of measured values exceeding 4 mW/m^3 (Vidal et al., 1982; Scharer, 1984; Scharer et al., 1986; Copeland et al., 1988; Cuney et al., 1984; Scaillet et al., 1990; Vidal et al., 1982; Macfarlane, 1992). These values are similar to heat production rates of rocks of the northern Indian shield, the ultimate source for the sediments that now make up the metamorphic rocks within the Himalaya (Parrish and Hodges, 1996; Rao et al. 1976). Thus, the range of heat production rates used as input parameters is

$$1.5 \mu\text{W}/\text{m}^3 \leq A \leq 8 \mu\text{W}/\text{m}^3$$

Parameter range 6

Erosion rate (e).

Given evidence for significant displacement on the South Tibetan detachment system, the unroofing history of the Himalaya include both tectonic denudation and simple erosion. For the purposes of modeling, both can be treated together as “augmented” erosion. Estimates of long-term, regional erosion rates within the Himalaya range from 0.5-5 km/m.y. (Corrigan & Crowley, 1989; Hubbard et al., 1991), while denudation rates locally as high as 5-10 km/m.y. have been inferred (Copeland & Harrison, 1990; Hodges et al, in press; Burbank et al., 1996). We use the range

$$0.5 \text{ km/my} \leq e \leq 10 \text{ km/my}$$

Parameter range 7

Additional constraints

The above geologic and geophysical data limit individual input parameters, but, additional data can be used to constrain appropriate combinations of parameters.

Heat Flow: Combinations of heat production rate and thickness of the accreted slabs can be further constrained such that modeled foreland heat flows are consistent with present-day foreland heat flows of 56-80 mW/m² (Rao et al, 1976) Using the heat flow equation for a two layer lithosphere, we constrain combinations of A and d_r such that

$$58 \mu\text{W}/\text{m}^3 \leq K * \left[\frac{T_a}{l} + \left(\frac{A}{K} \right) * \left(d_r - \frac{d_r^2}{2l} \right) \right] \leq 80 \mu\text{W}/\text{m}^3$$

Parameter range 8

Width of orogen: The present-day amount of accreted crust, $d/(t*\tan\Theta)$, can be constrained by the map distance between the suture zone and presently active zone of convergence. Although variable along strike, the typical distance is ~300 km in the central Himalaya. Since this region has been affected by both shortening and internal extension, the non-deformed length is unknown (Schelling & Arita, 1991; Searle, 1986; Burg et al., 1984; Burchfiel et al., 1992). We constrain combination of d_r , t , and Θ such that

$$250 \leq d_r/(t*\tan\Theta) \leq 400 \text{ km}$$

Parameter range 9

Results

Unfortunately, there is no way to independently determine which combination of the above parameters is precisely appropriate to the evolution of this orogen. Instead of investigating all possible parameter combinations, we chose two extreme combinations. The first results in an orogen with the coldest possible thermal structure and metamorphic record. The second results in an orogen with the hottest possible thermal structure and metamorphic record.

The cold combination assumed a cold foreland geotherm ($A=3.5 \mu\text{Wm}^3$, $d_f=10 \text{ km}$, and $q_{\text{foreland}}= 58 \mu\text{W/m}^3$). It is characterized by a narrow orogen that developed in a short time ($d=280 \text{ km}$, $t= 45 \text{ my}$), a shallow heat-producing wedge ($d_w=18 \text{ km}$), and was based on low erosion rates ($e=0.5 \text{ km/my}$) (Fig. 8). In this case, maximum temperatures in the upper plate were very low; in fact, temperatures at any depth in the orogen were cooler than temperatures at corresponding depths in the foreland. Metamorphic temperatures and pressures across the orogen were also very low, with maximum temperatures in the core of $T_m \sim 200^\circ\text{C}$ at $z_m= 15 \text{ km}$. The hot example assumed a foreland with high heat flow ($A=2.4 \mu\text{Wm}^3$, $d_f=25 \text{ km}$, and $q_{\text{foreland}}= 80 \mu\text{Wm}^3$). It represents a wide orogen that developed over a long time ($d=380 \text{ km}$, $t=60 \text{ my}$), with a deep heat-producing wedge ($d_w=91 \text{ km}$). In this case, we assumed an erosion rate of ($e=1.25 \text{ km/my}$). The resulting temperatures in the upper plate exceeded 1000°C at depths of 40-50 km, and the metamorphic record exhibited maximum metamorphic temperatures of $\sim 650^\circ\text{C}$ at depths of $\sim 30 \text{ km}$.

Thus, although the permissible parameter ranges can reproduce Himalayan metamorphism, they can also reproduce nearly all observed metamorphic records in the continental crust. However, the sensitivity of the model to estimated parameters suggests that perhaps we can turn the problem around: Can the metamorphic and deformational history of the Himalaya be used to better constrain some of the critical parameters in its evolution?

Metamorphic and deformational constraints

Generalized results of our thermal model indicate that two facets of the metamorphic record – the distance between the toe of the orogen and the metamorphic core (related to the average surface width, s_w) and the maximum temperatures recorded within the metamorphic core – can be used to limit the rates of tectonic processes acting within the orogen. In the central Himalaya, the average surface width of the heat-producing wedge (s_w) is constrained to be $> \sim 150 \text{ km}$ - the distance between the Main Frontal thrust (at the toe of the

orogen) and the Greater Himalayan zone (the metamorphic core of the orogen). Allowable combinations of the heat-production rate (A) and average maximum thickness of the heat-producing wedge (d_w) can be constrained by the observed peak metamorphic temperatures of 600°-800°C (Fig. 9). Applying these constraints of s_w , d_w , and A , and independently constrained values for the subduction velocity ($v_c=10-20$ km/my), subduction angle ($\Theta=7.5-20^\circ$), and slab thickness ($d_r=10-25$ km) to equations 2 and 3, we arrive at estimates of a time-averaged accretion rate of 0.4 km/my $<d/t_a < 2.4$ km/my, and an erosion rate of 1.1 km/my $<e < 2.5$ km/my. These estimates lie within the independently constrained ranges discussed earlier of 0.4 km/my $<d/t_a < 2.8$ and 0.5 km/my $<e < 10$ km/my, but are much more restrictive.

Although this approach yields a relatively broad range of possible accretion and erosion rates, we can further constrain these parameters by forcing model results to match the detailed geometry and timing of deformation and metamorphism in the Himalaya. Two additional aspects of the Himalaya provide important constraints on the metamorphic evolution:

- *Structural Position of the metamorphic core.* The Greater Himalayan zone is underlain by two accreted slabs (the Lesser Himalayan zone and the Subhimalayan zone), and the base of the Greater Himalayan zone is located ~150 km from the toe of the orogen. Thus, we can further constrain allowable combinations of d_r and Θ such that $2*d_r/\tan\Theta \sim 150$ km.
- *Timing and depth of metamorphism:* Thermochronologic and thermobarometric results indicate that at the base of Greater Himalayan zone metamorphism occurred coeval with movement on the Main Central thrust at ~20 Ma at depths of 25-30 km.

Model results match observations within the Himalaya very well; including the general geometry of the orogen, metamorphic conditions within the core, and timing of metamorphism and deformation (Fig. 10). Results not only satisfy these constraints, additional aspects also match the geology of the Himalaya. These include: metamorphic grade increases with distance from the foreland with distinct breaks in grade at each of the relict subduction zones; an inverted metamorphic gradient is predicted within the Greater Himalaya-equivalent; and metamorphic conditions in the equivalent of the Lesser Himalayan zone are generally consistent with chlorite grade metamorphism observed; and timing of

metamorphism within the Lesser Himalayan-equivalent at 10 Ma are similar to reported ages of 5-8 Ma (Harrison et al., 1997).

Although results of this model display an inverted temperature gradient within the metamorphic core, calculated metamorphic depths across the core do not display a lithostatic gradient. One factor that may account for this discrepancy between predicted and observed metamorphic depths is that rocks of the Greater Himalayan zone have experienced post-metamorphic tilting and presently have a dip of $\sim 30^\circ$. If we take this into consideration and calculate metamorphic depths along a crustal section oriented 30° to the subduction zone the metamorphic pressure gradient is consistent with a lithostatic gradient (Fig. 11). The preservation of metamorphic pressure gradients equivalent to a lithostatic gradient has been interpreted as a direct record of the geothermal gradient, i.e., the instantaneous recording of temperatures within a vertical column of crust. However, results from Fig. 11 suggest that this need not be the case. Note this structural section of the crust was never a vertical column of rocks, and although all the metamorphic ages across the section are “geologically instantaneous” at ~ 20 Ma, the metamorphic temperature gradient is not a vertical geotherm.

Maximum metamorphic temperatures predicted in this model are lower than the temperatures recovered by quantitative thermobarometry along some transects (Fig. 7). In addition, there is a growing body of evidence that at least some of the anatexis in the Greater Himalayan zone occurred under fluid-absent conditions, requiring temperatures in excess of 700°C (Inger & Harris, 1993, Harris & Massey, 1994). In our model, temperatures of $>600^\circ\text{C}$ can not be predicted without exceeding one or more of the geologic constraints, implying that accretion and erosion and the attendant redistribution of heat producing crust are not the only factors controlling the thermal structure of the orogen. Additional factors may be heating due to friction along the fault, or additional thickening of the heat producing wedge due to internal deformation.

Pressure-temperature paths of rocks at the base of the metamorphic core in our model are consistent with early metamorphism at relatively high temperatures and pressures followed by re-equilibration at higher temperatures and lower pressures. These events could correspond to the Eohimalayan and Neohimalayan events in the Himalaya. However, temperature changes predicted ($25\text{-}50^\circ\text{C}$) are not as great as those sometimes observed in the Himalaya ($>100^\circ\text{C}$), and predicted maximum depths occur at ~ 25 Ma, while timing of Eohimalayan metamorphism appears to be significantly older, at $\sim 30\text{-}35$ Ma.

A major inconsistency between the synthetic orogen and observations in the Central Himalaya is the prediction of a fourth intracontinental subduction zone. This additional subduction zone is required by the model to bury and metamorphose the Greater Himalayan equivalent. Although no subduction zone above the Greater Himalayan zone has been observed, its existence has been previously postulated to account for Eohimalayan metamorphism (Hodges & Silverberg, 1988; Pognante & Benna, 1992; Vannay & Hodges, 1996).

The synthetic metamorphic record discussed above was based on input parameter values of $v_c=20$ km/my, $A=3 \mu\text{W}/\text{m}^3$, $\Theta=15^\circ$, $t_a=12.5$ my, $d_r=20$ km, and $e=1.4$ km/my. Although this set of parameters is not the only one capable of producing results that satisfy the geologic constraints, the extreme sensitivity of our model implies that the range of appropriate parameter combinations is limited. Since the geometry of the heat-producing wedge exerts such a strong control on the metamorphic record, any changes to the advective rates (v_c , t_a , and e) or geometry of the orogen (Θ , d_r) will result in synthetic metamorphic patterns that are significantly different than the observed metamorphism within the Himalaya. We can compensate for this by varying multiple parameters to produce a wedge geometry and heat production rate that will still result in high-temperature, low-pressure metamorphism. However, even in these cases, variations in any one of the input parameters by a significant amount (~30%) produces results that are inconsistent with geologic constraints (Table 2). For example, increasing the thickness of the accreted slab while maintaining metamorphic temperatures in excess of 600°C in the core results in metamorphic depths in excess of 35 km, significantly deeper than those recovered by thermobarometry.

Conclusions

A straightforward, two-dimensional thermal model of collisional orogens that incorporates the processes of accretion and erosion is capable of reproducing the metamorphic patterns observed within collisional belts, including the common occurrence of high-temperature low-pressure metamorphism and the preservation of inverted geotherms. The general similarity between the modeled metamorphic record and observed metamorphism suggests that accretion and erosion may be fundamental to the thermal evolution of orogens.

The predicted metamorphic evolution is controlled by only a few input parameters: the convergence velocity, v_c , the heat-production rate of the upper crust, A , the dip of the

subduction zone, Θ , the thickness of the accreted slab, d_s , the duration of the accretion cycle, t_a , and the erosion rate, e . Using regional-scale geophysical information from the Himalayan orogen to constrain these input parameters, our model produces a large range of predicted metamorphic conditions, including some that are generally consistent with the observed metamorphism.

However, the *geologic* history of the Himalayan orogen provides more stringent constraints on the values of input parameters, and the resulting synthetic metamorphic patterns are strikingly similar to those observed in the Himalaya. Significant variations from the optimal input parameters (>30%) yields metamorphic results inconsistent with the observations.

Our model is a highly simplified simulation of the geometry and dynamics of real orogens. The most significant simplifications include: 1) there is no internal deformation within slabs; 2) we presume that the intracontinental subduction zones extend from the surface to the base of the lithosphere; and 3) we do not address directly the thermal consequences of extensional features such as the South Tibetan Detachment system. In spite of the above limitations, our analysis suggests that petrologic and geochronologic data may provide a powerful way to constrain the convergence velocity, accretion rate, and regional denudation rate for ancient collisional orogenic belts. Capitalizing on this opportunity requires the development of regionally extensive thermobarometric and geochronologic databases.

References

- Alam, M., 1989. Geology and depositional history of Cenozoic sediments of the Bengal Basin of Bangladesh. *Palaeogeography, Palaeoclimatology, Palaeoecology*, **69**, 125-130.
- Armijo R., Tapponnier, P., Mercier, J. & Han, T.L., 1986. Quaternary extension in southern Tibet; field observations and tectonic implications. *Journal of Geophysical Research*, **B**, **91**, 13,803-13,872.
- Beck, R.A., Burbank, D.W., Sercombe, W.J., Riley, G.W., Barndt, J.K., Berry, J.R., Afzal, J., Khan, A.M., Jurgen, H., Metje, J., Cheema, A., Shafique, N.A., Lawrence, R.D. & Khan, M.A., 1995. Stratigraphic evidence for an early collision between north-west India and Asia. *Nature*, **373**, 55-58.
- Bilham, R., Larson, K., Freymueller, J. & Project Idylhim members, 1997. GPS measurements of present-day convergence across the Nepal Himalaya. *Nature*, **386**, 61-63
- Brunel, M. & Kienast, J.R., 1986. Etude petrostructurale des chevauchements ductile Himalayens sur la bransversale de L'Everest-Makalu Nepal oriental. *Canadian journal of Earth Sciences*, **23**, 1117-1137.
- Burbank, D.W., Leland, J., Fielding, E., Anderson, R.A., Brozovic, N., Reid, M.R., & Duncan, C., 1996. Bedrock incision, rock uplift and threshold hillslopes in the northwestern Himalayas. *Nature*, **379**, 505-510.
- Burchfiel, B.C. & Royden, L.H., 1985. North-south extension within the convergent Himalayan region. *Geology*, **13**, 679-682.
- Burchfiel, B.C., Chen, Z., Hodges, K.V., Liu, Y., Royden, L.H., Deng, C. & Xu, J., 1992. *The South Tibetan Detachment System, Himalayan Orogen: Extension Contemporaneous With and Parallel to Shortening in a Collisional Mountain Belt*. Geological Society of America, Boulder, CO.
- Burg, J.P., Brunel, M., Gapais, D., Chen, G.M., & Liu, G.H., 1984. Deformation of leucogranites of the crystalline Main Central Sheet in southern Tibet China. *Journal of Structural Geology*, **6**, 535-542.
- Caby, R., Pecher, A. and Le Fort, P., 1983. Le MCT. Himalayen: nouvelles donnees sur le metamorphisme inverse a la base de la Dalle du Tibet. *Revue Geogr. phys. Geol. dynam.*, **24**, 89-100.
- Chen, Z. Y. Liu, K.V. Hodges, B.C. Burchfiel, L.H. Royden, and C. Deng, 1990. Structural evolution of the Kangmar dome: A metamorphic core complex in southern Xizang (Tibet): *Science*, **250**, 1552-1556.
- Coleman, M.E., in press. U-Pb constrains on Oligocene-Miocene deformation and anatexis, Marsyandi Valley, central Nepalese Himalaya. *American Journal of Science*.
- Copeland, P, Parrish, R. & Harrison, T.M., 1988. Identification of inherited radiogenic Pb in monazite and its implications for U-Pb systematics. *Nature*, **333**, 760-763.
- Copeland, P., & Harrison, T.M., 1990. Episodic rapid uplift in the Himalaya revealed by ⁴⁰Ar/³⁹Ar analysis of detrital K-feldspar and muscovite, Bengal fan. *Geology*, **18**, 354-357.
- Corrigan, J.D. and K.D. Crowley, 1989. Thermal history of sites 717 and 718, ODP Leg 116, central Indian Ocean; constraints from numerical simulations and apatite

- fission-track data. *Abstracts with Programs - Geological Society of America*. **21**, 320.
- Cuney, M., Le-Fort, P. & Wang, Z., 1984. Uranium and thorium geochemistry and mineralogy in the Manaslu leucogranite (Nepal, Himalaya). In: *Geology of granites and their metallogenic relations; proceeding of the international symposium* eds. Xu, K. & Tu, G., pp. 853-873, Scientific Press, Beijing.
- Dewey, J.F., Cnade, S.C. and Pitman, W.C., 1989. Tectonic evolution of the India/Eurasia collision zone. *Eclogae Geologica Helvetiae*, **82**, 717-734.
- Edwards, M.A., W.S.F. Kidd and T.M. Harrison, 1995, Active medial Miocene detachment in the high Himalaya of the Tibet-Bhutan frontier; a young crystallization age for the Khula Langri leucogranite pluton, *Eos, Transactions* **76**, 567.
- Gansser, A., 1964. *Geology of the Himalayas*. Wiley Interscience, London
- Gansser, A., 1966, The Indian Ocean and the Himalaya: a geologic interpretation, *Eclog. Geol. Helv.*, **59**, 832-848.
- Grujic, D., Casey, M., Davidson, C., Hollister, L.S., Kündig, R., Pavlis, T., and Schmid, S., 1996, Ductile extrusion of the Higher Himalayan crystalline in Bhutan: evidence from quartz microfabrics: *Tectonophysics*, **260**, 21-43
- Guillot, S., Hodges, K.V., Le Fort, P. & Pecher, A., 1994. New constraints on the age of the Manaslu leucogranite: Evidence for episodic tectonic denudation in the central Himalayas. *Geology*, **22**, 559-562.
- Harris, N. and J. Massey, 1994, Decompression and anatexis of Himalayan metapelites. *Tectonics*, **13**, 1537-1546.
- Harrison, T.M., McKegan, K.D. & Le Fort, P., 1995. Detection of inherited monazite in the Manaslu leucogranite by $^{208}\text{Pb}/^{232}\text{Th}$ ion microprobe dating: Crystallization age and tectonic implications. *Earth and Planetary Science Letters*, **133**, 271-282
- Harrison, T.M., Ryerson, F.J., Le Fort, P., Yin, A., Lovera, O.M. & Catlos, E.J., 1997. A Late Miocene-Pliocene origin for the Central Himalayan inverted metamorphism. *Earth and Planetary Science Letters*, **146**, E1-E7.
- Hodges, K.V. & Silverberg, D.S., 1988. Thermal evolution of the Greater Himalaya, Garhwal, India. *Tectonics*, **7**, 583-600.
- Hodges, K., Bowring, S., Davidek, K., Hawkins, D. & Krol, M., in press. Evidence for rapid displacement on Himalayan normal faults and the importance of tectonic denudation in the evolution of mountain ranges. *Nature*.
- Hodges, K.V., Burchfiel, B.C., Royden, L.H., Chen, Z. & Liu, Y., 1993. The metamorphic signature of contemporaneous extension and shortening in the central Himalayan orogen: Data from the Nyalam transect, southern Tibet. *Journal of Metamorphic Geology*, **11**, 721-737.
- Hodges, K.V., Hames, W.E., Olszewski, W.J., Burchfiel, B.C., Royden, L.H., & Chen, Z., 1994. Thermobarometric and $^{40}\text{Ar}/^{39}\text{Ar}$ geochronologic constraints on Eohimalayan metamorphism in the Dinggye area, southern Tibet. *Contributions to Mineralogy and Petrology*, **117**, 151-163.
- Hodges, K.V., Hubbard, M.S. & Silverberg, D.S., 1988. Metamorphic constraints on the thermal evolution of the central Himalayan Orogen. *Philosophical Transactions of the Royal Society of London*, **A 326**, 257-280.

- Hodges, K.V., Parrish, R.S., Housh, T., Lux, D., Burchfiel, B.C., Royden, L., & Chen, Z., 1992. Simultaneous Miocene extension and shortening in the Himalayan orogen. *Science*, **258**, 1466-1470.
- Hodges, K.V., Parrish, R.R. & Searle, M.P., 1996. Tectonic evolution of the central Annapurna Range, Nepalese Himalayas. *Tectonics*, **15**, 1264-1291.
- Hubbard, M.L., 1988. Thermobarometry, $^{40}\text{Ar}/^{39}\text{Ar}$ geochronology, and structure of the Main Central thrust zone and Tibetan Slab, eastern Nepal Himalayas [Ph.D. Thesis]: Massachusetts Institute of Technology, 169 p.
- Hubbard, M., L. Royden and K. Hodges, 1991. Constraints on unroofing rates in the High Himalaya, eastern Nepal, *Tectonics*, **10**, 287-298.
- Hubbard, M.S. and T.M. Harrison, 1989. $^{40}\text{Ar}/^{39}\text{Ar}$ age constraints on deformation and metamorphism in the Main Central thrust zone and Tibetan slab, eastern Nepal Himalaya, *Tectonics*, **8**, 865-880.
- Hubbard, M.S., 1989. Thermobarometric constraints on the thermal history of the Main Central Thrust Zone and Tibetan Slab, eastern Nepal Himalaya, *J. Metamorphic Geol.*, **7**, 19-30.
- Huerta, A.D., L. Royden and K. Hodges, 1996. The Interdependence of Deformational and Thermal Processes in Mountain Belts, *Science*, **273**, 637-639.
- Huerta, A.D., L. Royden and K. Hodges, 1998. The thermal structure of collisional orogens as a response to accretion, erosion, and radiogenic heating. *Journal of Geophysical Research-B*, **103**, 15287-15302.
- Huerta, A.D., L. Royden and K. Hodges, submitted. The effects of accretion, erosion, and radiogenic heat on the metamorphic evolution of collisional orogens. *Journal of Metamorphic Geology*.
- Inger, S. and N.B.W. Harris, 1992, Tectonothermal evolution of the High Himalayan crystalline sequence, Langtang Valley, northern Nepal, *Journal of Metamorphic Geology*, **10**, 439-452.
- Inger, S. and N.B.W. Harris, 1993, Geochemical constraints on leucogranite magmatism in the Langtang Valley, Nepal Himalaya, *Journal of Petrology*, **34**, 345-368.
- Johnson, G.D., N.M. Johnson, N.D. Opdyke and R.A.K. Tahirkheli, 1979, Magnetic reversal stratigraphy and sedimentary tectonic history of the Upper Siwalik Group. In: *Geodynamics of Pakistan* eds Farah, A. and K.A. De Jong, pp. 149-165, Geological Survey of Pakistan, Quelta, Pakistan.
- Klootwijk, C.T. J.S. Gee, J.W. Peirce, G.M. Smith and P.L. McFadden, 1992, An early India-Asia contact; paleomagnetic constraints from Ninetyeast Ridge, ODP Leg 121; with Suppl. Data 92-15. *Geology*, **20**, 395-398.
- Le Fort, P., 1975. Himalayas: The collided range. Present knowledge and of the continental arc. *American Journal of Science*, **275-A**, 1-44.
- Lyon-Caen, H. and P. Molnar, 1985. Gravity anomalies, flexure of the Indian plate, and the structure, support, and evolution of Himalaya and Ganga Basin, *Tectonics*, **4**, 513-538.
- Macfarlane, A.M., 1992. *The Tectonic Evolution of the Core of the Himalaya, Langtang National Park, Central Nepal*, [Ph.D. thesis] Mass. Inst. of Tech, Cambridge, MA.

- Macfarlane, A.M., 1995. An evaluation of the inverted metamorphic gradient at Langtang National Park, central Nepal Himalaya. *Journal of Metamorphic Geology*, **13**, 595-612
- Macfarlane, A., K.V. Hodges and D. Lux, 1992, A structural analysis of the Main Central thrust zone, Langtang National Park, central Nepal Himalaya, *Geological Society of America Bulletin*, **104**, 1389-1402.
- Makovsky, Y. Klemperer, S.L., Huang, L. and Lu, D., 1996. Structural elements of the southern Tethyan Himalaya crust from wide-angle seismic data. *Tectonics*, **15**, 997-1005.
- Metcalf, R.P., 1993, Pressure, temperature and time constraints on metamorphism across the Main Central Thrust zone and High Himalayan Slab in the Garhwal Himalaya. In: *Himalayan Tectonics* eds Treloar, P.J. & M.P. Searle, pp. 485-509, Geological Society Special Publication, 47, London.
- Najman, Y. P. Clift, M.R.W. Johnson and A.H.F. Robertson, 1993, Early stages of foreland basin evolution in the Lesser Himalaya, N. India. In: *Himalayan Tectonics* eds Treloar, P.J. & M.P. Searle, pp. 541-558, Geological Society Special Publication, 47, London.
- Parrish, R.R. and K.V. Hodges, 1993, Miocene (22 ± 1 Ma) metamorphism and to-stage thrusting in the Greater Himalayan sequence, Annapurna Sanctuary, Nepal, *Geological Society of America Abstracts with Programs*, **25**, A174.
- Parrish, R.R. and K.V. Hodges, 1996, Isotopic constraints on the age and provenance of the Lesser and Greater Himalayan sequences, Nepalese Himalaya, *Geological Society of America Bulletin*, **108**, 904-911.
- Parrish, R.R., K.V. Hodges and A. Macfarlane, 1992, U-Pb geochronology of igneous and metamorphic rocks near the Main Central Thrust in the Langtang area, central Nepal Himalaya, in M.P. Searle and P.J. Treloar eds., *7th Himalaya-Tibet-Karakoram Workshop Abstracts*: Oxford, U.K., 67-68.
- Patriat, P. and J. Achache, 1984, India-Eurasia collision chronology and its implications for crustal shortening and driving mechanisms of plates, *Nature*, **311**, 615-621.
- Pecher, A., 1977. Geology of the Nepal Himalaya; deformation and petrography in the Main Central thrust zone. In *Himalaya; sciences de la terre*, ed. Jest, C., pp. 301-318. Centre National de la Recherche Scientifique, Paris.
- Pecher, A., 1978, Deformation et metamorphisme associes a une zone de cisaillement: Exemple du grand chevauchement central Himalyan (MCT) [D. Sc. Thesis]: Grenoble.
- Pecher, A., 1989. The metamorphism in the central Himalaya, *J. Metamorphic Geol.*, **7**, 31-41.
- Pognante, U. and P. Benna, 1993, Metamorphic zonation, migmatization and leucogranites along the Everest transect of eastern Nepal and Tibet: The record of an exhumation history. In: *Himalayan Tectonics*, eds, Treloar, P.J. & M.P. Searle, pp. 323-340, The Geological Society, London.
- Rao, R.U.M., B.V. Rao and H. Narain, Radioactive heat generation and heat flow in the Indian Shield, *Earth and Planetary Science Letters*, **30**, 57-64, 1976.
- Rowley, D.B., 1996. Age of initiation of collision between India and Asia: A review of stratigraphic data: *Earth and Planetary Science Letters*, **145**, 1-13.

- Scaillet, B.C., P. France-Lanord and P. Le Fort, 1990. Badrinath-Gangotri plutons (Garhwal, India): petrological and geochemical evidence for fractionation processes in a high Himalayan leucogranite. *J. of Volc. and Geothermal Res.* **44**, 163-188.
- Scharer, U., 1984. The effect of initial ^{230}Th disequilibrium on young U-Pb ages: the Makalu case, Himalaya, *Earth and Planetary Science Letters*, **67**, 191-204.
- Scharer, U., R. Xu and C. Allegre, 1986. U-(Th)-Pb systematics and ages of Himalayan leucogranites, South Tibet, *Earth and Planetary Science Letters*, **77**, 35-48.
- Schelling, D. and K. Arita, 1991, Thrust tectonics, crustal shortening, and the structure of the far-eastern Nepal Himalaya, *Tectonics*, **10**, 851-862.
- Searle, M.P., 1986. Structural evolution and sequence of thrusting in the High Himalayan, Tibetan-Tethys and Indus suture zones of Zaskar and Ladakh, western Himalaya. *Journal of Structural Geology*, **8**, 923-936.
- Searle, M.P., D.J.W. Cooper, and A.J. Rex, 1988. Collision tectonics of the Ladakh-Zaskar Himalaya, in *Tectonic Evolution of the Himalayas and Tibet*, edited by R.M. Shackleton, J.F. Dewey and B.F. Windley, London, The Royal Society, 117-149.
- Swapp, S.M. and L.S. Hollister, 1991, Inverted metamorphism within the Tibetan Slab of Bhutan: Evidence for a tectonically transported heat-source, *Canadian Mineralogist*, **29**, 1019-1041.
- Vannay, J.-C. and K.V. Hodges, 1996, Tectonometamorphic evolution of the Himalayan metamorphic core between Annapurna and Dhaulagiri, central Nepal. *Journal of Metamorphic Geology*, **14**, 635-656
- Vidal, P., A. Cocherie and P. Le Fort, 1982. Geochemical investigations of the origin of the Manaslu leucogranite (Himalaya, Nepal), *Geochimica Cosmochimica Acta*, **46**, 2279-2292.

Figure Captions

Figure 1; Model geometry used to simulate the thermal evolution of collisional orogens. Initially, the upper and down-going plates have an upper layer of crust enriched in heat-producing elements of thickness d_r . Subduction of the down-going plate and surface erosion of the upper plate act continuously at rates v_c and e respectively. Slabs of the lower plate with vertical thickness d_r are accreted to the upper plate with a periodicity of t_a . The accretion of crust enriched in heat-producing elements from the down-going plate to the upper plate, and subsequent erosion of material from the surface of the upper plate results in the development of a wedge of heat-producing crust within the upper plate.

Figure 2; Surface width and maximum depth of the heat-producing wedge as a function of time. The depth of the wedge reaches its maximum following each accretion event, following each accretion event the depth of the wedge diminishes as erosion removes material from the surface. During the first few accretion cycles, the surface width of the wedge increases at each accretion event. Following time t_w the width and depth of the wedge oscillate between maximum values achieved at the time of accretion, and minimum values reached just prior to accretion.

Figure 3; Left column- Generalized cross sections showing the growth of the wedge of heat producing material within the upper plate of a collisional zone and the thermal evolution from $t=0$ (initiation of collision) to thermal steady state. Contours are isotherms with contour intervals of 100°C , stippled pattern is material accreted to upper plate, white line outlines area of heat-producing crust, solid line shows position of active subduction zone, dashed lines show locations of relict subduction zones marking contacts between accreted slabs.

Right column. Generalized evolution of metamorphic field gradient zone showing metamorphic temperatures (T_m), depths (z_m) and ages (t_m) of a collisional zone. Vertical lines indicate surface location of relict subduction zones marking contacts between accreted slabs.

Figure 4; Steady state temperatures and metamorphic field gradients as a function of heat production rate (A), convergence velocity (v_c), thickness of the accreted slab (d_r), accretion period (t_a), erosion rate (e), and dip of the subduction contact (Θ).

Left Column: Heavy line shows position of subduction contact. Medium line shows outline of wedge of heat-producing crust in upper plate.

Right Column: Heavy line shows zone showing metamorphic temperatures (T_m) and depths (z_m) for case where $A=2\mu\text{W}/\text{m}^3$, $v_c=20\text{ km}/\text{my}$, $d_r=20\text{ km}$, $t_a=10\text{ m.y.}$, $e=1\text{ km}/\text{my}$, $\Theta=15^\circ$. Thin lines show metamorphic temperatures and pressures when each of these parameters are varied

Figure 5; Generalized map of Himalayan orogen showing major tectonostratigraphic zones and faults. Locations refer to studies referenced in text.

- Figure 6; Temperatures and pressures within the Greater Himalayan zone during a) Eohimalayan metamorphism b) Neohimalayan metamorphism.
- Figure 7; Metamorphic temperatures vs. structural position above the Main Central thrust displaying steep-to-inverted metamorphic gradient (left column), metamorphic pressure vs. structural position above the Main Central thrust displaying near-lithostatic metamorphic pressure gradients (right column).
- Figure 8; Range of predicted thermal structures (upper panels) and metamorphic conditions zone showing metamorphic temperatures (T_m), depths (z_m) and ages (t_m) lower panel) of collisional orogen based on input parameters constrained by Himalayan geology.
- Figure 9; Maximum upper plate temperatures as a function of heat production rate (A) and thickness of the heat producing wedge (d_w).
- Figure 10; Results for best-fit simulation of Himalayan metamorphism based on $v_c=20$ km/my, $A=3 \mu\text{W/m}^3$, $\Theta=15^\circ$, $t_a=12.5$ my, $d_r=20$ km, and $e=1.4$ km/my. Upper panels: P-T-t paths for rocks located directly below the MCT-equivalent ($x=142$ km), within the Greater Himalayan equivalent ($x=150, 172$ and 216 km), and directly above the Greater Himalayan equivalent ($x=225$ km). Middle panel; metamorphic field gradient across the orogen zone showing metamorphic temperatures (T_m), depths (z_m) and ages (t_m). Lower panel; general structure of the orogen
- Figure 11; Left; Metamorphic field gradient within the Greater Himalayan equivalent along transect at 30° angle to subduction zone showing metamorphic temperatures (T_m), depths (z_m) and ages (t_m). Right; Metamorphic pressure vs. structural position above the MCT-equivalent displaying near-lithostatic metamorphic pressure gradients (lithostatic gradient based on pressure gradient of 27 MPa/km)

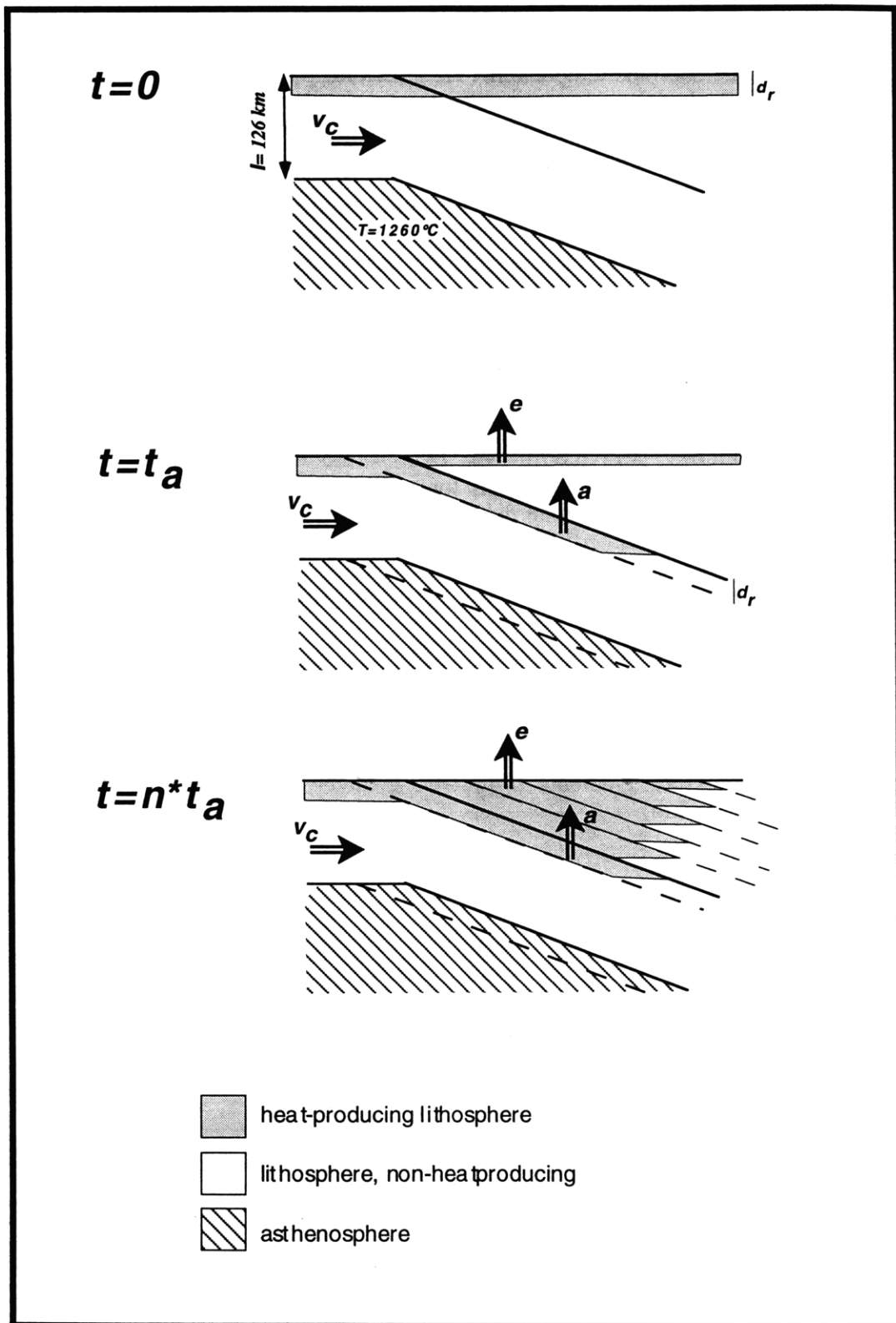


figure 1

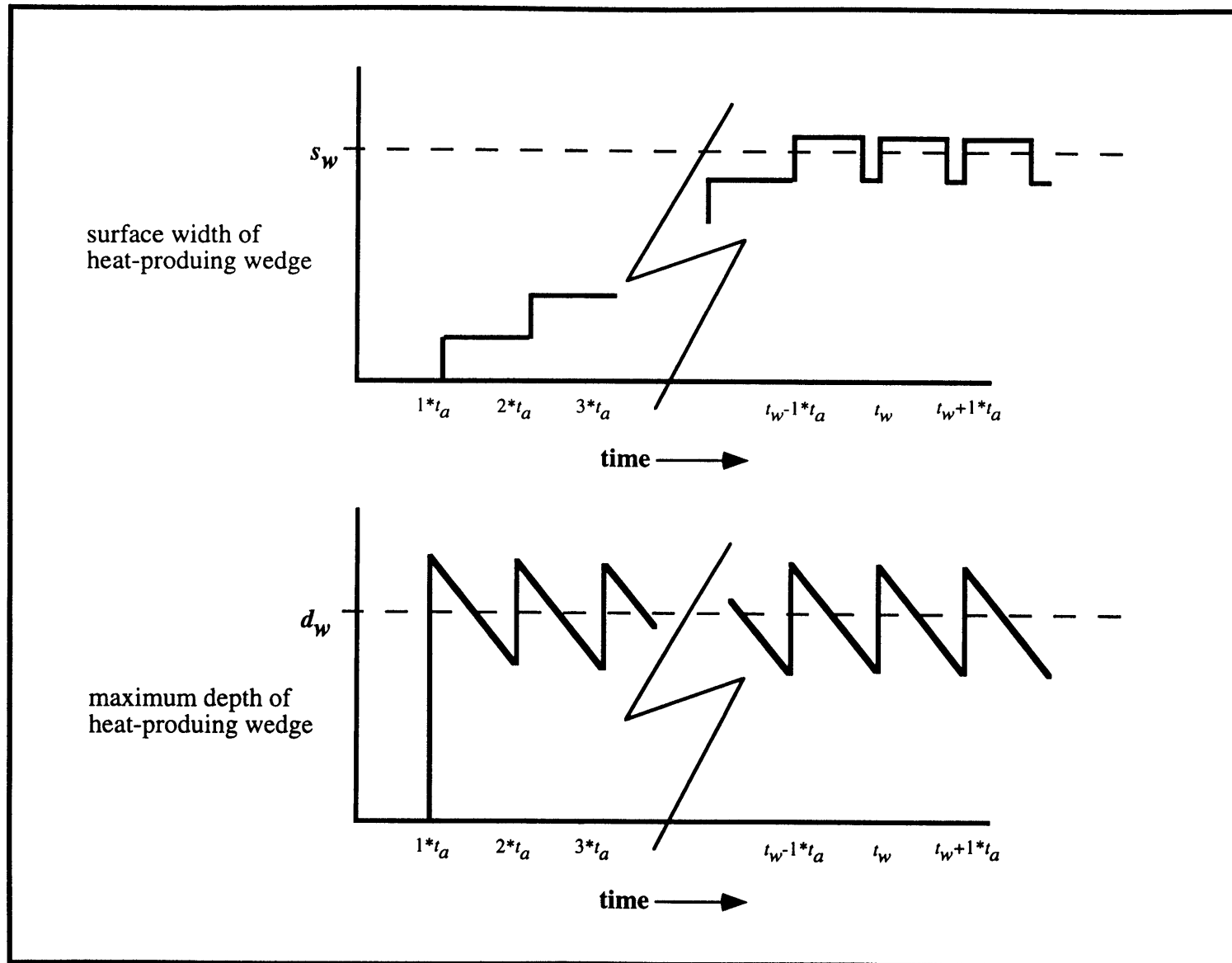


Figure 2

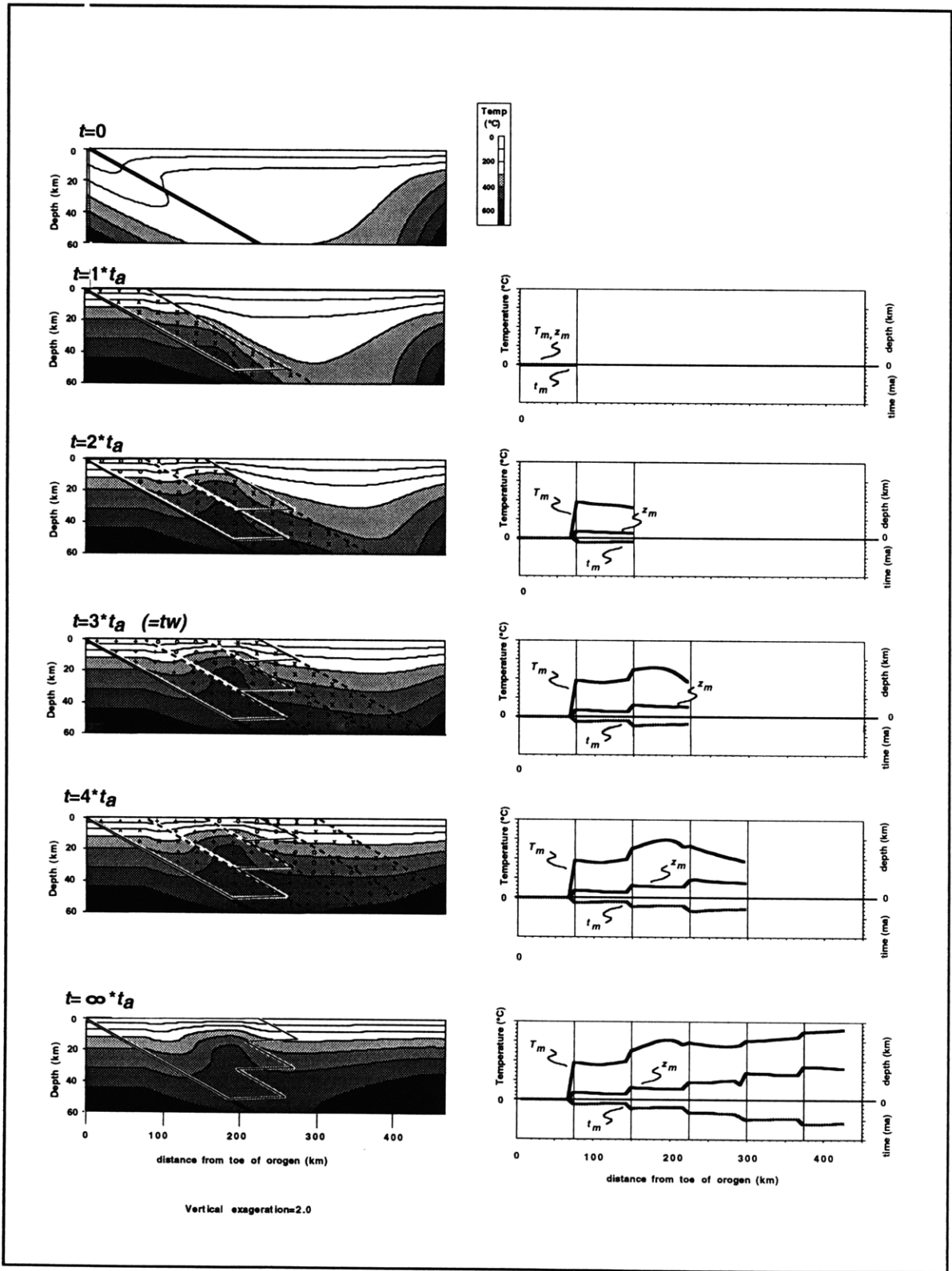


Figure 3

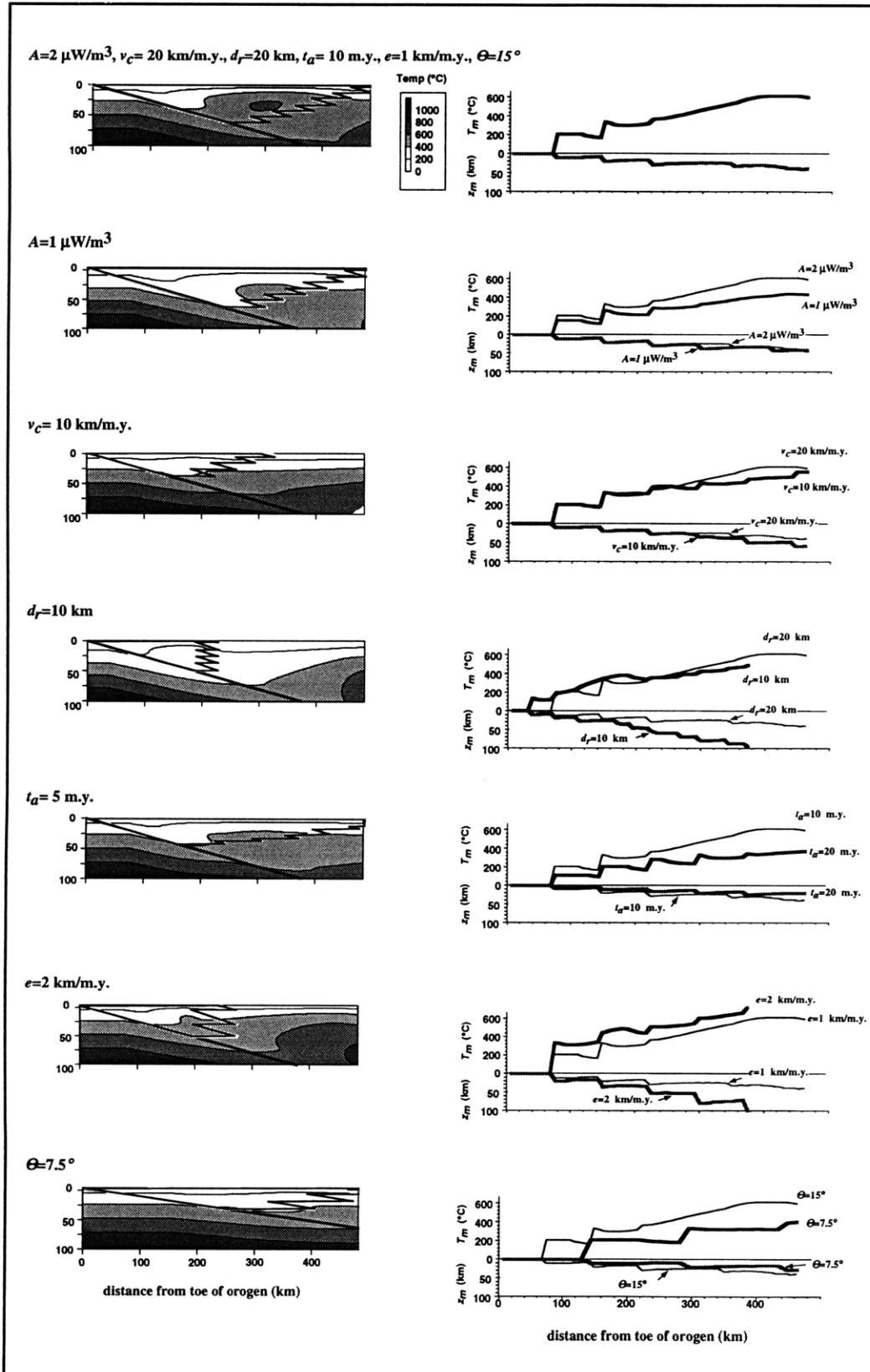
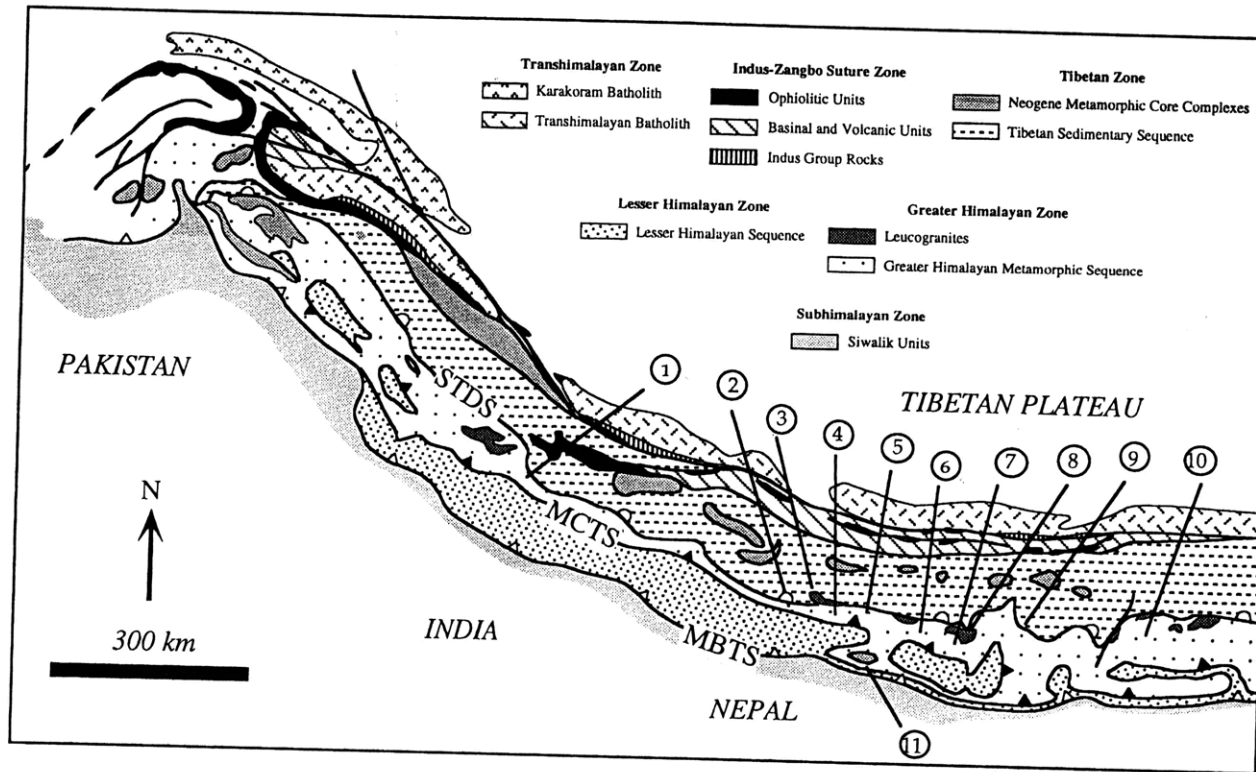


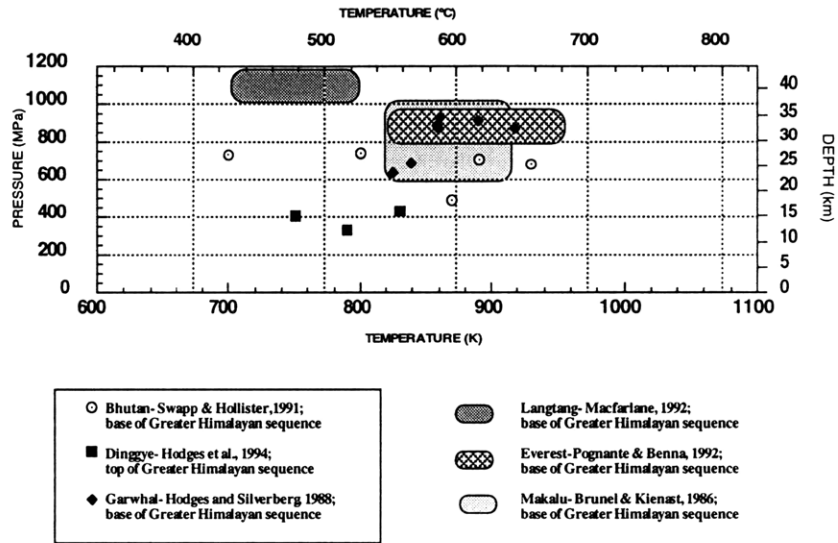
Figure 4



- (1) Garhwal (Hodges & Silverberg, 1988)
- (2) Modi Khola (Parish & Hodges, 1993)
- (3) Manaslu Pluton (Guillot et al., 1994; Harrison & McKeegan, 1994)
- (4) Burhi Gandaki-Darondi (Hodges et al., 1988)
- (5) Langtang (Macfarlane, 1992; Inger & Harris, 1992)
- (6) Nyalam (Hodges et al., 1993)
- (7) Everest (Hubbard, 1988; Pognante & Benna, 1993; Hodges et al., 1992, Hubbard & Harrison, 1989 Burchfiel et al., 1992)
- (8) Makalu (Brunel & Kienast, 1986)
- (9) Dinggyê (Hodges et al., 1994)
- (10) Bhutan (Swapp & Hollister, 1991)
- (11) Kathmandu klippe (Brunel & Kienast, 1986)

Figure 5

a)
Pressures and temperatures of Eohimalayan metamorphism



b)
Pressures and temperatures of Neohimalayan metamorphism

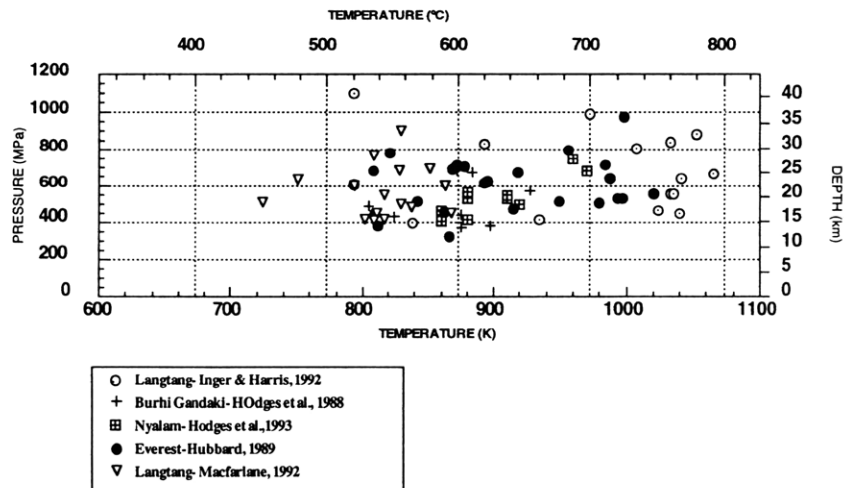


Figure 6

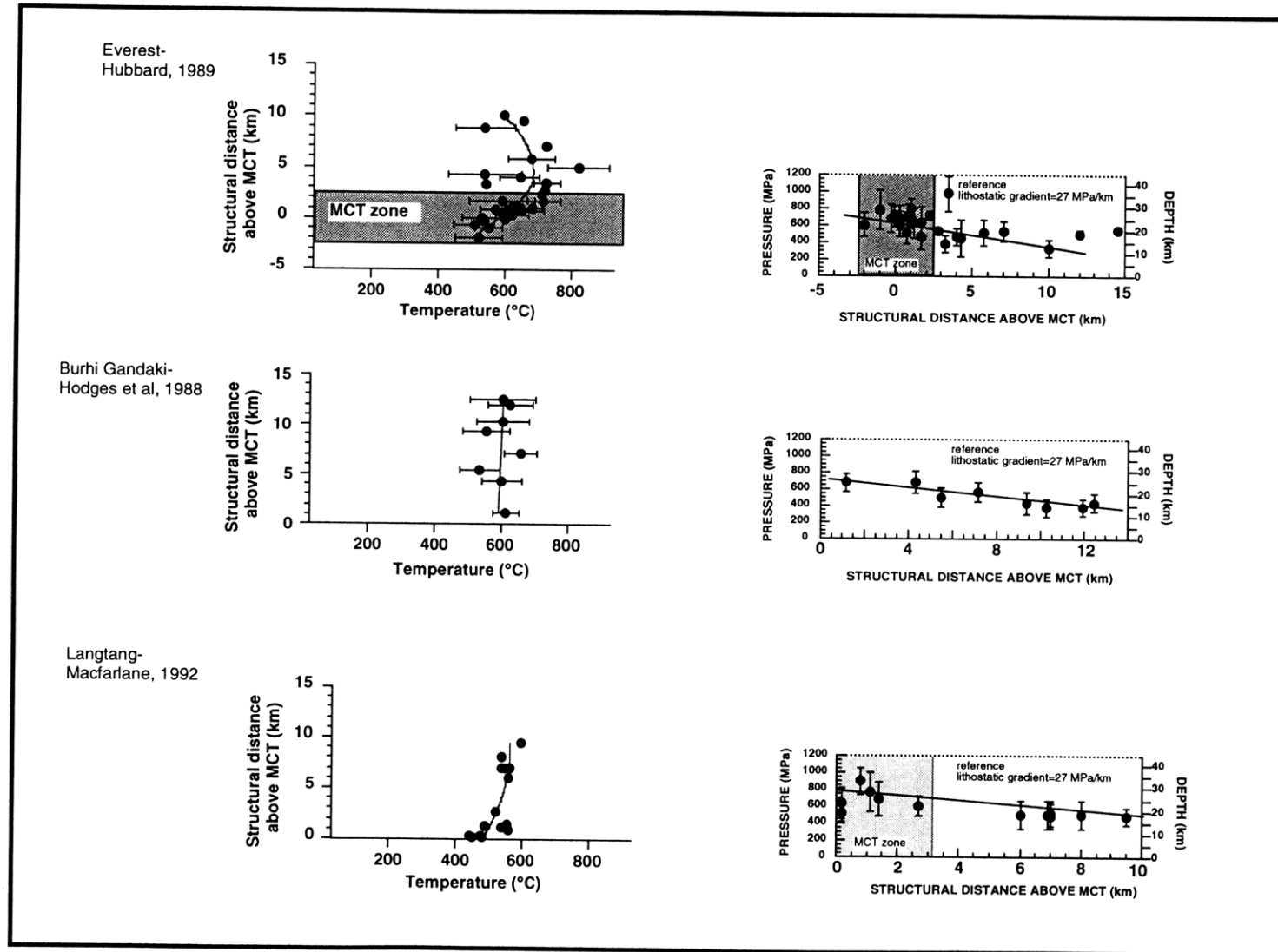


Fig. 7

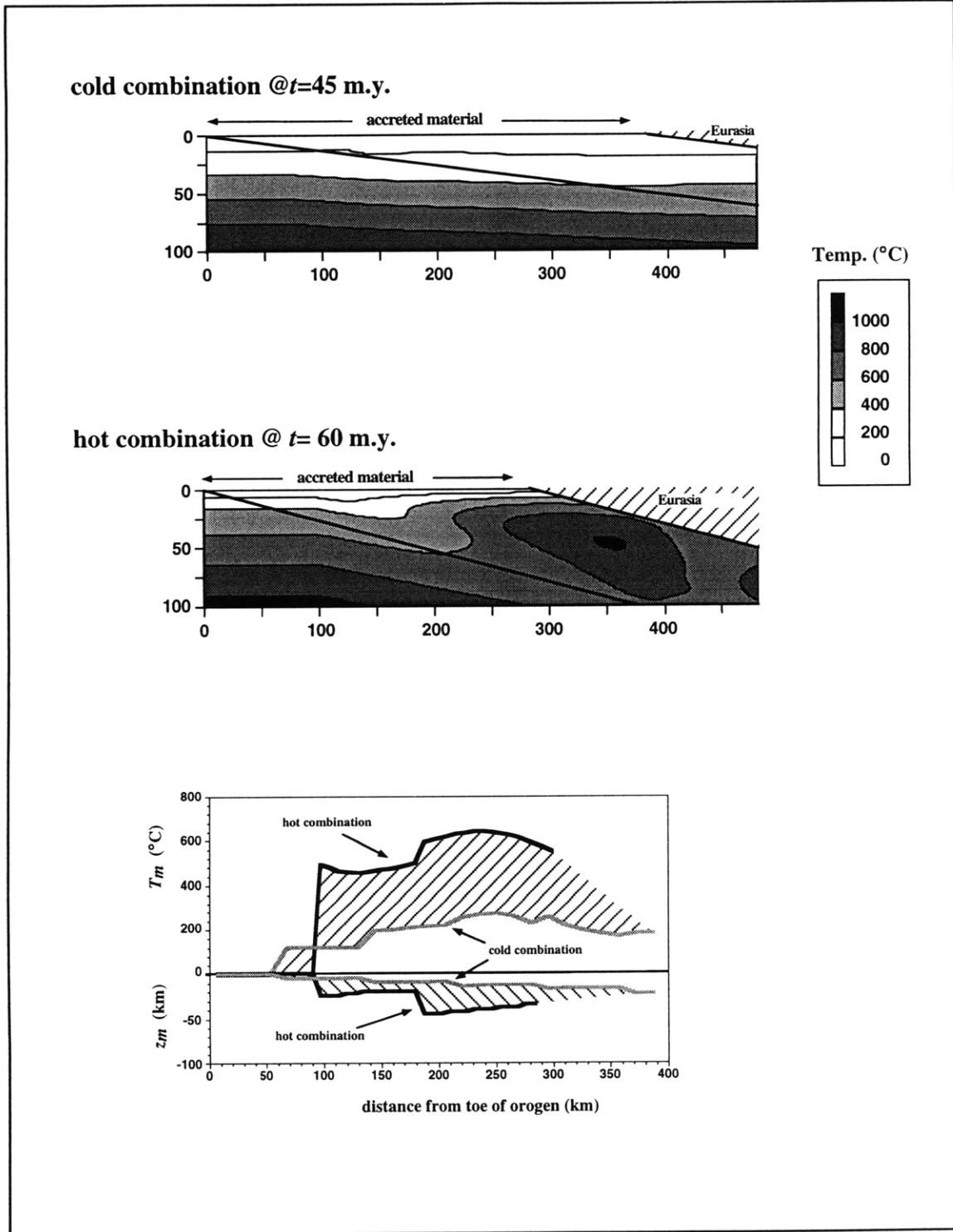


Figure 8

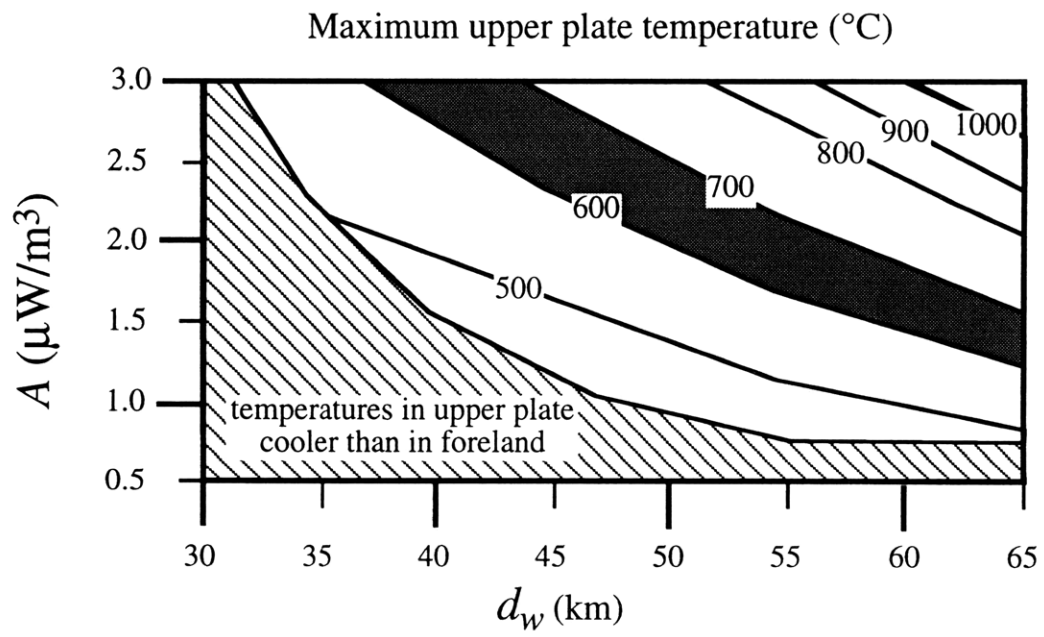


Figure 9

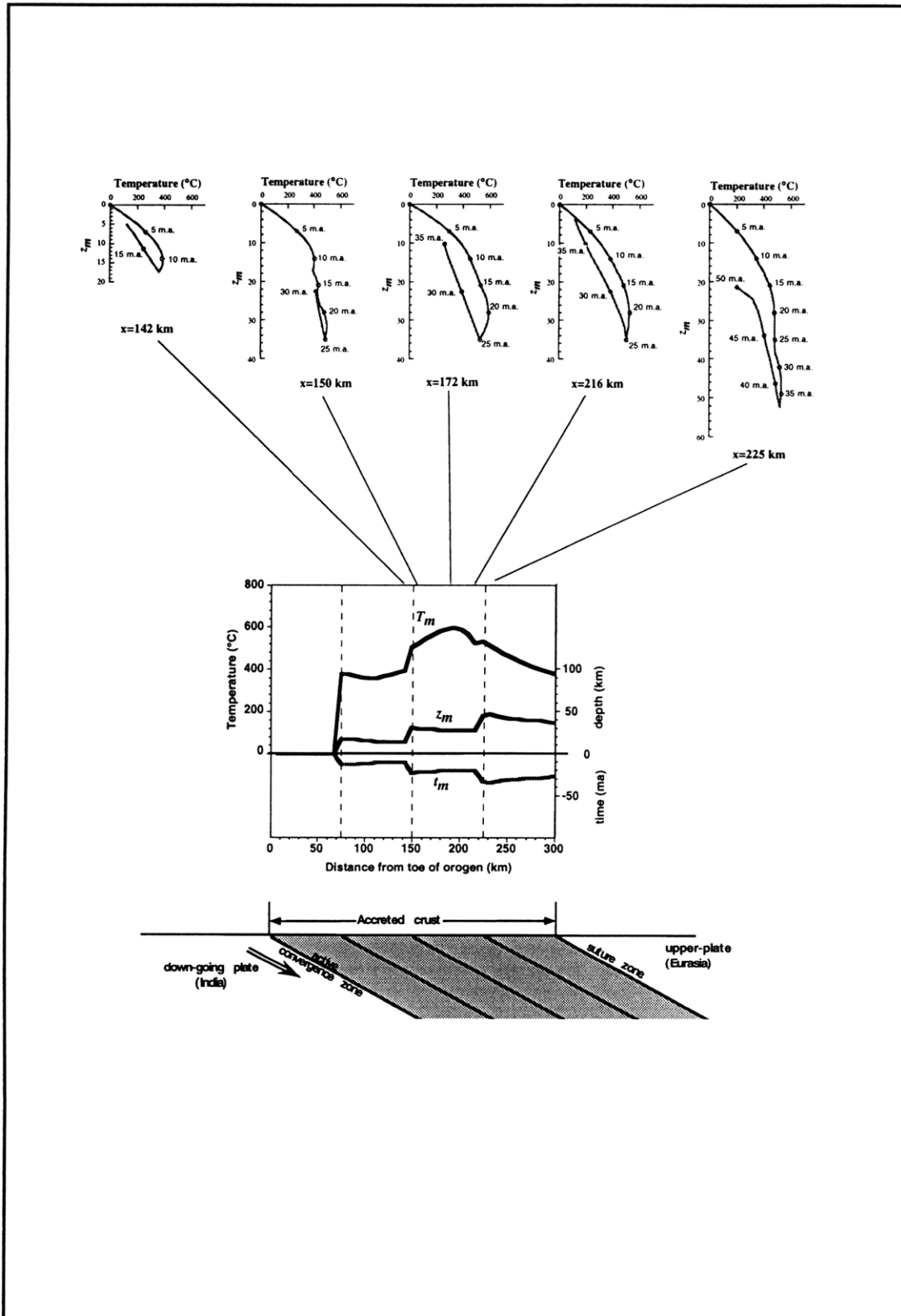


Figure 10

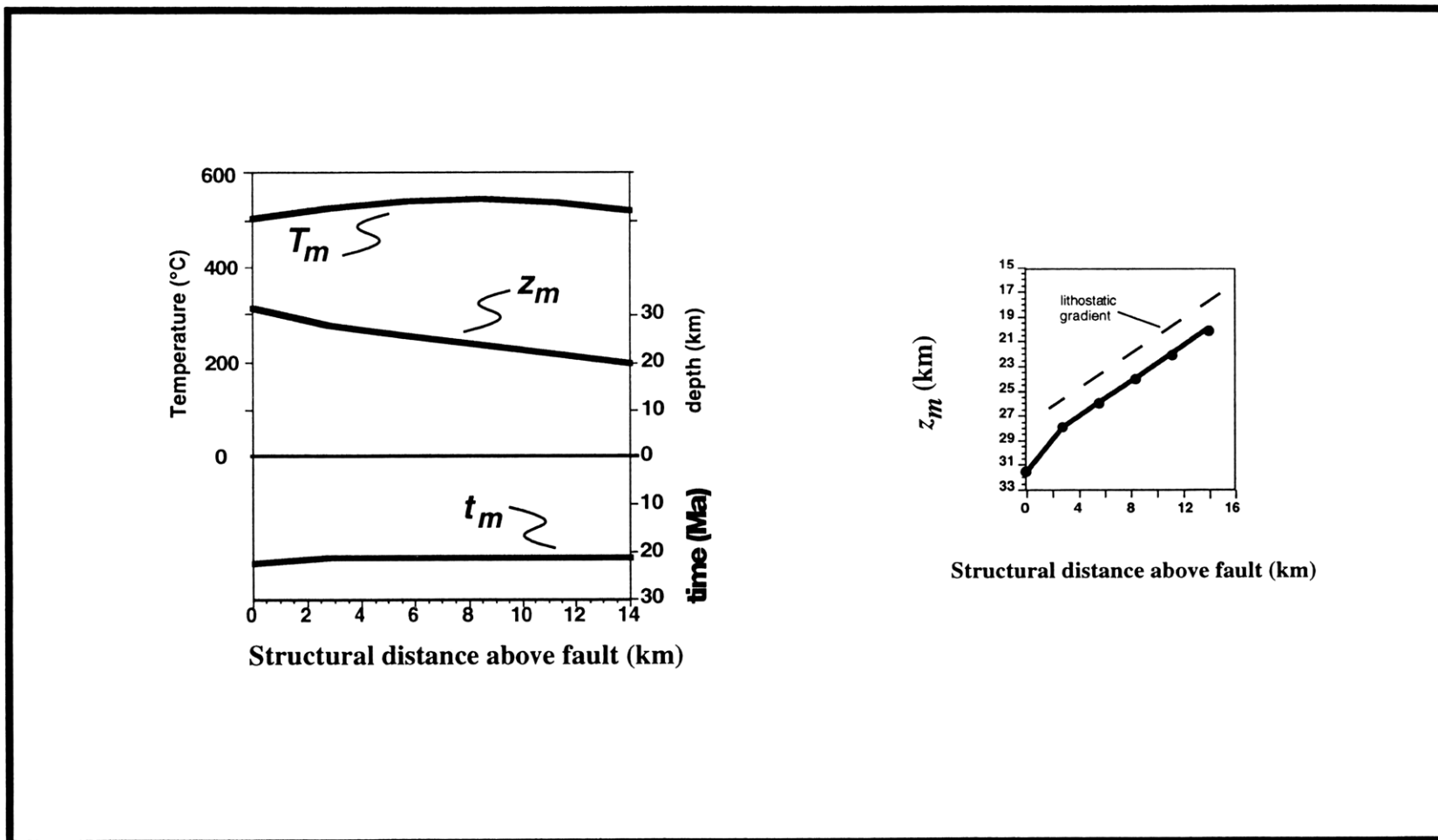


Figure 11

TABLE 1. Definitions of Variables and Values Used

Variable	Physical Meaning	Value or	Comments
A	radioactive heat production rate of upper crust	($\mu\text{W/m}$)	
Θ	dip of subduction zone	($^\circ$)	
d_r	vertical thickness of accreted slab	(km)	
t_a	period of accretion cycle	(my)	
e	erosion rate	(km/my)	
v_c	convergence velocity	(km/my)	velocity of rocks in the down-going plate relative to rocks in the upper plate
ℓ	thickness of foreland lithosphere	126 km	
T_a	temperature at base of lithosphere	1260 $^\circ$ C	
K	thermal conductivity	2.5 W/mK	
α	thermal diffusivity	10^{-6} m ² /s	
τ	time step for thermal model	0.05 my	
Δz	vertical grid spacing	2 km	
Δx	horizontal grid spacing	(km)	$\Delta z/\tan\Theta$
t_w	time to oscillatory stage of heat-producing wedge	(my)	
s_{max}	maximum surface width of heat-producing wedge	(km)	
s_{min}	minimum surface width of heat-producing wedge during oscillatory stage	(km)	
s_w	average maximum surface width of heat-producing wedge during oscillatory stage	(km)	
d_{max}	maximum depth of heat-producing wedge	(km)	
d_{min}	minimum depth of heat-producing wedge during oscillatory stage	(km)	
d_w	average maximum depth of heat-producing wedge	(km)	
x	horizontal distance from upper-plate toe	(km)	
z	vertical distance from surface	(km)	
$T(x,z)$	temperature at location (x,z) within the orogen	($^\circ\text{C}$)	
t	time since initiation of collision	(my)	
T_m	peak metamorphic temperature of rock at surface	($^\circ\text{C}$)	
z_m	depth at T_m	(km)	
t_m	time at T_m	(Ma)	elapsed time between when T_m is reached and surfacing
z_{struct}	structural distance within a column of rock	(km)	measured perpendicular to the subduction boundary

Table 2 Metamorphic record of alternative combinations of input parameters^

	Input						Output									
	d_r (km)	t_o (my)	Θ (°)	v_c (km/my)	e (km/my)	A $\mu\text{W/m}^3$	Geometry of heat-producing wedge		Conditions at Metamorphic core			Orogen Geometry				
							d_w (km)	s_w (km)	location of metamorphic core with respect to toe of orogen	T_m (°C)	z_m^* (km)	t_m^* (Ma)	t (m.y.)	width of orogen (km)	width of slab (km)	number of subduction zones [#]
Optimal Combination	20	12.5	15	15	1.4	3.0	42	218	$x=172$ km, middle of 3 rd slab	600	28	20	50	300	75	4
Non-optimal Combinations	15	10	15	20	1.5	4.0	44	193	$x=172$ km bottom of 4 th slab	605	24	16	50	280	56	5
	25	12.5	15	20	2.0	2.4	52	224	$x=224$ km middle of 3 rd slab	690	38	19	50	375	93	4
	20	19	15	10	0.75	3.0	42	211	$x=202$ km middle of 3 rd slab	494	24	32	57	300	75	4
	20	9.5	15	20	1.5	3.0	42	211	$x=261$ km middle of 4 th slab	620	34	23	50	300	75	5
	20	12.5	10	20	1.3	3.0	47	329	$x=295$ km top of 3 rd slab	578	26	20	50	452	113	4
	23	10	20	17	2.3	2.6	47	160	$x=148$ km middle of 3 rd slab	629	37	16	50	219	55	5

^Parameter combinations selected to approximate structural and metamorphic record of Himalayas: $T_m \geq 600^\circ\text{C}$, $z_m \sim 25\text{-}30$ km, $t_m \sim 20\text{Ma}$, and metamorphic core located within 3rd slab above toe of orogen

*Conditions at base of slab containing metamorphic core

#not including suture zone